Leibniz Institute for

Astrophysics Potsdam

Clarifying the discrepant results in the characterization of exoplanetary atmospheres

Xanthippi Alexoudi

Cumulative Dissertation to obtain the academic degree

”doctor rerum naturalium”
(Dr. rer. nat.)
in the scientific discipline of

Astrophysics

submitted to the
Faculty of Mathematics and Natural Sciences
of the University of Potsdam

Potsdam, 22 March 2023
Disputation: Potsdam, 30 June 2023

Supervisors:	Reviewers:
Principal supervisor: Prof. Dr. Klaus G. Strassmeier	Prof. Dr. Klaus G. Strassmeier
Second supervisor: Prof. Dr. Philipp Richter	Prof. Dr. Stephan Geier
Mentor: Dr. Matthias Mallonn	Prof. Dr. Arnold Hanslmeier

Abstract

Planets outside our solar system, so-called "exoplanets", can be detected with different methods, and currently more than 5000 exoplanets have been confirmed, according to NASA Exoplanet Archive. One major highlight of the studies on exoplanets in the past twenty years is the characterization of their atmospheres using transmission spectroscopy as the exoplanet transits. However, this characterization is a challenging process and sometimes there are reported discrepancies in the literature regarding the atmosphere of the same exoplanet. One potential reason for the observed atmospheric inconsistencies is called impact parameter degeneracy, and it is highly driven by the limb darkening effect of the host star. A brief introduction to those topics in presented in chapter 1, while the motivation and objectives of this work are described in chapter 2.

The first goal is to clarify the origin of the transmission spectrum, which is an indicator of an exoplanet's atmosphere; whether it is real or influenced by the impact parameter degeneracy. A second goal is to determine whether photometry from space using the Transiting Exoplanet Survey Satellite (TESS), could improve on the major parameters, which are responsible for the aforementioned degeneracy, of known exoplanetary systems. Three individual projects were conducted in order to address those goals. The three manuscripts are presented, in short, in the manuscript overview in chapter 3.

More specifically, in chapter 4, the first manuscript is presented, which is an extended investigation on the impact parameter degeneracy and its application on synthetic transmission spectra. Evidently, the limb darkening of the host star is an important driver for this effect. It keeps the degeneracy persisting through different groups of exoplanets, based on the uncertainty of their impact parameter and on the type of their host star. The second goal, was addressed in the second and third manuscripts (chapter 5 and chapter 6 respectively). Using observations from the TESS mission, two samples of exoplanets were studied; 10 transiting inflated hot-Jupiters and 43 transiting grazing systems. Potentially, the refinement or confirmation of their major system parameters' measurements can assist in solving current or future discrepancies regarding their atmospheric characterization.

In chapter 7 the conclusions of this work are discussed, while in chapter 8 it is proposed how TESS's measurements can be able to discern between erroneous interpretations of transmission spectra, especially on systems where the impact parameter degeneracy is likely not applicable.

Zusammenfassung

Planeten außerhalb unseres Sonnensystems, sogenannte Ëxoplaneten", lassen sich mit verschiedenen Methoden aufspüren, und nach Angaben des NASA Exoplanet Archive wurden bisher mehr als 5000 Exoplaneten bestätigt. Ein großer Höhepunkt der Studien über Exoplaneten in den letzten zwanzig Jahren ist die Charakterisierung ihrer Atmosphäre mit Hilfe der Methode der Transmissionsspektroskopie. Diese Charakterisierung ist jedoch ein schwieriger Prozess, und manchmal wird in der Literatur für den gleichen Planeten unterschiedliche Resultate bezüglich seiner Systemparameter gezeigt. Ein möglicher Grund für die beobachteten atmosphärischen Unstimmigkeiten könnte durch die Entartung des Impaktparameters herrühren, die in hohem Maße durch den Verdunkelungseffekt des Muttersterns beeinflusst wird. Eine kurze Einführung in diese Themen wird in Kapitel 1 gegeben, während die Motivation und die Ziele dieser Arbeit in Kapitel 2 beschrieben werden.

Das erste Ziel dieser Arbeit ist die Klärung der Herkunft von Merkmalen im Transmissionsspektrum, die Indikatoren für die Atmosphäre eines Exoplaneten sind; ob sie real sind oder durch die Entartung des Impaktparameters beeinflusst werden. Ein zweites Ziel ist es, festzustellen, ob die Photometrie aus dem Weltraum mit Hilfe des Transiting Exoplanet Survey Satellite (TESS) die atmosphärischen Systemparameter bekannter Exoplanetensysteme verbessern könnte. Drei Einzelprojekte wurden durchgeführt, um diese Ziele zu erreichen. Die drei Manuskripte werden in der Manuskriptübersicht in Kapitel 3 kurz vorgestellt.

Genauer gesagt, wird in Kapitel 4 das erste Manuskript vorgestellt, welches eine erweiterte Untersuchung der Entartung des Impaktparameters und seine Anwendung auf synthetische Transmissionsspektren darstellt. Offensichtlich ist die Randverdunkelung des Muttersterns ein wichtiger Treiber für diesen Effekt. Sie sorgt dafür, dass die Entartung über verschiedene Gruppen von Exoplaneten, die auf der Unsicherheit ihrer Impaktparameters und dem Typ ihres Muttersterns beruhen, auftaucht. Das zweite Ziel wurde im zweiten und dritten Manuskript behandelt (Kapitel 5 und Kapitel 6, jeweils). Anhand von Beobachtungen der TESS-Mission wurden zwei Populationen von Exoplaneten untersucht: zehn transitierende, aufgeblähte heiße-Jupiter Planeten und 43 nicht-zentral transitierende. Möglicherweise kann die Verbesserung oder Bestätigung der Messungen der wichtigsten Systemparameter dazu beitragen, aktuelle oder zukünftige Diskrepanzen bei der Charakterisierung ihrer Atmosphäre zu lösen.

In Kapitel 7 werden die Schlussfolgerungen dieser Arbeit erörtert, während in Kapitel 8 diskutiert wird, wie die Messungen von TESS in der Lage sein können, zwischen fehlerhaften Interpretationen von Transmissionsspektren zu unterscheiden, insbesondere bei Systemen, bei denen die Entartung des Impaktparameters wahrscheinlich nicht zutrifft.

Contents

List of Figures

List of Tables

1 Introduction

1.1 A brief historical overview of exoplanet discoveries

The idea of the existence of other worlds, other than the Earth, captivated the curious minds since the ancient times. Early evidence of this is a letter from the ancient Greek philosopher Epicurus to Herodotus [1] where he expressed his belief that:

> *Αλλὰ μὴν καὶ κόσμοι ἄπειροί εἰσιν, οἵ θ᾽ ὅμοιοι τούτῳ καὶ ἀνόμοιοι*
> ‘The worlds also are infinite, whether they resemble this one of ours or whether they are different from it’.

The widely known term of "Exoplanet", as used today in science, is of Greek origin; a combination of the words ‘exo’ (ἔξω) which means external and ‘planet’(πλανήτης), which means "wanderer". The exoplanet is therefore a planet outside our Solar System. This early hypothesis of the existence of exoplanets, implied in that letter from Epicurus, is dated back to ca. 300 BC. However, without means to prove this hypothesis and with Aristotle’s persistence on the existence of a single world, the idea was abandoned for the centuries to come. It was then during the Renaissance, when the Italian philosopher Giordano Bruno introduced his idea of an infinite universe and the multiplicity of worlds. His proposal was quite accurate at that time. The stars were presented as distant suns surrounded by planets, and he suggested that some of them might even support life. This idea was known as cosmic pluralism. Giordano Bruno was accused by the church as a heretic and was sentenced to execution by burning [2]. Another important milestone, on this brief historical overview, comes in the year 1992 where the first detection of an exoplanet around a pulsar was confirmed, by the astronomers Aleksander Wolszczan and Dale Frail (Wolszczan & Frail 1992). However, the discovery of an exoplanet around a Sun-like star was not made until three years later by the astronomers Michel Mayor and Didier Queloz (2019 Nobel Prize in Physics [3]), who discovered an exoplanet in the 51 Pegasi system.

Since the first discovery, different methods were developed for the detection of exoplanets and advances in astronomical instrumentation were made. Currently, a synergy with both ground-based telescopes and space-based missions, has identified more than 5000 exoplanetary systems (as of end of February 2023 [4]). From the ground some of the most widely known missions dedicated to this purpose are the

---

[1] The Letter of Epicurus to Herodotus, Book 10, Sections 45, translation is by C.D. Yonge (1895)

[2] https://www.britannica.com/biography/Giordano-Bruno

[3] https://www.nature.com/articles/d41586-019-02964-z

[4] https://exoplanetarchive.ipac.caltech.edu/

Wide Angle Search for Planets (WASP) survey (Pollacco et al. 2006), the Hungarian-made Automated Telescope Network (HATNet) Exoplanet Survey (Bakos et al. 2004), the XO project (McCullough et al. 2005) and the Next-Generation Transit Survey (NGTS) (Wheatley et al. 2018). Honorable mentions that are no longer operational are the Trans-Atlantic Exoplanet Survey (TrES) (Alonso et al. 2007) and the Kilodegree Extremely Little Telescope (or KELT) survey. From space, some notable missions are the CoRoT mission (Auvergne et al. 2009) and the Kepler mission (Borucki et al. 2010), which later on gave their leading roles to K2 mission (Howell et al. 2014) and to the Transiting Exoplanet Survey Satellite (TESS) (Ricker et al. 2014). Even though the Hubble Space Telescope[5] (HST) was not developed for exoplanetary discoveries and investigation, eventually it contributed significantly to the exploration of these worlds.

The study of exoplanetary systems is considered a relatively young field but rather rapidly growing; especially, since the detection and atmospheric characterization of HD 209458-b(Charbonneau et al. 2000, 2002), an exoplanet orbiting around a Sun-like star (HD 209458), using the transit method.

1.2 The Transit Detection Method

One of the most commonly used methods for exoplanet detection, and eventually atmospheric characterization, is the transit detection method. At the right orbital configuration, on a nearly edge-on orbit around their host star, exoplanets can be detected. This method favors the detection of gas giants exoplanets, similar in size with Jupiter, and orbital period of less than 10 days. These planets, because of their short period, are very close to their host stars (about 1/10th of Mercury's orbit, if we consider an analogy to our own Solar System), and for this reason they are unusually hot, with equilibrium temperatures around 1500 K, hence the term "hot-Jupiters".

The transit method (also known as transit photometry method) searches for a dip in the received stellar brightness, which is a consequence of the fact that the planet transits (passes in front of) the stellar disc, for a certain period of time (Fig.1.2). This transit depth is equal to the ratio of the planet-to-star surfaces, or $(R_p/R_s)^2$, with R_p being the planetary radius and R_s the stellar radius, respectively. This amount is in the order of about 1% for a hot-Jupiter like planet orbiting a solar-like star, while for an Earth-like system this dip is about 0.01%.

The investigation of transiting events can provide not only the exoplanet detection but also precise measurements on different system parameters, i.e., the orbital period (P, with observations of at least 2 transiting events), the planet-to-star radii ratio (R_p/R_s, with prior knowledge of R_s), the impact parameter (b, defined as the projected distance between the centers of the planet and star during mid-transit), and the density of the star ($\rho_\odot$, knowing the ratio a/R_s and Kepler's Third Law) (Seager & Mallén-Ornelas 2003).

The transit parameters can be used with radial velocity (RV) studies in order to determine the mass of the planet. The radial velocity method, or Doppler spectroscopy, observes Doppler shifts in the stellar spectrum, as the star-planet system orbit each other around a common center of mass. Knowing the stellar mass (M_s),

---

[5] https://www.stsci.edu/hst

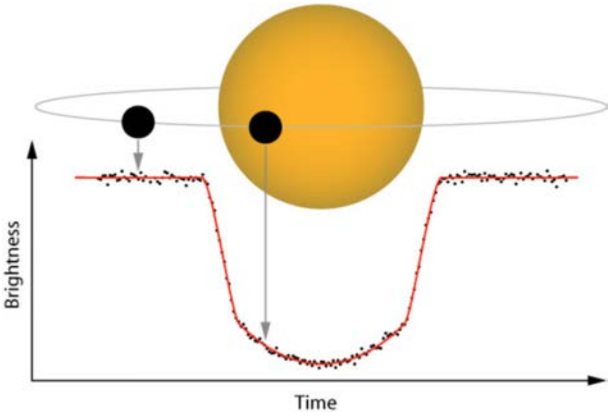

Figure 1.1: Light curve of a transiting exoplanet. On the y-axis of the plot is the received brightness of the star, and on the x-axis the time of the event. When the transiting exoplanet moves in front of the star, it blocks some of the starlight and this leads to a dip in the brightness. The fraction of the light which is blocked depends on the size of the planet. The black dots represent photometric measurements of the event, while the red solid line is a transit model fit to the data. Image credit: NASA

the planetary mass can be inferred, M_p, but this would be only a lower limit estimation for M_p, without the knowledge of the inclination value, i, of the system. This value can be estimated with the transit analysis. Those two methods, transit and RV, are usually complementary to each other in order to determine major system characteristics. This synergy enables an estimate to be made of the planetary density and yields a first characterization of the exoplanet regarding its composition.

1.3 Atmospheric Characterization

Transit events are not only useful in order to provide the fundamental physical and orbital parameters of an exoplanetary system, but also allow us to have a glimpse of an exoplanetary atmosphere. During a transit event, a fraction of the starlight will pass through the upper atmosphere of the planet (if there is an atmosphere) where the atoms, molecules, and aerosols will absorb or scatter some wavelengths of this light. Inevitably, at an observing wavelength of e.g., a strong atomic or molecular absorption feature by the atmosphere, the planet will appear larger (Fig.1.2). By observing how the apparent radius of the planet changes with different wavelengths of observation, a transmission spectrum can be constructed, revealing an estimation of the atmospheric composition (e.g., Deming & Seager 2017). This is the basic principle of a method called “Transmission Spectroscopy”, which was used also for the first characterization of an exoplanetary atmosphere (Charbonneau et al. 2002), and it has been widely used since.

The transmission spectra are able to show, especially for gaseous exoplanets, possible scattering in the atmospheres by small particles (Rayleigh scattering), or by larger particles (Mie scattering). This is pronounced in the spectra with a downward slope at the blue wavelengths of observation. Moreover, absorption features can be identified on transmission spectra, some of which are the alkali features of Na and

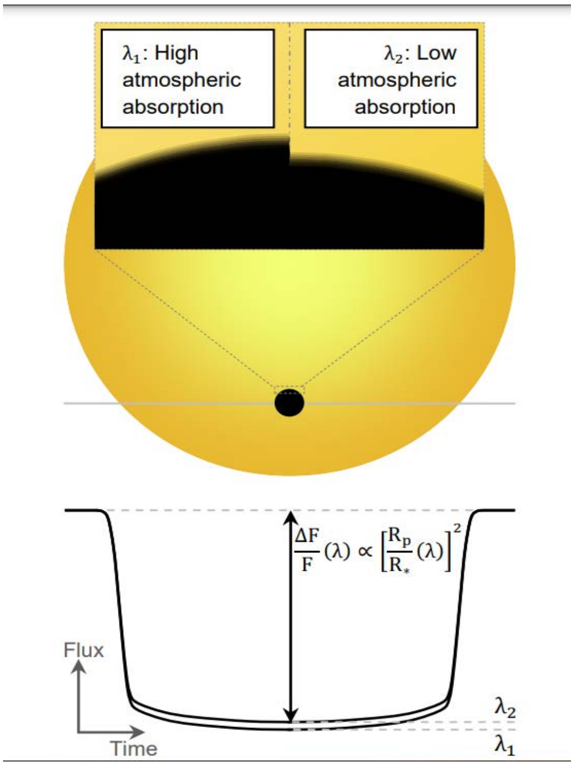

Figure 1.2: This is a representation of the fundamental notion of transmission spectroscopy. During a transiting event there is a drop in the received flux which is wavelength dependent due to the atmosphere of the planet. Evidently, at a wavelength with high atmospheric absorption, the apparent planetary radius will appear larger. Image credit: de Wit & Seager (2013).

K, while molecules of H_2O, CO, CH_4, CO_2 , HCN, TiO/VO are also observed (e.g., Madhusudhan 2012; Moses et al. 2013; Sing et al. 2016; Tsiaras et al. 2019; Guo et al. 2020; Edwards et al. 2021a; Ahrer et al. 2022). On the other hand, sometimes, the received spectra are featureless. This could be indicative of the absence of those atomic features and molecules, while they could also potentially indicate high altitude clouds, that are able to obscure part or completely those spectral features. Photochemical hazes, similarly to condensation clouds, can conceal the atmospheric features as well (e.g., Wakeford & Sing 2015; Gao et al. 2021).

Some highlights of ground-based works regarding the atmospheric characterization of exoplanets are presented in Madhusudhan (2019). In Fig. 1.3, the transmission spectra for WASP-19 b, WASP-127 b and WASP-96 b are shown, exhibiting elements present in their atmospheres. In the y-axis is the R_p/R_s with an offset value with each spectrum for clarity, while x-axis indicates the wavelength of observation. The dots represent the measurements as the planetary radius changes with wavelength, due to atmospheric absorption. The solid lines are atmospheric models fitting the data, while the dashed lines show the wavelengths where specific atmospheric features can be detected. For WASP-19 b, there is an evident detection of TiO, for WASP-127 b detections of Na, K, and Li, and for WASP-96 b, a clear detection of Na. From space, e.g., in the work of Sing et al. (2016), a fascinating diversity of exoplanetary atmospheres has been revealed with transit observations of 10 hot-Jupiters, with the Hubble Space Telescope and Spitzer Space Telescope.

To conclude, transmission spectra can reveal some atmospheric components of an exoplanet (e.g., Wakeford et al. 2017; Tsiaras et al. 2018; Kreidberg et al. 2018; Chachan et al. 2020; Mugnai et al. 2021) from clear atmospheres, e.g., with an evidence of alkali absorption (Seager & Sasselov 2000), to cloudy atmospheres, which are characterized by flat spectra, and hazy atmospheres showing a Rayleigh signature (e.g., Sing et al. 2016).

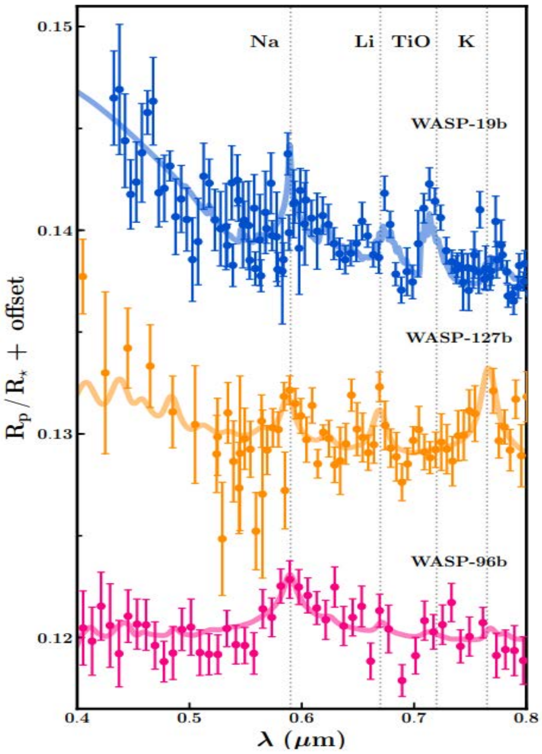

Figure 1.3: Transmission spectra of WASP-19 b, WASP-127 b, and WASP-96 b of high quality, obtained with ground-based telescopes. The solid lines are atmospheric models, while the spectral features are shown in dashed lines at the corresponding wavelengths of observation. The Na doublet peaks approximately at 576.8 nm and K peaks at 778.8 nm. This is Fig.4 from Madhusudhan (2019).

1.4 Atmospheric discrepancies

The shape of the transmission spectra can sometimes be mimicked by other factors, e.g. third light contamination from a nearby star (e.g., Mallonn & Strassmeier 2016), or significant stellar activity, i.e. stellar spots mimic planetary transits (e.g., Oshagh et al. 2014; Mallonn et al. 2018). Therefore, transmission spectra can be sensitive to factors that need to be considered during the transit light curve analysis and interpretation. A characterization of an exoplanet atmosphere is more robust when confirmed from different observations and analysis methods, by different instruments and different groups. In the literature, there are many atmospheric characterizations on exoplanets confirmed by independent investigations, e.g., the clear atmosphere of WASP-39 b (e.g., Fischer et al. 2016; Nikolov et al. 2016) or the flat spectrum of GJ-1214 b (e.g., Nascimbeni et al. 2015; Kreidberg et al. 2014). However, there are also reported discrepancies, with contradicting results for the same exoplanets, investigated by different groups. Some examples are shown in Table 1.1. According to these investigations, the discrepancies refer to the presence or absence of alkali elements, the direction of the spectral slope, presence of Rayleigh slope or rather a flat spectrum, offsets in the measurements or different amplitudes of the Rayleigh feature, and this list is not conclusive. A potential reason for these atmospheric misinterpretations, considering a quiet host star without significant activity and that there is no contamination of the light curves from a third light in the system, can be the Limb Darkening effect of the star itself.

Exoplanet	References	Discrepancy
GJ1214 b	Rackham et al. (2017) vs.Nascimbeni et al. (2015); de Mooij et al. (2013); Narita et al. (2013)	upward slope, flat spectrum or downward slope
HAT-P-1 b	Sing et al. (2016) vs. Wilson et al. (2015)	Presence/Absence of K
HAT-P-32 b	Mallonn & Strassmeier (2016) vs. Gibson et al. (2013a) and Nortmann et al. (2016)	scattering slope vs. flat spectrum
TrEs-3 b	Parviainen et al. (2016) vs. Mackebrandt et al. (2017)	Presence/Absence of a Rayleigh feature
WASP-12 b	Stevenson et al. (2014) vs. Sing et al. (2013)	Offset in measurements
WASP-17 b	Sedaghati et al. (2016) vs. Sing et al. (2016)	Presence/Absence of K
WASP-19 b	Huitson et al. (2013) vs. Sedaghati et al. (2017)	Presence/Absence of TiO
WASP-31 b	Sing et al. (2016) vs. Gibson et al. (2017)	Presence/Absence of K
WASP-52 b	Louden et al. (2017) vs. Chen et al. (2017)	Presence/Absence of Na
WASP-6 b	Jordán et al. (2013) vs. Nikolov et al. (2014)	Different amplitudes of Rayleigh feature
WASP-80 b	Kirk et al. (2018) vs. Sedaghati et al. (2017) vs. Parviainen et al. (2018)	Rayleigh feature vs. Alkali presence vs. flat spectrum

Table 1.1: Some reported discrepancies in the literature, regarding atmospheric characterization of exoplanets.

1.5 The Limb Darkening Effect

The Limb Darkening (LD) is a projection effect of the host stars. It represents the stellar brightness as a function of the stellar radius and makes the star appearing brighter at the center and darker towards the limb. This phenomenon takes place due to the different temperatures through the different layers of the stellar structure; lower temperature produces photons of longer wavelengths and higher temperature produces photons of shorter wavelengths. If one considers that the photons from the star are emitted from one optical depth, τ_λ, then the photons from the limb escape from a higher altitude of the stellar surface that has a cooler temperature, T_{low}, where the opacity is higher. In the same sense, one optical depth at the center of the star probes a deeper layer of the surface that is hotter, T_{high}, and the opacity lower, hence it appears brighter (Fig.1.4).

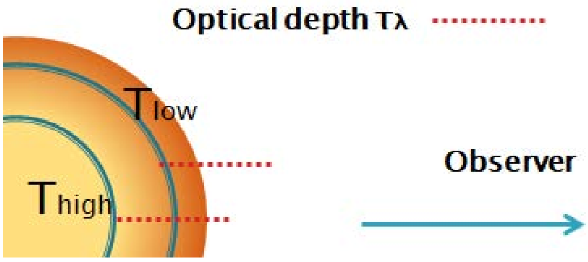

Figure 1.4: Geometry of the limb darkening phenomenon and the changes of the stellar brightness due to this effect.

This decrease of the intensity has an important effect on the shape of the received light curves from a transiting event of an exoplanet. However, this phenomenon can be handled in the transit modeling of a light curve, with the use of laws. The Limb

Darkening Laws (LDLs) are based on $\mu = cos\theta$, with θ being the angle between the normal to a given point on the star's surface and the line of sight. There are numerous works in the literature discussing extensively this effect and the employed laws and coefficients, e.g., Claret (2000); Sing et al. (2009); Sing (2010); Espinoza & Jordán (2016); Neilson et al. (2017); Howarth (2011). In this dissertation, there are employed two of the most widely used LD laws for transit light-curve modeling (e.g., Espinoza & Jordán 2015), the quadratic law:

$$I(\mu) = I(1)\Big[1 - u_1(1-\mu) - u_2(1-\mu)^2\Big], \tag{1.1}$$

and the nonlinear four-parameter LD law:

$$I(\mu) = I(1)\left[1 - \sum_{n=1}^{4} C_n(1-\mu^{n/2})\right], \tag{1.2}$$

with u_1 and u_2 being the coefficients of the quadratic LD law and C_1, C_2, C_3, C_4 being the coefficients of the four parameter LD law.

In Fig. 1.5, it is presented an illustration of the LD's influence on a set of simulated transit light curve models. The models are developed for a hot-Jupiter type exoplanet with inclination $i = 89.9°$, semi-major axis $a = 8R_s$, transit depth $(R_p/R_s)^2 = 2\%$. This hypothetical system orbits a star with effective temperature of $T_{\text{eff}} = 4500$ K, logarithm of the surface gravity $\log g = 4.5$, and solar metallicity. The transit models were created with the use of the BATMAN package, which stands for "BAsic Transit Model cAlculatioN in Python" (Kreidberg 2015), and they are referred to observations at different wavelengths, using Sloan Digital Sky Survey (SDSS) u',g',r',i' and z' filters. Specifically, for this example, the employed LDL is the quadratic law, while the coefficients for each bandpass are calculated using the Exoplanet Characterization Toolkit, EXOCTK, based on Kurucz ATLAS9 (Kurucz 1979) stellar model atmospheres [6]. There is an evident change to the light curve shape as we observe this transiting event from near-infrared wavelengths (e.g., flatter bottom of the curve, shallower transit depth) towards the ultraviolet wavelengths (e.g., V-shaped curve, deeper transit depth).

Therefore, the LD effect of the host star, if not correctly modeled in a transit light curve analysis, can be a possible driver for changes in the transmission spectra, since it affects the determination of the transit depth and the R_p/R_s value. Especially, in conjunction with a poorly determined impact parameter value, b, in the fitting process, the LD effect can have a significant influence on the derived spectra.

1.6 The impact parameter degeneracy

Atmospheric investigations through transmission spectroscopy are sometimes impaired due to different factors, e.g., underestimated systematics, different assumptions during the data analysis processes, different LD laws and LDCs, or stellar variability (e.g., starspots). One more specific factor to consider is the choice of the impact parameter, b, of the system:

$$b = \frac{a}{R_s} cosi, \tag{1.3}$$

---

[6] https://exoctk.stsci.edu

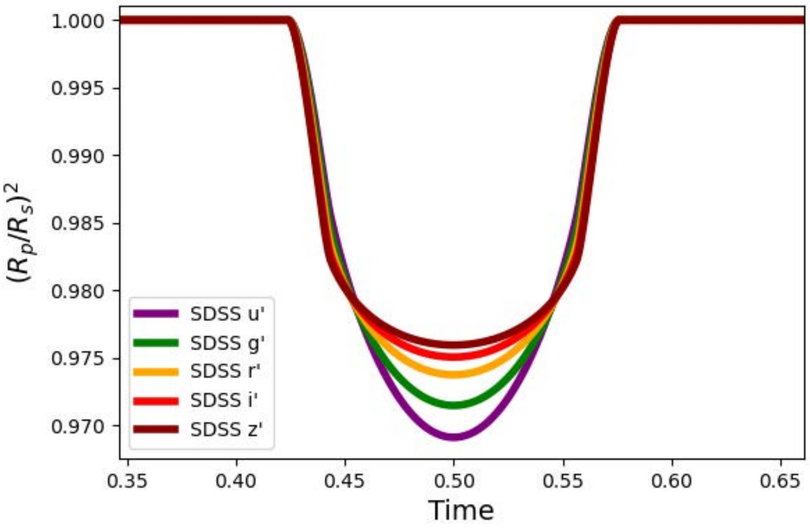

Figure 1.5: Simulations of transit light curves showing the influence of the stellar limb darkening. It is seen as a progressive change in the shape of the light curve and the transit depth, as we observe from near-infrared towards ultraviolet wavelengths.

with a/R_s being the semi-major axis in units of stellar radii and i being the system's inclination. As presented in Fig. 1.6, the impact parameter indicates the trajectory of the transit with respect to the equator of the star. When a planet transits the star centrally, $b = 0$, and when it transits over the stellar limb, then $b = 1$. The simulated received light curves are retrieved using the BATMAN package (Kreidberg 2015), the quadratic LD law, and coefficients from EXOCTK, based on Kurucz ATLAS9 stellar model atmospheres, for a star similar to the one in Sec 1.5, observed at red wavelengths. All the other planetary and system parameters are the same as in Sec 1.5 as well, with the only difference the variable inclination values ($i = 83°$, $i = 84°$, $i = 86°$, and $i = 89.9°$), employed in a way to yield the corresponding b in the lower part of the image, and denoting different orbital trajectories around the star. The four transit light curves have been chosen for illustration purposes, to show how the curves change progressively from $b = 0.01$ (orange curve, for an almost centrally crossing transit) to $b = 0.97$ (red curve, for a transit over the stellar limb). The transit shape changes from U-shaped to V-shaped, and the transit depth becomes shallower because the planet blocks a part of the star, which appears darker than the center of the star.

The choice of b during a transit light curve fit, essentially directs the planet towards a specific trajectory around the star; if this b value is not precise, then potentially unreal changes on the transmission spectrum might occur. A change in the transit depth due to incorrect use of b translates directly to a deviating value than the true R_p/R_s. The degeneracy, created by b shaping the transmission spectrum, might be another potential reason that leads to discrepancies in atmospheric characterization.

The impact parameter degeneracy was suggested in the work of Alexoudi et al. (2018) (hereafter, A18), in order to clarify the atmospheric inconsistency reported for the exoplanet HAT-P-12 b (Hartman et al. 2009). There were two contradicting

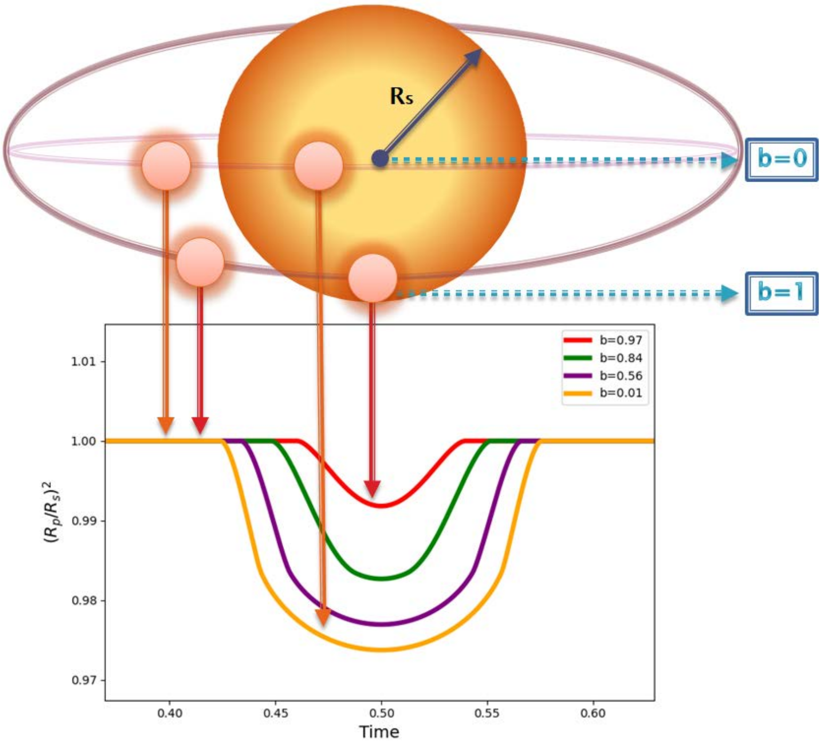

Figure 1.6: Illustration of a transiting system of an exoplanet and its host star. The received brightness of the event over time is shown in the form of transit light curves. Four cases are considered: 1) the planet transits its star centrally at $b = 0.01$, and yields U-shaped light curves (orange solid curve) and 2) the planet transits over the limb at $b = 0.97$, and yields V-shaped light curves (red solid curve). 3) and 4) are intermediate cases with $b = 0.56$ (purple solid curve) and $b = 0.84$ (green solid curve), which are shown in order to demonstrate the progressive shape change, with a direct change of R_p/R_s. This is due to variations in the employed inclination of the system in the transit light-curve fit analysis. Considering all other parameters similar, only the inclination value is changing in the fit process in order to demonstrate the principle of the impact parameter degeneracy described in the text.

characterizations for the atmosphere of HAT-P-12 b. The first team, Mallonn et al. (2015) (hereafter, M15), using ground-based observations, derived a flat spectrum, indicative of clouds in the atmosphere of this exoplanet. The second team, Sing et al. (2016) (hereafter, S16), used spectroscopic observations of the Hubble Space Telescope (HST) and found a hazy atmosphere, described by a strong Rayleigh scattering slope. The discrepancy is evident at the bluer wavelengths of the transmission spectra in Fig.1.7 (comparison between M15 and S16). With a homogeneous re-analysis of all datasets and the use of new ground-based light curves, A18 identified that the discrepancy is closely linked with the impact parameter of the system. The two different groups had used a different inclination value, hence impact parameter value ($b_{S16} = 0.37 \pm 0.05, b_{M15} = 0.21 \pm 0.06$), forcing this way the planet to have a different trajectory around the host star during the data analysis. Evidently, the limb darkening of the star acted as a driver for the phenomenon, trying to push the model towards an unreal transit depth estimation. With a common inclination value derived from the entire set of the ground-based datasets, yielding $b_{A18} = 0.24 \pm 0.04$, a new transmission spectrum of HAT-P-12b was formed, and it is presented in Fig. 1.7 (blue squares denote ground-based observations and blue dots indicate the reanalyzed HST data).

What was identified as "impact parameter degeneracy" in A18, might be a potential explanation for other discrepancies reported in the literature (see Table 1.1).

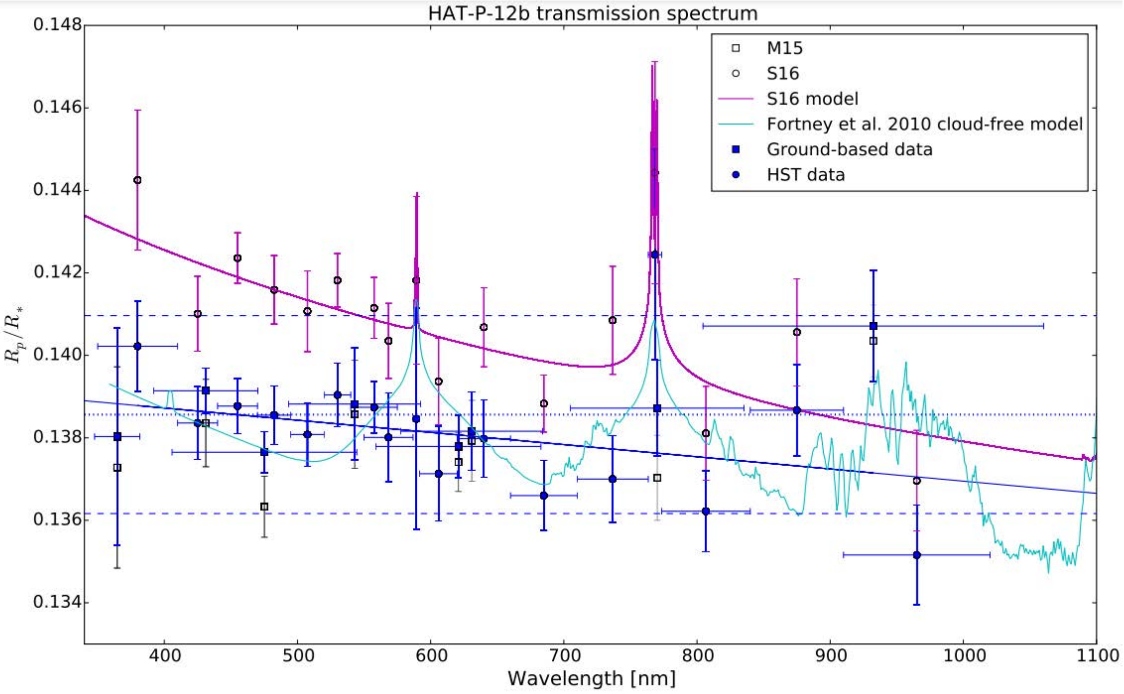

Figure 1.7: Transmission spectrum of HAT-P-12b as derived from the homogeneous reanalysis of all data from the ground and from the HST with their associated error bars. For reference and comparison, we overplot the values obtained by M15 (black empty squares). The blue dashed lines show plus-minus two scale heights from the weighted average value of R_p/R_s (blue dotted line). In magenta, we show the values of S16 together with the suggested atmospheric model (magenta solid line). The cyan solid overplotted line represents the cloud-free, solar-composition model of HAT-P-12b from Fortney et al. (2010) for comparison. The blue solid line is a linear regression of the weighted R_p/R_s values. Also, Fig. 8 in Alexoudi et al. (2018). Credit: Alexoudi et al., A&A, vol. 620, A142, p.8, 2018, reproduced with permission © ESO.

2 Motivation and Objectives

2.1 Motivation of this thesis

The main motivation of this doctoral dissertation is to assess the degeneracy between the optical slope and the impact parameter at its infancy, and to quantify this phenomenon in terms of transmission spectroscopy. Motivated strongly by the results in Alexoudi et al. (2018), where the degeneracy of the planetary spectral slope with the orbital parameters is confirmed, it is particularly interesting to investigate if this idea could be applicable to further reported inconsistencies (see an example of some systems in Table 1.1) and resolve them. More specifically, if a change in the inclination of the system can cause a slope in the transmission spectrum (as with the HAT-P-12 b atmospheric investigation), then this might be a potential reason for other reported discrepancies. Even though this dependency of the orbital parameters with the optical slope is also described briefly in Pont et al. (2013), it was not proved that an implemented inaccurate and smaller inclination in the light curve analysis could potentially fabricate a Rayleigh slope in the spectrum. A proof of such a phenomenon is found in the work of Alexoudi et al. (2018). Therefore, when a reported atmospheric discrepancy is not caused by e.g., the different analysis tools, limb darkening laws, or limb darkening coefficients, then it is suggested to search for deviations in the employed orbital parameters, especially in the value of the inclination i. Assuming i and a/R_s (where a is the semi-major axis and R_s is the stellar radius) as wavelength independent and being fixed during the fit process, one should be cautious and use the most precise value available, in order to avoid questionable atmospheric characterizations.

The first goal of this dissertation is to clarify whether a transmission slope is a product of the exoplanet's atmosphere or of non-precise parameters used for the analysis of the transit light curves.

2.2 Exoplanet atmospheric investigation with simulated transit light curves

In order to accomplish an extensive investigation of the impact parameter degeneracy with the spectral slope, one possible method is to use noise-free, simulated light curves of transiting events. Some reasons for atmospheric inconsistencies might be, among others, systematic effects from the instruments and the Earth's atmosphere, third light contamination from another star in the system or partial transiting events and hence not enough observational cadence. With simulations, one can test a perfect case in which the light curves come from the transit event itself and solely from the objects of interest, which is the planet and its host. It is fundamental to understand from where this effect finds its source and persistence. Some misin-

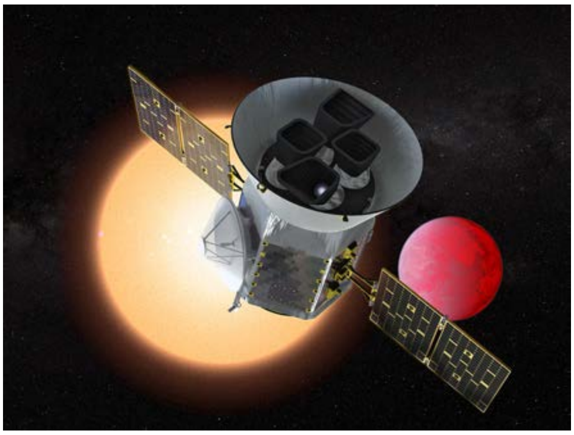

Figure 2.1: Illustration of NASA's TESS in front of a lava planet orbiting its host star. Image Credit: NASA.

terpretations and discrepancies in the literature can possibly be explained by the impact parameter degeneracy, demonstrating that the limited precision of the transit parameters has an important effect on the transmission spectra. Knowing the drivers for this phenomenon, one can avoid ambiguous interpretations and contradicting results of atmospheric characterizations, and can contribute in optimizing the quality of the scientific output.

2.3 Photometry with TESS

Photometry with space-based instruments can overcome systematics introduced by the Earth's atmosphere (e.g., seeing, atmospheric absorption) in the received light curves. Moreover, high-quality and uninterrupted datasets can benefit systems that were observed before with low photometric precision or with partial transits. When partial transits are observed, the derived b and R_p/R_s measurements are biased. The lack of information from a well established baseline before and after the transit event can compromise a R_p/R_s determination, while the lack of information about the ingress/egress (when the planet starts to transit the star and when it ends its transit), can hamper a correct determination of the orbital parameters (Winn et al. 2009). Therefore, the need of uninterrupted datasets is important, and this is one of the main attributes that the Transiting Exoplanet Survey Satellite (TESS) can provide.

TESS is a NASA mission specifically dedicated to the search for transiting exoplanets around nearby stars (Ricker et al. 2015). TESS's mission is a near all-sky survey, focused especially in finding smaller planets than Neptune in a 2-year prime mission interval. It was launched in April 2018 and the operations started in July of the same year. After two years of successful observations, TESS started its first extended mission, while two years later, in September 2022, it got a further extension. Even though TESS uses a single optical-red bandpass that ranges from 600 to 1000 nm (central wavelength = 786.5 nm), it still can be a valuable tool for characterization of exoplanetary atmospheres (e.g., Carter et al. 2020; Daylan et al. 2021; Yang et al. 2022). TESS can provide, with high quality uninterrupted photometry, precise orbital parameters, hence impact parameter estimations, from short period exoplanets. The continuous monitoring of each sector of approximately 27-days, can yield many transiting events for some systems, from which we can derive physical and orbital parameters with the highest precision. Exoplanet atmospheric models can benefit strongly from this. Moreover, the transit depth measurements derived with TESS will add one high precision estimation of R_p/R_s on the transmission spectra. This single information, coming from TESS, is important to establish, for example, the presence of clouds in an exoplanetary atmosphere or the presence of water vapor in the near-infrared wavelengths (e.g., in the z' band, Yang et al. (2022)). TESS was designed to be a substantial improvement for data collection on smaller exoplanets, with radii less than Neptune (Barclay et al. 2018). In connection with RV measurements of those systems, TESS will re-establish the mass-radius diagram while it will simultaneously provide targets for atmospheric studies with JWST (Gardner et al. 2006) and later on with ARIEL (Tinetti et al. 2018). Another, goal of TESS is to find terrestrial exoplanets around M-dwarfs or planets with longer orbital periods. Furthermore, TESS can also be useful in two other scientifically challenging cases, that are investigated through this doctoral thesis: 1) in providing precise parameters for inflated hot Jupiter type exoplanets and 2) in providing precise parameters for grazing exoplanetary systems. The first case is explored in Chapter 5. Inflated hot Jupiters need a precise determination of their planetary radii, for the correct modeling of their atmospheres and structure. TESS is expected to be particularly useful with photometric observations of irradiated exoplanets and provide high precision of their radii and other orbital parameters. The second case is addressed thoroughly in Chapter 6. Even though there are successful detections and characterizations of grazing systems from the ground, (e.g., Mancini et al. 2014), sometimes grazing systems are difficult to characterize, due to their special orbital configuration. According to this, the planets are not able to transit their host stars centrally, but rather over the limb. A possibly poor estimation of the planetary radii in this case, and the pronounced limb darkening of the stellar surface, sometimes yield system parameters with large uncertainties. This is where TESS photometry is valuable for grazing targets, in order to precisely access their properties.

3 Overview of the included manuscripts

Some of the work presented in this thesis has been published in the peer-reviewed journals noted in their respective references. An overview of these manuscripts is presented here, along with information on the authorship and the contributions of each author, as well as a brief description of the context of the manuscripts within the thesis as a whole.

Manuscript I: "On the role of the impact parameter in exoplanet transmission spectroscopy", Astronomy and Astrophysics, Volume 640, Article Number A134, August 2020 [1]

Authors: X. Alexoudi[1,2,3], M.Mallonn[1,3], E.Keles[1,3], K. Poppenhaeger[1,3],C. von Essen[4] and K. G. Strassmeier[1,3]

[1]Leibniz Institute for Astrophysics Potsdam (AIP), An der Sternwarte 16, 14482 Potsdam, Germany
[2]Potsdam Graduate School, Am Neuen Palais 10, 14469 Potsdam, Germany
[3]Universität Potsdam, Institut für Physik und Astronomie, Karl-Liebknecht-Straße 24/25, 14476 Potsdam, Germany
[4]Stellar Astrophysics Centre (SAC), Department of Physics and Astronomy, Aarhus University, Ny Munkegade 120, 8000 Aarhus C, Denmark

Contribution: This article presents, in both qualitative and quantitative ways, the influence of incorrect parameters in a transit light curve fit has on a transmission spectrum of an exoplanetary atmosphere. I created the synthetic light curves and the simulations of their planetary atmospheres, hence the visualization of the expected optical slopes and their uncertainty envelopes. Dr. Matthias Mallonn provided examples of discrepancies in the literature that could possibly be explained by this work. I wrote the manuscript with input and assistance of Dr. Matthias Mallonn and Prof. Dr. Klaus G. Strassmeier. All of the authors participated in discussions of the results and contributed with helpful comments.
In the context of this thesis: This is the first publication of my thesis aiming to clarify the discrepant results regarding the atmospheric characterizations of individual exoplanets, reported in the literature. The estimated transmission spectra

---

[1] Credit: Alexoudi et al., A&A, vol. 640, A134, 2020, reproduced with permission © ESO.

deviations are closely linked to the employed orbital parameters of the star-planet systems and the limb-darkening effects of their host stars. With this work, I demonstrated that the uncertainty on the orbital parameters corresponds to an uncertainty on the spectral slope. I performed a qualitative and a quantitative study to illustrate the effect and to create an error envelope of the possible variations of the spectral slope with the different changes in the impact parameter. My simulations have shown a wavelength dependent offset that is more pronounced at the bluer wavelengths (since the limb darkening effect is stronger). Some discrepancies in the literature can possibly be explained by this effect, named "Impact Parameter Degeneracy”, as it can clarify ambiguities regarding atmospheric characterization of exoplanets.

Manuscript II: "On the parameter refinement of inflated exoplanets with large radius uncertainty based on TESS observations", Astronomical Notes, Volume 343, Issue 3, March 2022.

Authors: X. Alexoudi[1,2,3],
[1]Leibniz Institute for Astrophysics Potsdam (AIP), An der Sternwarte 16, 14482 Potsdam, Germany
[2]Potsdam Graduate School, Am Neuen Palais 10, 14469 Potsdam, Germany
[3]Universität Potsdam, Institut für Physik und Astronomie, Karl-Liebknecht-Straße 24/25, 14476 Potsdam, Germany

Contribution: This is a single author paper where I explored the photometric capabilities of TESS on a small sample of inflated hot-Jupiters. I identified the targets of interest, and I generated a photometric transit pipeline to obtain the publicly available TESS light curves. I performed the data analysis, with further detrending and transit modeling. Then, I interpreted the results and reported all the findings in this manuscript. This is my first independent work.

In the context of this thesis:

One of the most powerful instruments photometrically during the course of this doctoral thesis is the TESS mission. With this publication, I investigated how high quality datasets from space can improve our knowledge on outdated radii estimations from the ground. Uninterrupted transit light curves provided from TESS can help ameliorate major system parameters, especially the planetary radius that can be directly derived from the transit depth for systems that were reported with large radii uncertainties. The correct measurement of the transit depth is important in order to understand the chemical composition of an exoplanetary atmosphere at the wavelength of observation. Moreover, a more precise estimation of the impact parameter of the system can prevent potential discrepancies regarding its atmospheric characterization. A single measurement provided by TESS can still differentiate between a featureless spectrum and elemental absorption in an atmosphere. With this work, I revisited known inflated exoplanets and confirmed or refined their major system parameters, aiming to evaluate TESS's photometric capabilities in terms of precision, and to avoid future misinterpretations of their atmospheres.

Manuscript III: "Comparative study of nearly-grazing and fully-grazing exoplanet system parameters derived with TESS and ground-based instruments", Astronomical Notes, ASNA20220075

Authors: X. Alexoudi[1,2,3], E. Dineva [1], S. Barnes[1], and K. G. Strassmeier[1,2]

[1]Leibniz Institute for Astrophysics Potsdam (AIP), An der Sternwarte 16, 14482 Potsdam, Germany
[2]Universität Potsdam, Institut für Physik und Astronomie, Karl-Liebknecht-Straße 24/25, 14476 Potsdam, Germany
[3]Potsdam Graduate School, Am Neuen Palais 10, 14469 Potsdam, Germany

Contribution: The conception and outline of the objectives of this project was initiated by me. As a continuation to my previous project, I wanted to investigate systems with $b > 0.6$ in order to test if their radii are overestimated from the ground-based observations reported in the literature. The TESS data are publicly available and pre-processed at a certain degree. The data retrieval, further reduction, analysis, and visualization of the final results was conducted by me. Dr. Ekaterina Dineva provided helpful comments regarding the physics of the stellar radiation and the nature of the stellar spectrum. Moreover, she encouraged valuable discussions on ground-based observation specifics. Dr. Sydney Barnes provided useful guidance and suggested the Figures 6.3, 6.8 and 10.2, which gave clarity to the objectives of this manuscript. Prof. Dr. Klaus Strassmeier provided guidance and advised on the conduction of this work. All co-authors assisted in proofreading.

In the context of this thesis: In my first publication, one of the main outcomes, was that grazing systems are more likely to suffer from imprecision in the orbital parameters and yield vulnerable transmission spectra. The error envelope is larger for those systems and the effect of the impact parameter degeneracy becomes stronger, with steeper slopes at the blue wavelengths. Also, in my second publication, I identified a trend that planetary radii might be overestimated by ground-based investigations for systems that have a large impact parameter ($b > 0.6$). Grazing systems are interesting to investigate with high quality photometry because they usually lack information on ingress and egress from the ground-based works, and this compromises the accuracy of the derived transit depth, hence the spectral slopes and atmospheric characterization of those systems. Considering the impact parameter degeneracy and the effects of the limb darkening that are stronger towards the limb of the star, grazing systems are particularly difficult to characterize due to their geometry (shape of the transit light curve). For this reason, the atmospheric characterization of grazing systems is a challenging endeavor. Building on this, in this third publication we provide refined/confirmed planetary radii and impact parameters for a large sample of transiting exoplanets with $0.6 < b < 1.0$, with TESS observations. We compare them with previous ground-based investigations to test the hypothesis that the radii are always overestimated, and eventually we re-assessed the grazing nature of those systems. Some of them are not in the grazing regime after this investigation. The refinement of the orbital parameters for (nearly-) grazing systems, is essential in order to avoid future atmospheric discrepancies.

4 Role of the impact parameter in exoplanet transmission spectroscopy

Credit: Alexoudi et al., A&A, 640, A134, 2020, reproduced with permission © ESO.

4.1 Abstract

Transmission spectroscopy is a promising tool for the atmospheric characterization of transiting exoplanets. Because the planetary signal is faint, discrepancies have been reported regarding individual targets. We investigate the dependence of the estimated transmission spectrum on deviations of the orbital parameters of the star-planet system that are due to the limb-darkening effects of the host star. We describe how the uncertainty on the orbital parameters translates into an uncertainty on the planetary spectral slope. We created synthetic transit light curves in seven different wavelength bands, from the near-ultraviolet to the near-infrared, and fit them with transit models parameterized by fixed deviating values of the impact parameter b. First, we performed a qualitative study to illustrate the effect by presenting the changes in the transmission spectrum slope with different deviations of b. Then, we quantified these variations by creating an error envelope (for centrally transiting, off-center, and grazing systems) based on a derived typical uncertainty on b from the literature. Finally, we compared the variations in the transmission spectra for different spectral types of host stars. Our simulations show a wavelength-dependent offset that is more pronounced at the blue wavelengths where the limb-darkening effect is stronger. This offset introduces a slope in the planetary transmission spectrum that becomes steeper with increasing b values. Variations of b by positive or negative values within its uncertainty interval introduce positive or negative slopes, thus the formation of an error envelope. The amplitude from blue optical to near-infrared wavelength for a typical uncertainty on b corresponds to one atmospheric pressure scale height and more. This impact parameter degeneracy is confirmed for different host types; K-type stars present prominently steeper slopes, while M-type stars indicate features at the blue wavelengths. We demonstrate that transmission spectra can be hard to interpret, basically because of the limitations in defining a precise impact parameter value for a transiting exoplanet. This consequently limits a characterization of its atmosphere.

4.2 Introduction

Studying transiting exoplanets has been one of the highlights of the past 20 years in astronomy. Since the development of suitable instrumentation and techniques, the transit events permit us to even probe the atmospheres of exoplanets and allow a glimpse in their interiors (e.g., Charbonneau et al. 2002). One approach for exploring the atmosphere is employing of low-resolution transmission spectroscopy, which is a very effective method for investigating large gas giant exoplanets, such as the so called hot Jupiters. Its principle is that the effective radius of a planet depends on the wavelength. This wavelength can be measured during a planet transit (planet passes in front of its host star), and the planetary atmosphere can be seen to interact with the starlight. When we measure the ratio of the planet-to-star radius over wavelength, we obtain a transmission spectrum (e.g., Kreidberg 2018). Transmission spectra can reveal a wealth of features in an atmosphere, such as signatures of Rayleigh scattering toward shorter wavelengths, which is attributed to aerosols or H_2, and clouds, atomic, and molecular absorption from Na and K, $\mathrm{H_2O}$, AlO, TiO, or VO (e.g., Sing et al. 2016; Mallonn & Strassmeier 2016; Kreidberg et al. 2018; Nikolov et al. 2018; Tsiaras et al. 2018; Mancini et al. 2019; von Essen et al. 2019). One drawback is that the spectral slope can be mimicked by other effects, for instance, third-light contamination from a stellar companion or the potential activity of the host star, for example, spots and faculae (McCullough et al. 2014; Oshagh et al. 2014; Rackham et al. 2018). It is difficult to interpret the slope at optical wavelengths, and it can result in inconsistencies in the atmospheric characterization of exoplanets.

The literature lists several cases of independently derived transmission spectra of individual targets that deviate significantly. Numerous authors suggested that these reported discrepancies might be solved by a homogeneous reanalysis of the individual datasets to avoid systematic effects originating from differences in data reduction or data analysis. A successful application was presented by Alexoudi et al. (2018), who reanalyzed the data of two independent studies on the hot Jupiter HAT-P-12b. The two previous investigations, Mallonn et al. (2015) and Sing et al. (2016), derived inconsistent conclusions on the planetary atmosphere; the former found a flat optical spectrum, while the latter concluded that HAT-P-12b has a Rayleigh scattering slope toward the blue wavelengths. The probable source of this deviation was the use of different values of the orbital inclination in the two analyses. The difference of these inclination values was about 2.2σ. By applying a common inclination value in a simultaneous transit fit to the acquired datasets (both ground- and space-based), all data yielded consistent results. The authors finally concluded that weak scattering at short optical wavelengths is present in the planetary atmosphere.

Motivated by the discovery of this effect in HAT-P-12b transmission spectra, we present in this work an extended investigation of this phenomenon. With noise-free, simulated light curves, we prove here that the limited precision in the knowledge of the transit parameters can affect the transmission spectra, and lead into misinterpretations and discrepancies in the literature.

In Section 4.3 we present the methods that were employed in our work. In Section 4.4 we address the effect of the orbital parameters on the transmission spectra with simulations and through two different approaches. This confirms a degeneracy with the spectral slope. Then, we investigate the extension of this effect on a sample of hot Jupiters with different types of host stars. In Section 4.5,we aim to explain some of the known discrepancies from the literature that are due to the aforementioned effect, and in Section 4.6 we summarize our work and present our final conclusions.

4.3 Methods

One of the fundamental steps in a light-curve analysis is fitting a transit model on a given dataset. Typically, the transit-model fit parameters are the orbital period of the system P, the inclination i, the semimajor axis in units of stellar radii a/R_s, the transit depth in terms of the ratio of planet to stellar radii (R_p/R_s), the limb-darkening (LD) effect, expressed using different LD laws (LDL) and coefficients (LDCs), the midtime of the transit and the contribution of a third light term in the light curve.

Investigations of low-resolution transmission spectroscopy often start with the analysis of a white-light curve, which is the light integrated over the entire observed wavelength range. Such a light curve normally holds a low value of photon noise and therefore presents high photometric precision. This precision allows determining the entire set of model parameters. In the next step, the observed wavelength range is split into numerous wavelength channels to create a chromatic set of light curves and investigate the wavelength dependence of transit parameter of interest, here mainly R_p/R_s. Because the chromatic light curves are of lower photometric precision, all parameters that are not expected to vary with wavelength are normally kept fixed to their values derived in the previous white-light curve fit. These achromatic parameters also include those describing the planetary orbit. The planetary trajectories around their host stars can be tracked with the use of the impact parameter b. This is the relation between the orbital inclination and the semimajor axis, according to the following expression (Winn 2009; Haswell 2010):

$$b = \frac{cos(i) \times a}{R_s.} \tag{4.1}$$

However, the observed uncertainties in i and a/R_s allow for a range of b values. If the uncertainty in b is large, then the planet might apparently follow different pathways over its host, and because the stellar surface does not have a homogeneous brightness, the effect of the LD becomes important. We are interested in studying whether this range in allowed pathways over the host star might result in an uncertainty of the derived values of R_p/R_s over wavelength, that is, the planetary transmission spectrum. Eventually, we wish to describe the extension of this effect with respect to the atmospheric pressure scale height H of an exoplanetary atmosphere. The scale height is a quantity according to which we can estimate the size of the absorbing annulus of the planetary atmosphere, as defined by the expression (Winn et al. 2010)

$$H = \frac{k_B \ T_{eq}}{\mu_m \ g}, \tag{4.2}$$

where k_B is the Boltzmann constant, T_{eq} is the equilibrium temperature, μ_m is the mean molecular mass, and g is the local gravitational acceleration.

4.4 Results

4.4.1 Impact parameter degeneracy

Ideally, individual investigations of the atmosphere of the same exoplanet would yield consistent results, but this is not always the case: the literature includes reported discrepancies regarding the atmospheric characterization of exoplanets. When the authors do not agree at the same employed parameter values in the light-curve analysis, then inconsistent transmission spectra might appear. This is especially evident when different works use very different orbital parameters of i and a/R_s, and hence a different b value. In this section we focus on the effect of the choice in b on synthetically retrieved transmission spectra of transiting exoplanet events, and more specifically, their spectral slopes. We address the problem of the effect on the spectral slope when the analysis involves fixed orbital parameters, i and a/R_s, on values that yield different impact parameters for the system.

For this purpose, we simulated noise-free light curves in multiple wavelength bands by assuming a hot Jupiter exoplanet that is on a circular orbit of a K-type host star with $T_{\text{eff}} = 4500$K, surface gravity of log $g = 4.5$, and solar metallicity. The orbital period is set to 3.32 d. The orbital inclination of the system is $i = 90°$, the semi-major axis is $a = 8\ R_s$, and the planet transits its host centrally at a trajectory defined by an impact parameter $b = 0$. We used the four-parameter LD law to simulate the stellar LD, with coefficients from Claret & Bloemen (2011). We defined a transit depth of 2% ($R_p/R_s = 0.14142$). The synthetic light curves were created with a custom pipeline using PyAstronomy[1] and the analytical transit models of Mandel & Agol (2002). We worked with sets of seven chromatic light curves of different bands (Johnson/Cousin U, B, V, R, I, J, and H) and we did not consider any out-of-transit variations.

We focused on the consequences that the forced alterations of the orbital parameter values might have on the derived transmission spectra when their combination yields different or similar b values. We therefore kept i and a/R_s fixed to values that deviate from their original ones during the application of a transit model fit. We used the OneDFit class, which is an object-fitting base class of PyAstronomy. It provides a suitable interface for the Nelder-Mead simplex, which is a parameter-fitting algorithm, in order to determine the best-fit solution. In Table 4.1 we present the values we adopted to create the light curve and the altered values that were kept fixed at the subsequent model fitting. The only free parameters during the fit were R_p/R_s and the orbital period P. To illustrate the individual effects of deviations in i, a/R_s, and b on the retrieved transmission spectrum, we varied i and a/R_s by unusually high values, much higher than their typical uncertainties. It was therefore necessary to also vary P accordingly to achieve a reasonable model fit to the simulated data. This was done by including P in this part of the work as free-to-fit parameter.

In Fig.4.1 we present the transmission spectra derived with this approach. They clearly show a wavelength-dependent offset in R_p/R_s. The nine parameter sets of Table 4.1 overlap in three sequences, indicating the parameter sets with the same b value. They are distinguished by different symbols for each Δb configuration. Even when the values for i and a/R_s are very different, we obtain the same offset if the

---

[1] https://github.com/sczesla/PyAstronomy

Table 4.1: Setup of the orbital parameters i and a/R_{star} of the transit light-curve simulations presented in Fig. 4.1

	i	a/R_{star}	b
simulated	90	8	0
fitted	89.28	8	0.1
	88.57	8	0.2
	87.85	8	0.3
	89.05	6	0.1
	88.09	6	0.2
	87.13	6	0.3
	89.43	10	0.1
	88.85	10	0.2
	88.28	10	0.3

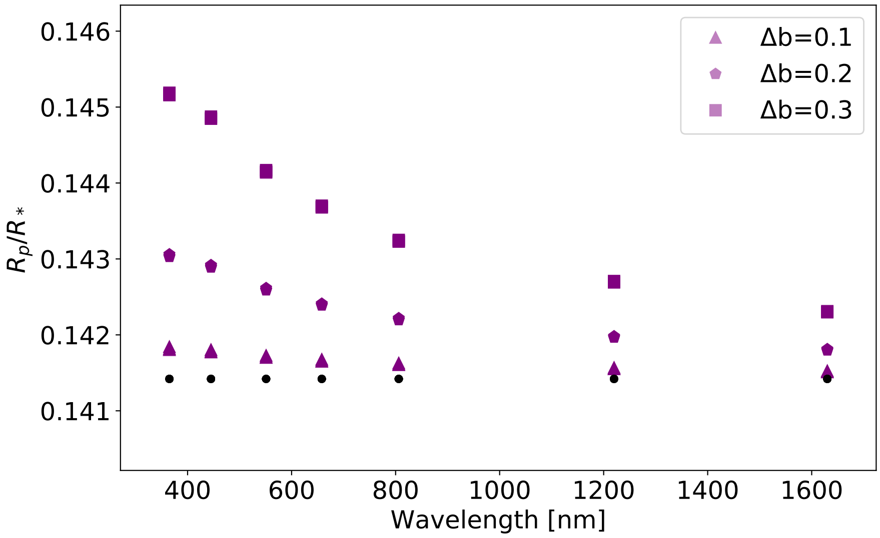

Figure 4.1: Synthetic transmission spectra for transiting exoplanets. We show the spectral slopes derived with fixed orbital parameters in combinations that yield the same impact parameter. The symbols indicate the different variations in b. The nine configurations of Table4.1 overlap in three sequences according to their Δb deviation from the original setup (black dots).

parameter combinations result in the same b. This can be compared to the initial setup value of the simulations for R_p/R_s. With this qualitative approach, we wish to highlight that this wavelength-dependent offset in R_p/R_s depends mainly on b, not on i or a/R_s separately, and that it is more pronounced toward shorter wavelengths. This introduces a slope in the spectra. This offset has a strong nonlinear exponential dependence with the deviation in b, and it is basically driven by the LD of the host star.

The offset in the derived R_p/R_s can be explained as follows: When we fix b to a different value than the true input value, the planet is forced toward a deviating trajectory. The fit compensates for the different brightness of the host star that is due to LD along this trajectory by a planetary radius R_p different from the input radius, causing the offset. In synthetic light curves, where the host star LD is switched off, no offset in R_p/R_s is found. Hereafter, we call this effect the "impact parameter degeneracy".

4.4.2 Formation of an uncertainty envelope

The uncertainty in b is able to modify the transmission spectrum, as we demonstrated in the previous paragraph. In order to quantify the effect of a typical uncertainty in b on the transmission spectra through the impact parameter uncertainty, we obtained the impact parameter and its uncertainty for a total sample of 349 hot Jupiters from the NASA Exoplanet Archive (Akeson et al. 2013). We split our sample into three groups of interest according to their b values: centrally to off-center (group A includes 181 exoplanets with $0.0 < b < 0.5$), off-center to nearly grazing (group B includes 82 exoplanets with $0.5 < b < 0.7$), and totally grazing (group C includes 62 exoplanets with $0.7 < b < 1$) transiting exoplanets. For each group, we derived the median parameter values and median uncertainties and show them in Fig. 4.2. The uncertainty Δb decreases with increasing b because Δi is determined more precisely for higher b values. The b values and their median uncertainties that we used here as typical Δb for each subgroup are $b_A = 0.28 \pm 0.09$, $b_B = 0.6 \pm 0.04$, and $b_C = 0.82 \pm 0.02$. To simulate the effect of the typical impact parameter uncertainty, we created one synthetic light curve per group and per filter with the median b and performed a transit model fit by fixing b to values corresponding to plus and minus the median Δb. To this end, we always fixed $a/R_s = 8$ and adopted

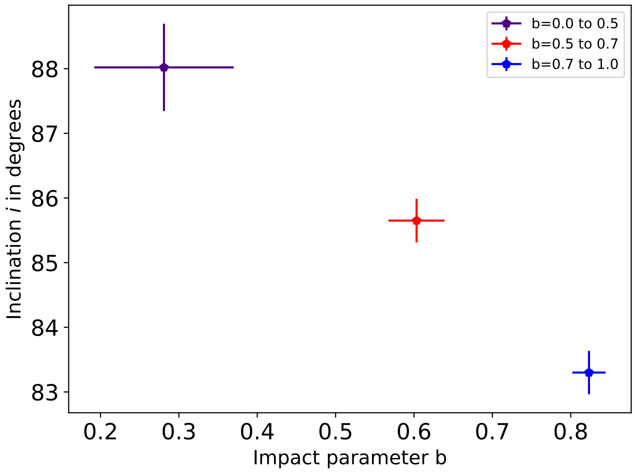

Figure 4.2: Median inclination values and their uncertainties with respect to the median b values and their uncertainties in b of the different subgroups of exoplanets. Purple values represent group A, red values group B, and blue values group C

.

i to yield the demanded b value. The orbital period was again set to 3.32 days, and the LD was treated using the four-parameter law. The adopted LDCs from Claret & Bloemen (2011) correspond to an average K-type host star from our sample with $T_{\rm eff}$=5000K, surface gravity of $\log g = 4.5$, and solar metallicity. The only parameter that was free to fit per light curve was R_p/R_s. In contrast to our exercise in Section 4.4.1, we varied i by only low values and kept the parameter P fixed to its input value. This reflects the typical situation of P being fixed during the fit of the multiwavelength transit light curves because it is usually known to high precision. An example of the fits of these synthetic light curves is presented in Fig. 4.3.

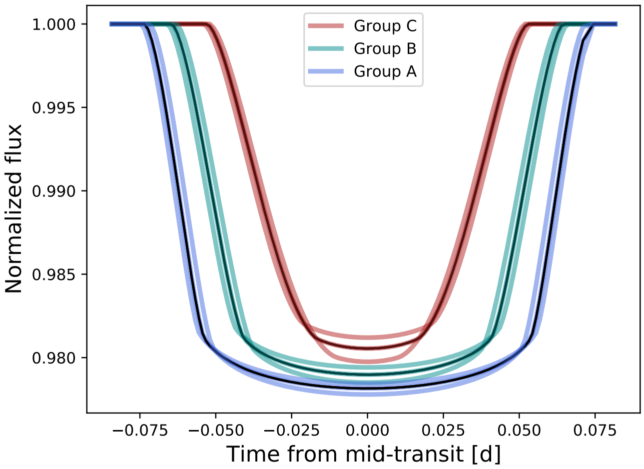

Figure 4.3: Example of the synthetic light-curve fit for each subgroup.

The results show the deformations of the spectra that are caused by changes in b of each subgroup; they are presented in Fig. 4.4.The deviation in b in opposite directions, according to plus and minus the uncertainty, result in an opposite offset in R_p/R_s, and the formation of an uncertainty envelope. The deviation in b towards a centrally or grazing transiting configuration (lower or higher b value) results in a positive or negative slope in the transmission spectrum. We calculated the slope values, which are equal to $-1.37 \pm 0.27 \times 10^{-6}$ nm^{-1} for group A, $-1.58 \pm 0.31 \times 10^{-6}$ nm^{-1} for group B, and $-1.73 \pm 0.23 \times 10^{-6}$ nm^{-1} for group C, for the effect of $+\Delta b$. Because the uncertainty envelope closes with the effects due to $-\Delta b$, the estimated slope values of the opposite direction are $0.88 \pm 0.19 \times 10^{-6}$ nm^{-1} for group A, $1.28 \pm 0.25 \times 10^{-6}$ nm^{-1} for group B, and $1.38 \pm 0.26 \times 10^{-6}$ nm^{-1} for group C. The slopes clearly increase slightly from a central toward a grazing transit geometry.

In the physical interpretation of the derived transmission spectrum, a rise of R_p/R_s toward shorter wavelengths can be conceived as scattering of a hazy atmosphere, probably due to small particles (e.g., Pont et al. 2013; Mallonn & Wakeford 2017; MacDonald et al. 2020). We conclude that a flat spectrum (initial assumption of our simulation) might appear sloped and can be misinterpreted as Rayleigh absorption. Moreover, the opposite, a flat spectrum, might be the outcome of using a lower b, and a plausible Rayleigh feature is obscured with such a configuration. Alternatively, a planet without an atmosphere can be considered to have an atmosphere for the same reasons as previously because a spectral slope appears at shorter wavelengths,

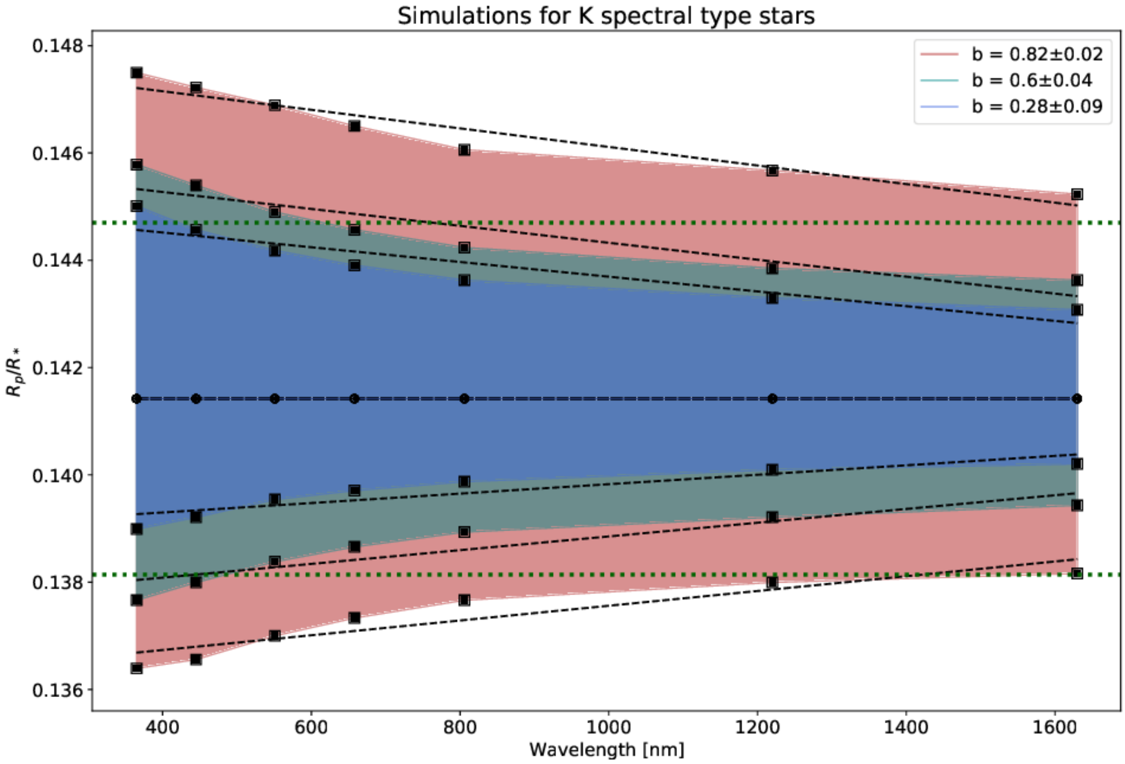

Figure 4.4: Effect of $b \pm \Delta b$ on the transmission spectra of three different groups of exoplanets (groups A, B and C), showing an introduced slope and an offset for different b values. Black dots show the synthetic spectra of each subgroup, and black squares show the respective derived spectra with the variation in b. The colored areas illustrate the error envelope for each case. Dashed black lines show the linear regression fits on each spectrum, and dotted green lines indicate two atmospheric scale heights from the predefined input value for R_p/R_s.

which is driven by the LD effect in the host star, and is due to a poor knowledge in b.

In transmission spectroscopy, the variation in R_p/R_s with wavelength is usually expressed in units of the atmospheric pressure scale height H. In order to examine the impact parameter degeneracy on the spectral slope in units of H, we determined a typical value of H for hot Jupiters that is suitable for transmission spectroscopy. We ranked all planets from the TEPCat (Southworth 2011) according to the amplitude of their potential transmission signal Δ_δ, estimated by Winn et al. (2010) to

$$\Delta_\delta = \left(\frac{R_p + N_H\ H}{R_s}\right)^2 - \left(\frac{R_p}{R_s}\right)^2, \tag{4.3}$$

with N_H as the number of scale heights, set to 1 for the purpose of our ranking. Then we formed a typical value by the average of the top-ranked 30 objects. The atmosphere of a typical hot Jupiter suitable for transmission spectroscopy causes a Δ_δ signal of $\sim 4.5 \times 10^{-4}$, and planets with smaller atmospheric scale heights cause significantly weaker signals. We obtained an average stellar radius of our sample of R_s=1$R_\odot$ and an average value for the atmospheric scale height of H=1140 Km. We conclude that a representative relative scale height of our sample is h=H/R_s=0.00164. In Fig. 4.4, we show two atmospheric scale heights of the average R_p/R_s input value (green dotted lines). Intriguingly, the relative R_p/R_s change over wavelength of the spectral slope is about one atmospheric scale height for hot Jupiters with a strong signal Δ_δ. The same amplitude of the impact parameter degeneracy corresponds to even higher values in units of H for exoplanets with weaker transmission signals.

4.4.3 Application on different stellar types

We focus on determining how the different host star properties, in terms of center-to-limb variations, change the derived transmission spectra. We used synthetic light curves with the same outline of orbital parameters as in Section 4.4.1 in order to investigate this scenario. We again considered a hot-Jupiter exoplanet with the same characteristics as previously. We investigated four additional categories to the former K-type host case: M-, G-, F-, and A- spectral types; this is a total of five different host categories. We addressed the LD effect using the four-parameter LDL and coefficients from Claret & Bloemen (2011), derived for a $\log g = 4.5$, solar metallicity, and for approximately a mean value of the different effective temperatures of each category of host stars ($T_{\text{eff}M}$=3800 K, $T_{\text{eff}G}$ = 5600 K, $T_{\text{eff}F}$ = 6250 K, and $T_{\text{eff}A}$ = 7500 K). All the parameters were kept fixed, except for R_p/R_s. We investigated the formation of the error envelope of the same subgroups as in Section 4.4.2 by adopting a different host star. The resulting transmission spectra of the different subgroups are shown in Fig. 4.5. The effect for A-type stars is slightly weaker than in M-type hosts. Interestingly, for M-type stars, we observe a feature at the blue wavelengths at 500nm that is persistent in all subgroups and might be linked to the wavelength dependence of the stellar LD effect. This feature is less pronounced in G-type hosts and A-type stars. F-type host stars exhibit the same shape as K-type stars. The derived slopes of each category (black dashed lines) are relatively similar, as is shown for $b + \Delta b$ in Fig.4.6, for example. However, for K-type host stars, the spectral slopes are steeper than in the other stars. In addition, a linear trend progresses from K-type host stars that is interrupted at G-type hosts stars and continues to F- and A- type hosts for all groups (A,B, and C) of transiting exoplanets.

4.5 Discussion

Some discrepancies have been reported concerning the slope at optical wavelengths in the atmospheric characterization of exoplanets. An explanation for these inconsistencies can be the impact parameter degeneracy with spectral slope, for instance, the case of HAT-P-12b in Alexoudi et al. (2018). Our work is able to show whether this controversy can be solved by a homogeneous set of orbital parameters.

4.5.1 Case of WASP-12b

We examined whether the discrepancy regarding two investigations on the atmospheric characterization of the ultra-hot Jupiter WASP-12b can be explained with

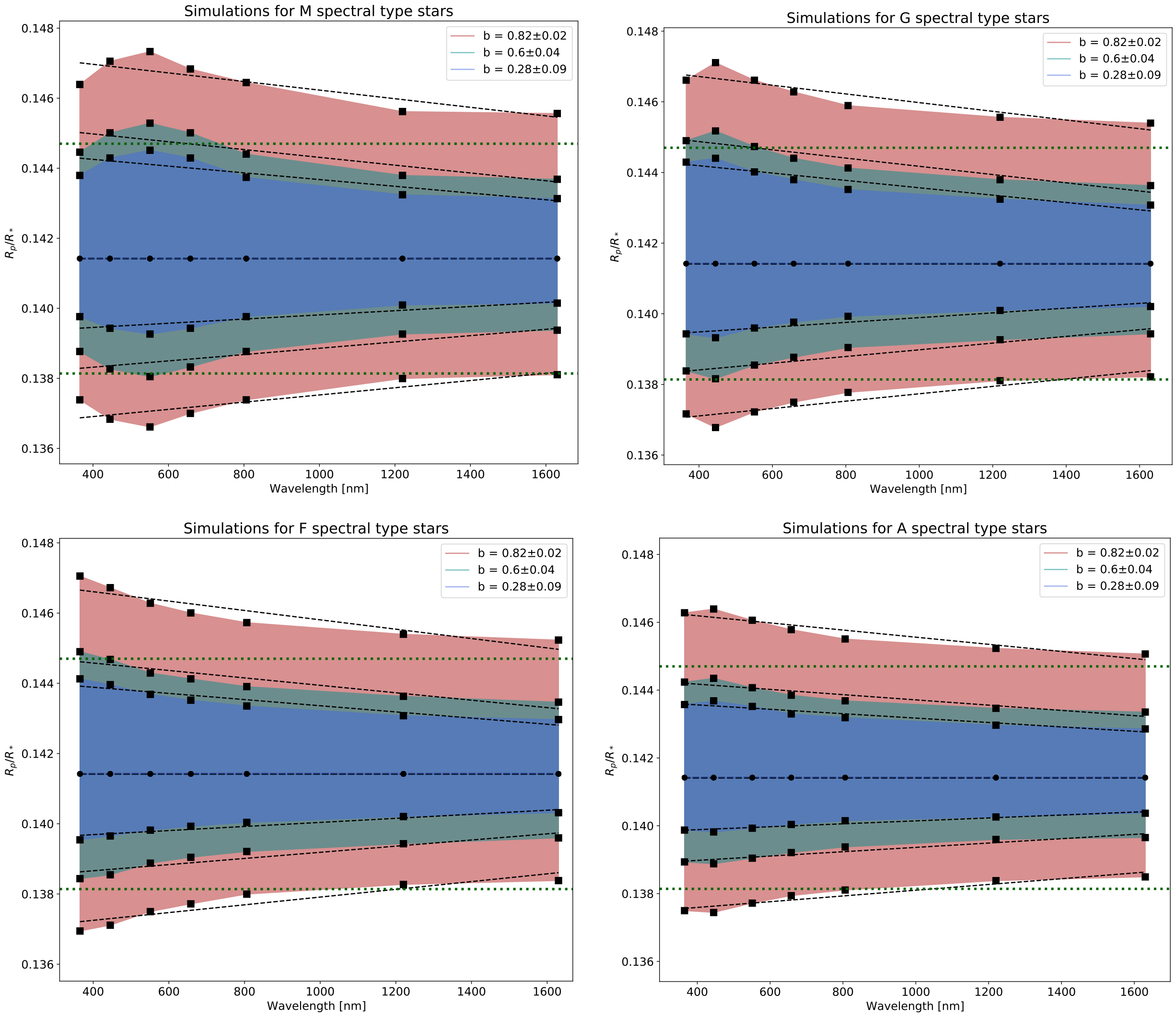

Figure 4.5: Simulations of variations that are due to the impact parameter degeneracy in the transmission spectra of the three different subgroups of exoplanets (groups A, B, and C), orbiting different categories of host stars. The upper panels show M- (on the left) and G- (on the right) and the lower panels F- (on the left) and A-type stars (on the right). The black dots indicate the flat synthetic spectra of each subgroup that we created with those configurations of the orbital parameters that yielded the median b value for each case. A combination of the orbital parameters at the transit model fit yields the spectra based on the change of $\pm\Delta b$ for each subgroup; this is indicated with black squares. The colored areas represent the error envelope. Dashed black lines show the linear regression fits on each spectrum, and the dotted green lines indicate two atmospheric scale heights from the average R_p/R_s value, as defined from the original setup for the transit depth.

the impact parameter degeneracy. Sing et al. (2013) (hereafter S13) demonstrated using the Space Telescope Image Spectrograph (STIS) on the Hubble Space Telescope (HST), that the transmission spectrum of this exoplanet shows a Rayleigh signature at the blue wavelengths. However, Stevenson et al. (2014) (hereafter S14),

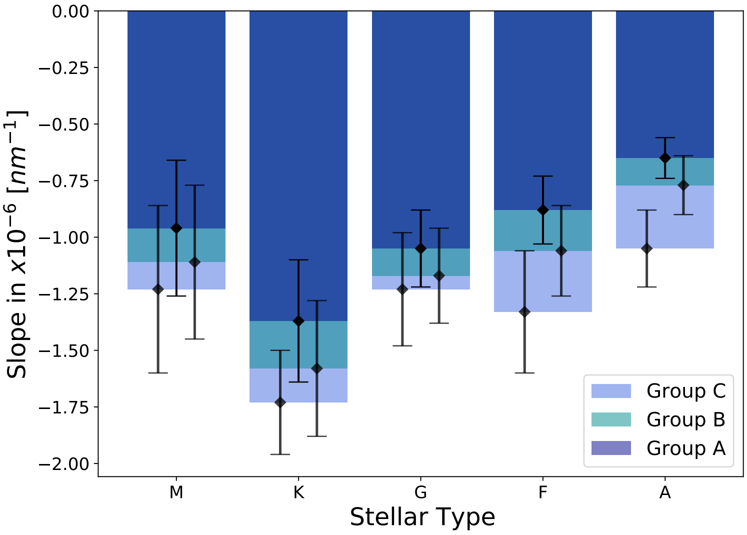

Figure 4.6: Comparison of the different slope values between the different spectral types of host stars for $b + \Delta b$ of each subgroup. K-type stars exhibit slightly steeper spectral slopes for the different subgroups of exoplanets. We offset the values of the x-axis arbitrarily for clarity.

using ground-based data from the Gemini Multi-Object Spectrograph (GMOS), determined a different impact parameter for the system and concluded that this is a spectrum with a much steeper slope than did S13 (Fig. 4.7). We investigated the impact parameter degeneracy by creating synthetic UBVRIJH light curves with the lower impact parameter value $b = 0.39$ from S13 and model-fit them with the fixed value of $b = 0.48$ from S14. We treated the LD effect using the four-parameter LDL and coefficients from Claret & Bloemen (2011), using the ATLAS model and the stellar characteristics for WASP-12 of S13 ($T_{eff} = 6500$, $\log g = 4.5$, [Fe/H] $=$ 0.0). As expected from our results in the previous sections, the higher b value of S14 results in a negative slope that is due to the impact parameter degeneracy, which we approximate by a linear regression line. We provide the linear slope y of the published transmission spectra of S13 and S14 in the third column of Table. 4.2, while the slope y' that is caused by the two different impact parameter values is given in the fourth column. The lower panel of Fig. 4.7 shows the two published slopes (solid lines) and the slope of S13 corrected for y' (dashed line). The correction brings the slopes of the two WASP-12b transmission spectra into better agreement. We therefore conclude that the impact parameter degeneracy might contribute significantly to the difference in the published planetary spectra.

4.5.2 Controversial results for WASP-80b

Sedaghati et al. (2017) (hereafter S17), using data from the FOcal Reducer and low dispersion Spectrograph (FORS) on the Very Large Telescope (VLT), reported a ground-based transmission spectrum of WASP-80b showing a pronounced optical slope, which the authors interpreted as a spectral signature of potassium (K). For the same exoplanet, Kirk et al. (2018) (hereafter K18), using the Auxiliary-port

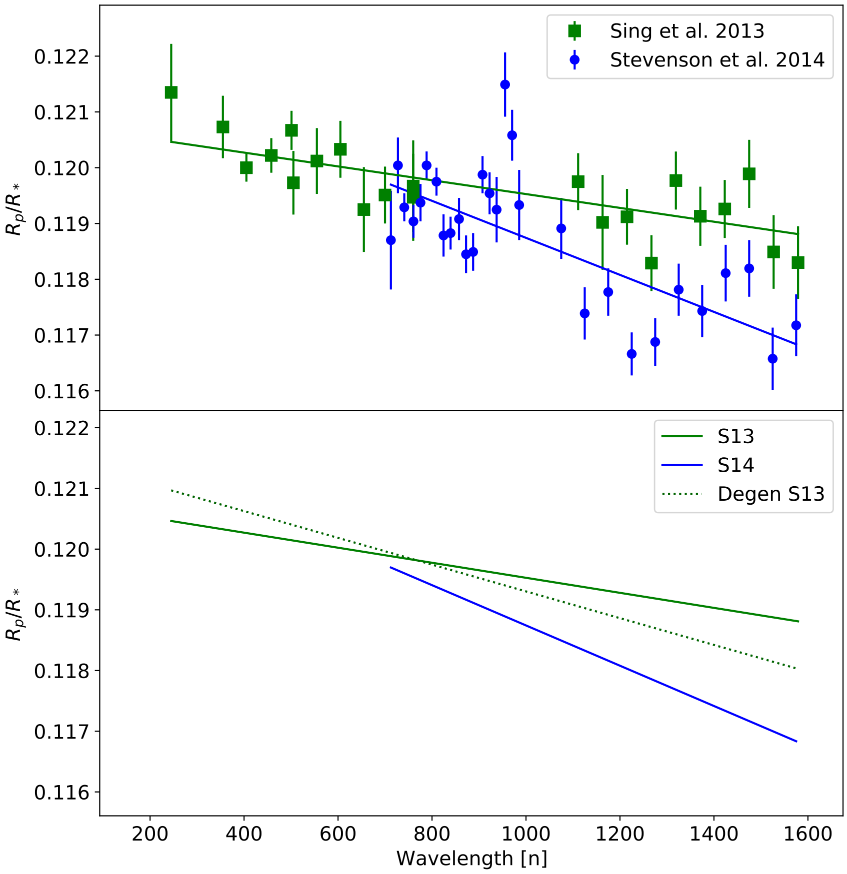

Figure 4.7: Discrepant case of WASP-12b investigations (upper panel) in the works of S13 (green squares) and S14 (blue dots). We fit the original spectra of S13 and S14 with regression line fits as solid green and blue lines, respectively. With our simulations (lower panel), we demonstrate the impact parameter degeneracy on the slope of S13 (green solid line). The synthetic light curves with the parameterization of S13 are fit with orbital parameters that yield the impact parameter of the S14 slope (solid blue line). Under this hypothesis, the S13 slope would be modified by an amount equal to the degenerated S13 slope (Degen S13, dotted green line).

CAMera (ACAM) on the William Herschel Telescope (WHT), concluded that it has an atmosphere that is dominated by haze based on a mild slope in their transmission spectrum, and they reported a non-detection of the previous potassium claim. A third work by Parviainen et al. (2018) (hereafter P18), using the Optical System for Imaging and low-Intermediate-Resolution Integrated Spectroscopy (OSIRIS) on the Gran Telescopio Canarias (GTC), yielded a flat spectrum that is indicative of high-altitude clouds for the atmosphere of WASP-80b. All three investigations fixed the impact parameter in their transit light-curve fit to different values. We study here whether these different assumptions can explain the different optical spectral slopes as a result of the impact parameter degeneracy. We created a set of UBVRIJH transit light curves with $b = 0.16$, which is the value used by P18.

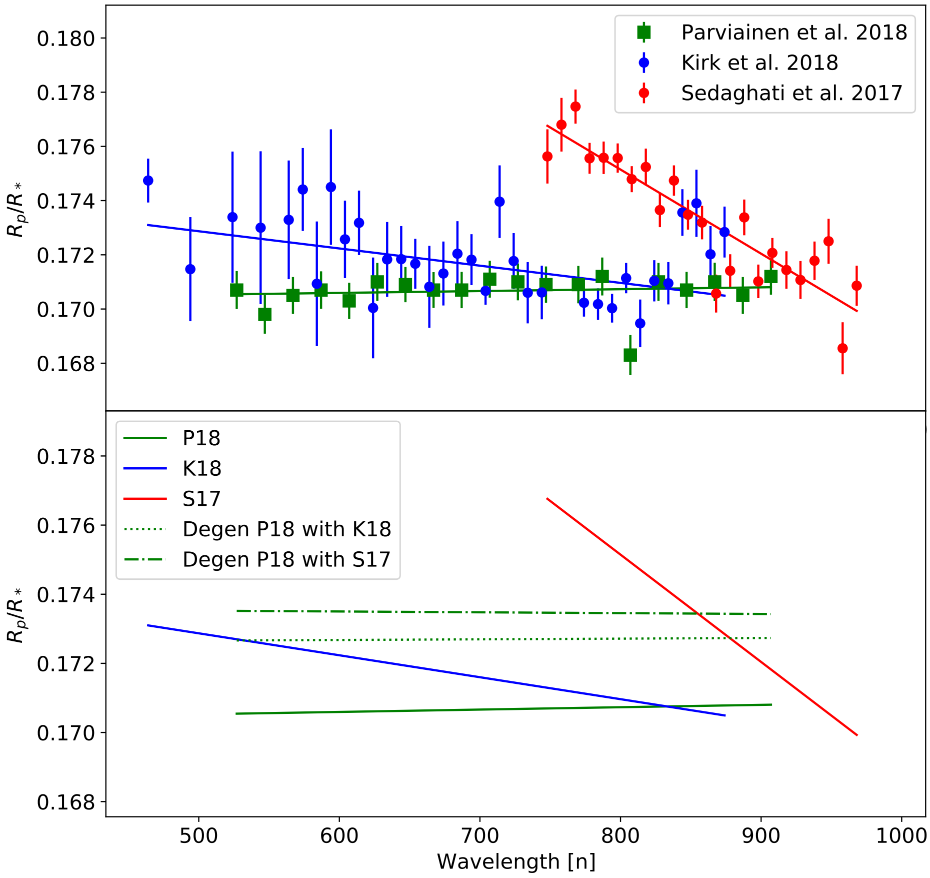

Figure 4.8: Spectral slopes from transmission spectroscopy investigations on WASP-80b by three individual groups (upper panel; P18 as green squares, K18 as blue dots, and S17 as red dots). The corresponding solid lines are regression line fits to each dataset. Synthetic light curves fit (lower panel) based on the parameters of P18 with transit models using the parameterization from K18 and S17, which yield different impact parameters than P18. The dotted green and dash-dotted green lines show the impact parameter degeneracy applied to the slope of P18, using the b terms from K18 and S17, respectively.

We used the four-parameter LDL and adopted coefficients obtained from Claret & Bloemen (2011). Then we fit these synthetic light curves with b fixed to 0.20 (K18), and in a second run to 0.23 (S17). The higher b values of K18 and S17 compared to P18 cause a negative slope y' by the impact parameter degeneracy, presented in Table. 4.2. However, this value amounts to only a small fraction of the differences in the published slope values. A portion of the Rayleigh slope reported by K18 might therefore be attributed to the impact parameter degeneracy. The very different measured slope of S17 compared to K18 and P18 cannot be explained by the impact parameter degeneracy because the slope value caused by the deviating b values in the synthetic spectra is negligible compared to the measured slope difference (Table 4.2). Effects different from the degeneracy studied here therefore apparently dominate in this case.

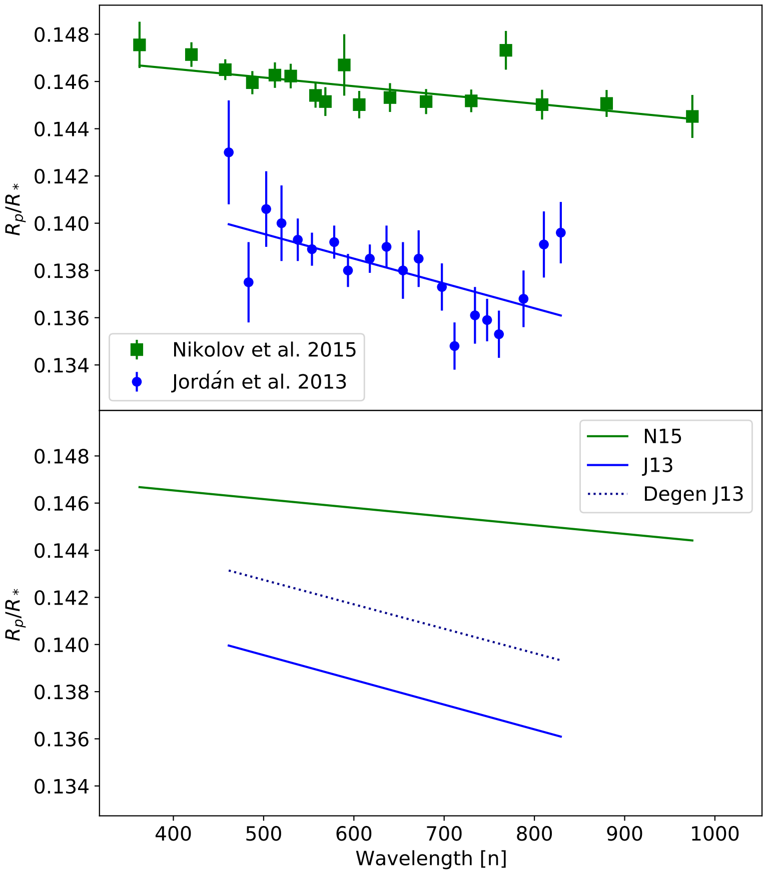

Figure 4.9: WASP-6b transmission spectra (upper panel) of N15 and J13 as green squares and blue dots, respectively, along with the solid green line and solid blue line as regression line fits to these datasets. Synthetic light curves of J13 (lower panel) with parameters that yield the impact parameter of N15. The contribution of this degeneracy to J13 is shown with a dotted blue line.

4.5.3 Inexplicable cases

The impact parameter degeneracy can be an explanation for parts of the reported discrepancies regarding the atmospheric characterization of exoplanets with respect to their spectral slopes. However, it is fails to clarify the inconsistencies in centrally transiting exoplanetary systems; especially when the individual analyses make use of a quite similar b value. For instance, the discrepancy on WASP-6b between Jordán et al. (2013) and Nikolov et al. (2015) (Fig. 4.9) cannot be explained. The two groups used similar b values, and their small difference causes only a very small slope y' when tested with synthetic light curves (Table 4.2). Therefore the different amplitudes of the discovered Rayleigh feature cannot be attributed to the impact parameter degeneracy.

Another case is HAT-P-32b. This exoplanet has been studied thoroughly in the literature (e.g., Gibson et al. 2013a; Mallonn & Strassmeier 2016; Nortmann et al. 2016; Tregloan-Reed et al. 2018; Alam et al. 2020). However, some investigations exhibit significant differences in the spectral slope of the obtained transmission spectra. We compare the results of Gibson et al. (2013b) (hereafter G13) and Mallonn

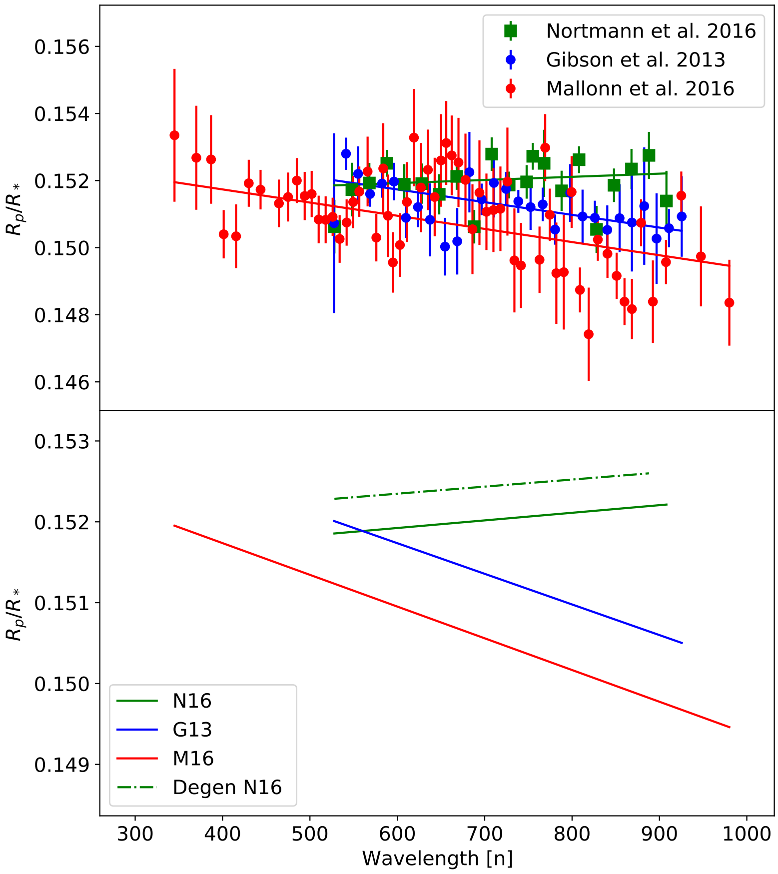

Figure 4.10: HAT-P-32b transmission spectra (upper panel). We present results from N16 (green squares), G13 (blue dots) and M16 (red dots). The corresponding solid lines represent linear regression fits of the different works. Synthetic transmission spectrum of N13 (lower panel) using the impact parameter obtained from G13 and M16. The N16 slope is corrected for by this amount caused by the impact parameter degeneracy (dash-dotted green line).

& Strassmeier (2016) (hereafter (M16) with the result of Nortmann et al. (2016) (hereafter N16). The first two studies achieve transmission spectra with a negative low-amplitude slope that might indicate scattering processes in the planetary atmosphere, and the result of N16 supports the scenario of a very flat spectrum. M16 used the same orbital parameter values as G13 in their light-curve analysis, while N16 used values resulting in a slightly different b value (Fig. 4.10). When we created synthetic light curves with the b value of N16 and fit them with b fixed to the value of G13 and M16, we obtained a slope caused by the impact parameter degeneracy of negligible gradient (Table 4.2). This follows our findings in previous sections that the impact parameter degeneracy is less important for centrally transiting systems and for a precisely determined impact factor b. Thus, the impact parameter degeneracy is certainly not the source of the deviating results of N16 and G13, and M16, on the optical spectral slope.

Table 4.2: Impact parameters from each study along with the gradient of the slope fit to the literature data (y) and the simulation slopes resulting from the impact parameter degeneracy (y'). By "input" we denote to the impact parameter value used to create synthetic light curves of a flat spectrum, and y' is the slope caused by fitting these synthetic light curves with the deviating impact parameter.

Planet	Reference	$y\,[\times 10^{-6}\ \mathrm{nm}^{-1}]$	$y'\,[\times 10^{-6}\ \mathrm{nm}^{-1}]$	b
WASP-12b	Sing et al. (2013)	-1.24 ± 0.25	input	0.39
	Stevenson et al. (2014)	-3.32 ± 0.62	-0.97	0.48
WASP-80b	Parviainen et al. (2018)	0.68 ± 1.28	input	0.16
	Kirk et al. (2018)	-6.35 ± 2.08	−0.49	0.20
	Sedaghati et al. (2017)	-31.05 ± 3.30	−0.92	0.23
HAT-P-32b	Nortmann et al. (2016)	0.94 ± 1.32	input	0.07
	Gibson et al. (2013b)	-3.79 ± 0.94	-0.07	0.09
	Mallonn & Strassmeier (2016)	-3.92 ± 0.94	-0.07	0.09
WASP-6b	Jordán et al. (2013)	-10.56 ± 3.28	input	0.26
	Nikolov et al. (2015)	-3.69 ± 1.11	-0.14	0.28

4.5.4 Impact parameter degeneracy versus other causes of spectral slope uncertainty

The case-by-case investigations of individual systems presented in the former sections showed that the impact parameter degeneracy is certainly not the only effect that can generate uncertainties in the optical slope of exoplanet transmission spectra. Many studies on the effect of dark or bright spots in the stellar photosphere have been conducted, which in the case of very active stars can cause optical slopes of larger amplitudes than the impact parameter degeneracy (McCullough et al. 2014; Oshagh et al. 2014; Rackham et al. 2018; Mallonn et al. 2018). However, for stars at about the low activity level of the Sun, the effect might be negligible. Third-light contribution of another star in the photometric aperture can also mimic a spectral slope. If it is uncorrected for, the amplitude of this effect can be stronger than the impact parameter degeneracy (e.g., Sing et al. 2013; Mallonn & Strassmeier 2016; von Essen et al. 2020). However, the Gaia satellite astrometry mission (Gaia Collaboration et al. 2018) has provided information on significant foreground or background objects to the exoplanet host stars, and a third-light correction can be performed with good accuracy. The choice of the stellar LD law or the estimation of the LD coefficients might also affect the planetary spectral slope. We tested the amplitude of this effect by creating synthetic UBVRIJH light curves with the four-parameter LD law and fit these noise-free data with transit models using the two-parameter quadratic LD law or the one-parameter linear law. We did not apply deviations from the orbital parameters, but kept them fixed to their input values. The only parameters left free to vary were the ratio of the planet-to-star radius. We derived values that deviated from the input value by an order of magnitude less than the impact parameter degeneracy for a typical uncertainty on b (Section 4.4.2).

Several of the individual planets we described above with discrepant published spectral slopes are inactive and either do not have a known third-light contribution, or a third-light correction has been performed using similar correction values. This means that none of the listed effects can explain the slope discrepancies. Our list of potential sources therefore appears to be incomplete, and other reasons such as different light-curve detrending approaches or systematics in the observing data might also play a role. For example, Nikolov et al. (2015) and Stevenson et al. (2014) compared their result on WASP-6b, respectively WASP-12b, to the previously published results of Jordán et al. (2013) and Sing et al. (2013), respectively, and argued that differences in the employed systematics model are a likely reason for an offset in R_p/R_s. We speculate that an offset like this might not be entirely achromatic, but wavelength dependent, and also affect the measured slope. The controversial results for WASP-6b, HAT-P-32b, and WASP-80b, for example, indicate that these systematics-related effects on the measured slope can be stronger than the impact parameter degeneracy.

4.6 Summary and conclusions

The limited precision in the determination of b in turn limits the characterization of exoplanetary atmospheres. We addressed the degeneracy of the spectral slope with this parameter through two main investigations, using synthetic noise-free light curves. First with a qualitative approach, in order to demonstrate that the changes in Δb affect the direction of the spectral slope, and then with a quantitative investigation to determine the error envelope of this effect for different groups of exoplanets, for which we applied typical measurement uncertainties in b. We conclude that the impact parameter degeneracy can be the driver of the spectral slope in both directions (positive and negative slopes), and it can transform flat spectra into sloped spectra, and vice versa. The effect persists with the use of different stellar hosts and yields steeper slopes for K-type hosts, but introduces a feature at the bluer wavelengths for M-type hosts.

The amplitude of the slope caused by the impact parameter degeneracy for a typical uncertainty in b is about one scale height over the optical wavelength range for a representative inflated hot Jupiter with a comparably large scale height suitable for transmission spectroscopy. For planets with smaller scale heights and therefore potentially weaker transmission spectroscopy signals, the amplitude of the impact parameter degeneracy amounts to even higher values in units of the scale height. Typical reported spectral slopes measured from observations are one to three scale heights in amplitude, therefore we consider the impact parameter degeneracy to be able to affect the measurements significantly.

We discussed the application of the degeneracy on a sample of reported discrepancies from the literature, but found no planet next to HAT-P-12b Alexoudi et al. (2018) for which the impact parameter degeneracy can fully explain the differences between reported optical slopes of its transmission spectrum. For WASP-12b, the degeneracy might partly be responsible for a reported discrepancy, but there are several other systems, for instance, WASP-80b, WASP-6b, or HAT-P-32b, for which the amplitude of a potential impact parameter degeneracy is negligible compared to the amplitude of the reported discrepancy. This illustrates that there is more than one source of error for the optical slope in exoplanet transmission spectroscopy.

As a consequence of the results, we suggest that the orbital parameter is not kept fixed in a model fit of the chromatic light curves when transmission spectra are extracted. We instead advise to let it remain a free parameter, potentially constrained by Gaussian or uniform priors. Another possibility is performing a similar exercise as done in this work and fixing the impact factor in a first run to its best-fit value, and compare the outcome of the transmission spectrum in a second run when the impact factor is changed by an uncertainty of about one sigma.

5 On the parameter refinement of inflated exoplanets with large radius uncertainty based on TESS observations

5.1 Abstract

We revisited ten known exoplanetary systems using publicly available data provided by the Transiting Exoplanet Survey Satellite (TESS). The sample presented in this work consists of short period transiting exoplanets, with inflated radii and large reported uncertainty on their planetary radii. The precise determination of these values is crucial in order to develop accurate evolutionary models and understand the inflation mechanisms of these systems. Aiming to evaluate the planetary radius measurement, we made use of the planet-to-star radii ratio, a quantity that can be measured during a transit event. We fit the obtained transit light curves of each target with a detrending model and a transit model. Furthermore, we used emcee, which is based on a Markov chain Monte Carlo approach, to assess the best fit posterior distributions of each system parameter of interest. We refined the planetary radius of WASP-140 b by approximately 12%, and we derived a better precision on its reported asymmetric radius uncertainty by approximately 86% and 67%. We also refined the orbital parameters of WASP-120 b by 2σ. Moreover, using the high-cadence TESS datasets, we were able to solve a discrepancy in the literature, regarding the planetary radius of the exoplanet WASP-93 b. For all the other exoplanets in our sample, even though there is a tentative trend that planetary radii of (near-) grazing systems have been slightly overestimated in the literature, the planetary radius estimation and the orbital parameters were confirmed with independent observations from space, showing that TESS and ground-based observations are overall in good agreement.

5.2 Introduction

The field of exoplanets is a rapidly advancing domain in modern astrophysics. Surveys and missions were dedicated through the years with joint ground- and space-based efforts in the discovery of exoplanets and the characterization of their interiors (e.g. The Hungarian Automated Telescope Network (HATNet) project (Bakos 2018), the SuperWASP: Wide Angle Search for Planets project (Street et al. 2003), the CoRoT project (Barge et al. 2008) and the Hubble Space Telescope (HST)). The results of these endeavors has shown that exoplanets are not similar to the planets of our solar system; increasing this way the interest of the scientific community to investigate further these unknown exotic worlds. For example, the Kepler mission (Borucki et al. 2010) (and later on the K2 mission (Howell et al. 2014), a follow-on to the Kepler mission), provided thousands of transiting systems, where the planet orbits its host star on an edge-on orbit, as seen by an observer on the Earth. Those systems included Earth-like planets, Neptune-sized, and interestingly large gaseous planets of the size of Jupiter at short orbital periods. However, most of Kepler's targets are faint stars, and the atmospheric characterization of large gaseous transiting exoplanets is favorable only for the brightest candidates.

One mission that is focused specifically on bright targets (5% on brighter than $V_{\mathrm{mag}} = 8$) is the Transiting Exoplanet Survey Satellite (TESS), which was launched in 2018 (Ricker et al. 2015) and it is scheduled to fixate its detectors on more than 100 exoplanets. For more than three years, TESS has been observing the night sky and has been providing datasets of photometric monitoring of bright stars and their planets, triggering follow-up studies by ground-based facilities and setting up the challenge for future space-born missions (e.g. the James Webb Space Telescope, JWST, of Gardner et al. (2006)).

The radii of inflated hot Jupiters, strongly affected by the irradiation of their host stars, extend beyond the typical Jupiter radius size. They can be determined from uninterrupted high-quality photometric light curves, always with respect to their host star radius measurement. The dimming in the brightness of these stars is larger for transiting gas giants with extended inflated radii. Even though, the planet radius estimation is derived straightforward from the planet-to-star radii ratio measurement during a transit event, the uncertainty on this measurement can be constrained significantly due to different factors; from unknown systematic errors to incomplete datasets, or a different approach on the methodology that was used for the transit light curve analysis. The required precision for the planetary radius measurement can contribute to the general understanding of the inflation scenarios taking part on different exoplanets.

Some of the most prominent mechanisms able to trigger the effect of inflation on gas giant exoplanets are: the irradiating flux sourcing from the host star itself, that heats up the planet and increases its equilibrium temperature (Guillot & Showman 2002), the ohmic heating mechanism (Laughlin et al. 2011), as a result from the coupling of the atmospheric flows with the magnetic field of the planet, the kinetic heating (a more direct mechanism), as some incident flux turns into kinetic energy and eventually into thermal energy that heats up the atmosphere. Last but not least, another mechanism is the tidal heating promoted by the circularization of the planetary orbit (Bodenheimer et al. 2001; Leconte et al. 2010). Evolutionary models that predict the formation mechanisms of inflated exoplanets can gain in robustness with the precise measurements of the key physical and orbital parameters of those exotic systems, and conclude to a suitable explanation for the applied inflation mechanism.

Moreover, studies on transiting exoplanets can yield an accurate planetary radius, that in combination with high precision radial velocity (RV) observations, can provide a mass for the planet, hence a mean density estimation which gives important information regarding the internal structure of these planets. Furthermore, the precise radius estimation and the distance from their hosts, can give insights on the gravitational potential of the planets and their equilibrium temperature. Consequently, those computations are useful in transmission spectroscopy because they

Exoplanet	TESS mag	P (d)	R_{p} ($\mathrm{R_J}$)	Date of last update	Publication
WASP-140 b	10.3	2.2	$1.440^{+0.42}_{-0.18}$	2016-11-30	Hellier et al. (2017)
WASP-136 b	9.5	5.2	1.380 ± 0.160	2016-11-30	Lam et al. (2017)
WASP-113 b	11.2	4.5	$1.409^{+0.096}_{-0.140}$	2016-07-14	Barros et al. (2016)
WASP-120 b	10.6	3.6	1.473 ± 0.096	2016-06-01	Turner et al. (2016)
WASP-93 b	10.6	2.7	1.597 ± 0.077	2016-09-06	Hay et al. (2016)
HAT-P-16 b	10.8	2.8	1.289 ± 0.066	2014-05-14	Buchhave et al. (2010)
WASP-123 b	10.4	3.0	1.318 ± 0.065	2016-06-01	Turner et al. (2016)
WASP-76 b	9.0	1.8	$1.830^{+0.060}_{-0.040}$	2016-01-20	West et al. (2016)
WASP-20 b	10.7	4.9	1.459 ± 0.057	2015-03-05	Anderson et al. (2015)
WASP-108 b	11.2	2.7	1.215 ± 0.04	2014-10-29	Anderson et al. (2014)

Table 5.1: The sample of this work. The sample selection is based on exoplanets with inflated radii ($R_{\mathrm{p}} > 1.2\mathrm{R_J}$), that orbit relatively bright stars (TESS mag < 12), in short orbital periods ($P < 5$ days). The planetary radius of each target has last been updated between the years 2014 and 2017, and therefore its refinement is necessary. The targets are sorted by the uncertainty on R_{p} with a decreasing order.

provide an estimation of the extension of an exoplanetary atmosphere, if it is present. The correct characterization of this, is based on the investigation of the planetary to stellar radii ratio over different wavelengths of observation, known as the transmission spectrum. The employment of incorrect parameters in the light curve analysis can compromise the structure of the spectrum and yield misplaced slopes (Alexoudi et al. 2020). TESS is expected to contribute to those studies by providing precise physical and orbital parameters derived from high-quality high-cadence datasets.

Motivated by the aforementioned capabilities of TESS, we obtained a sample of inflated hot giants, orbiting bright stars in short close-in orbits, and proceeded with a parameter refinement of those systems since their parameters have not been up-to-date for more than three years (see Table 5.1). The dates of the last update are presented as registered at the NASA Exoplanet Archive [1]. In this work, we focused on exoplanets with the largest reported planetary radius uncertainty, and we expected TESS to ameliorate our knowledge on the planetary radii of those systems and their physical properties. The aim is to provide the most accurate parameterization of these systems and quantify TESS's capabilities in comparison to the ground-based facilities.

The structure of this paper is the following: Section 5.3 presents the TESS observations of each exoplanet of our sample. In Section 5.4, we describe the reduction method that was employed for the analysis of these datasets and in Section 5.5, we demonstrate the adopted methods in order to derive the system parameters of our targets. In Section 5.6, we present our results and in Section 5.7 we discuss the impact of these findings regarding the characterization of hot giant exoplanets. In the end, in Section 5.8, we provide a summary and the conclusions of this entire work.

---

[1] exoplanetarchive.ipac.caltech.edu

5.3 Observations

Our sample consists solely of TESS observations, spanning the period of 2018-2021. We re-visited ten inflated hot giants (nine hot Jupiters and one Saturn-sized planet) using the publicly available, two-minute cadence data of TESS. The complete list of the observations is presented in Table 5.2. The obtained light curves were processed by the Science Processing Operations Center (SPOC) pipeline, based on the work of Jenkins et al. (2016). We made use of the PDCSAP_FLUX, which is the Pre-search Data Conditioning SAP flux, in order to access SPOC's data. PDCSAP_FLUX has an advantage over the simple aperture photometry (SAP_FLUX), because of the use of the Cotrending Basis Vectors (CBVs). CBVs remove longstanding systematic trends and provide better data quality (Tenenbaum & Jenkins 2018). Another approach would be to use the light curves derived from the data validation timeseries (DVT) files as in Ridden-Harper et al. (2020), however a standard process for the analysis of TESS data is the use of the PDC light curve (Shporer et al. 2019; Espinoza et al. 2020; Turner et al. 2021). With the use of PDCSAP products, we obtained light curves corrected for pointing and focus related systematics, for the cosmic rays' contribution to the detector, for persistent outliers and flux contamination (Jenkins et al. 2016). Moreover, we performed a further selection criterion on the datasets by masking out the bad cadences. During the observations some pixels may be contaminated by various effects e.g. spacecraft is in coarse point, reaction wheel desaturation event, cosmic ray detected, stray light from the Earth or Moon (see a complete set of such effects in Table 32 in Tenenbaum & Jenkins (2018)). To account for this, we used a conservative setting (in the lightkurve package - Lightkurve Collaboration et al. (2018)) in our analysis that excludes cadences with data-quality issues (Littlefield et al. 2019). All the cadences considered in this work are of high-quality, are products of the SPOC pipeline, and publicly available at the Mikulski Archive for Space Telescopes (MAST) [2].

5.4 Data analysis

We made use of Lightkurve (Lightkurve Collaboration et al. 2018), a Python package for Kepler and TESS data analysis. We cleaned additionally the light curves from outliers to the 6σ level, and normalize them by the median. We applied a further correction in the light curves by removing additional trends using the flatten method of the lightkurve package. This correction removes long-term trends using a Savitzky-Golay filter. We applied a window length of the filter of 1501 points and a break tolerance (in order to account for any large gaps in time) of 50. For each individual light curve of each sector, we applied a second order time-dependent polynomial, aiming to remove any remaining trends. We made use of the Bayesian Information Criterion, BIC (Schwarz 1978), to determine the best detrending model for our transit light curve fitting (Mallonn et al. 2015, 2016, 2019), and we concluded to a second order time-dependent polynomial that yields a smaller BIC value. In the end, we folded the light curves to a common transit mid-time reference of zero. Then, we used a combination of a detrending polynomial for the folded light curve and the Bad-Ass Transit Model cAlculatioN (BATMAN software

---

[2] https://archive.stsci.edu/

Target	Sector	Start Date	End Date	Cycle	Camera
WASP-140 b	4	$2018 - Oct - 18$	$2018 - Nov - 15$	1	2
	5	$2018 - Nov - 15$	$2018 - Dec - 11$	1	2
	31	$2020 - Oct - 21$	$2020 - Nov - 19$	3	2
WASP-136 b	29	$2020 - Aug - 26$	$2020 - Sept - 22$	3	1
	42	$2021 - Aug - 20$	$2021 - Sep - 16$	4	2
WASP-113 b	23	$2020 - Mar - 18$	$2020 - Apr - 16$	2	3
	24	$2020 - Apr - 16$	$2020 - May - 13$	2	2
WASP-120 b	4	$2018 - Oct - 18$	$2018 - Nov - 15$	1	3
	5	$2018 - Nov - 15$	$2018 - Dec - 11$	1	3
	30	$2020 - Sep - 22$	$2020 - Oct - 21$	3	3
	31	$2020 - Oct - 21$	$2020 - Nov - 19$	3	3
WASP-93 b	17	$2019 - Oct - 07$	$2019 - Nov - 02$	2	2
HAT-P-16 b	17	$2019 - Oct - 07$	$2019 - Nov - 02$	2	2
WASP-123 b	13	$2019 - Jun - 19$	$2019 - Jul - 18$	1	1
	27	$2020 - Jul - 04$	$2020 - Jul - 30$	3	1
WASP-76 b	30	$2020 - Sep - 22$	$2020 - Oct - 21$	3	1
	42	$2021 - Aug - 20$	$2021 - Sep - 16$	4	3
WASP-20 b	2	$2018 - Aug - 22$	$2018 - Sep - 20$	1	1
	29	$2020 - Aug - 26$	$2020 - Sep - 22$	3	1
WASP-108 b	11	$2019 - Apr - 22$	$2019 - May - 21$	1	2
	37	$2021 - Apr - 02$	$2021 - Apr - 28$	3	2
	38	$2021 - Apr - 28$	$2021 - May - 26$	3	2

Table 5.2: The TESS observations of each target, that were used in this work. We provide information on the sector, on the date, the observing cycle of each observation and the camera that was used. For many of the targets, there were available datasets of observations from multiple sectors.

by Kreidberg (2015)) in order to fit our data. We adopted initial model parameters as defined for each exoplanet from their discovery papers and used the Barycentric Julian Date as the Barycentric Dynamical Time ($\mathrm{BJD}_{\mathrm{TDB}}$) standard for the mid-time, as it is generally recommended being used in practice for astrophysical events (Eastman et al. 2010). We made use of the quadratic limb darkening law (Howarth 2011), and employed coefficients from the limb darkening calculator of the Exoplanet Characterization Toolkit[3]. We preferred limb darkening coefficients (LDCs) calculated with the ATLAS stellar atmospheric model grids, because there is an offset between the theoretical and the observed TESS LDCs when using the PHOENIX models, while using the ATLAS models there is a significantly smaller offset (Claret 2017). Then, we chose the traditional Cousins I - band, for the wavelength band for which to obtain the LDCs, because the TESS detector bandpass is centered on 786.5 nm[4]. And finally, we proceeded with the light curve fit process. That being the case, we kept all the parameters fixed to their theoretical values, except the time of the mid-transit T_0, the orbital inclination i, the semi major axis normalized in stellar radii a/R_{s}, the ratio of the planet to star radii $R_{\mathrm{p}}/R_{\mathrm{s}}$, and the three terms of the time polynomial c_0, c_1 and c_2. The orbital period P, the eccentricity e and the limb darkening coefficients remained fixed to their theoretical values during the fitting process. The free parameters were fit through the maximum likelihood optimization. For this purpose, we used the "optimize" module from SciPy [5], in order to apply a numerical optimization to the likelihood function and derive the parameters that maximize it. We made use of the maximum likelihood estimation of the free model parameters and employed the emcee [6] approach (Foreman-Mackey et al. 2013) to fit the combined transit model on the data and obtain posterior distributions for each parameter with errors. We used uniform prior values from where the emcee can draw samples in order to define the posterior values. The final probability function is a sum of the prior function and the likelihood function. We set the initialization of 30 walkers around the maximum likelihood estimations of each parameter and then run 20000 iterations. We access the samples using the “EnsembleSampler.get chain” method and identify the parameter values for each walker and for each iteration of the chain. The walkers initially wonder around the maximum likelihood values of each parameter, and then very quickly start to converge towards the full posterior distribution. There is a burnt-in phase of around 10000 steps. We ensured convergence of the chains with the integrated autocorrelation time τ metric, which computes the autocorrelation time of the emcee. Usually, chains longer than $50 \times \tau$ are sufficient and the burnt-in phase of 10000 steps ensured convergence for all the chains of the analyses of all our targets. Then, we thinned each chain and flatten it, so we would obtain a final flat list of samples. We present the best-fit parameters for each target in corner plots, where we can see the projections of the posterior probability distributions of our parameters. The 2-D histograms show the marginalized distribution of each. We used the uncertainties based on the 16th, 50th and, 84th percentiles of the samples. These confidence intervals correspond to $\pm 1\sigma$ for a Gaussian posterior distribution. The best fit of the modeled transit light curves and the corner plots of the analysis of each exoplanet of our sample are presented

---

[3] exoctk.stsci.edu/limb_darkening

[4] heasarc.gsfc.nasa.gov/docs/tess/the-tess-space-telescope.html

[5] https://docs.scipy.org/doc/scipy/reference/optimize.html

[6] emcee.readthedocs.io/en/stable/

in the Appendix A.

5.5 Derivation of the physical parameters

The investigation of inflated giant exoplanets with high-quality photometric TESS observations allows for a more concrete estimate of the properties of those systems. In our analysis, we adopted the values for the stellar radius R_s, the eccentricity e and the RV semi-amplitude of the stars $K_\star$, of these systems from their discovery papers. The newly derived parameters with TESS: T_0, $R_\mathrm{p}/R_\mathrm{s}$, a/R_s, i, can provide a refined measurement on their planetary surface gravitational acceleration, g_p and on their equilibrium temperature, T_eq. The updated R_p, being a direct connection to the density of these exoplanets, can yield a first characterization of their internal structure. Moreover, regarding the atmospheric characterization of these systems, we calculated a quantity that describes the relative atmospheric scale height of their atmospheres, H. With the measurement of H in km, we can define the extension of the absorbing annulus due to the planet's atmosphere. We made use of the equations from Southworth et al. (2007), Southworth et al. (2010), Winn et al. (2010), Seager (2011), Turner et al. (2016), Alexoudi et al. (2018), in order to compute all these quantities.

The surface gravitational acceleration is given by Eq. 5.1:

$$g_\mathrm{p} = \frac{2\pi}{P}\left(\frac{a}{R_\mathrm{p}}\right)^2 \frac{\sqrt{1-e^2}}{\sin\, i} K_\star, \tag{5.1}$$

The modified equilibrium temperature T_eq is as follows in Eq. 5.2:

$$T_\mathrm{eq} = T_\mathrm{eff}\left(\frac{R_\mathrm{s}}{2\,a}\right)^{1/2}, \tag{5.2}$$

where T_eff is the effective temperature of the host star.

We estimated the relative atmospheric scale height of the atmospheres of our sample using Eq. 5.3 (Winn et al. 2010):,

$$H = \frac{k_\beta\ T_\mathrm{eq}}{\mu_\mathrm{m}\ g_\mathrm{p}}, \tag{5.3}$$

where k_β is Boltzmann's constant, T_eq is the equilibrium temperature of the planet, μ_m the mean molecular mass and g_p the local gravitational acceleration. We adopt a mean molecular mass of approximately 2.3 amu, which is typical for a hot Jupiter exoplanet with a H/He dominated atmosphere (e.g. Sing et al. (2016)). Planets with large atmospheric scale height of many kms are excellent targets for atmospheric characterization through transmission spectroscopy (e.g. Burrows (2014); Mallonn et al. (2015); Sing et al. (2016)).

Moreover, TESS with uninterrupted datasets is expected to improve on the orbital parameters of those systems, hence we can provide a better constrained impact parameter b value for each one of them. The impact parameter is a quantity that shows the projected distance between the planetary center and the stellar center (Seager & Mallén-Ornelas 2003), and it is given by Eq. 5.4, where i is the inclination of the system and a/R_s is the normalized semi-major axis in units of stellar radii.

$$b = cos\,(i) \times a/R_\mathrm{s}. \tag{5.4}$$

5.6 Results

We used publicly available datasets from TESS with high-quality photometric precision in order to refine the parameters from ten inflated hot gas giant exoplanets. All the derived parameters from this work for each target are displayed in Tables 3-12, along with their 1σ uncertainty and a reference with their previously obtained parameters. In the following paragraphs, we shortly review each target, including some of their most important features, and present our results with a direct comparison between the individual investigations.

5.6.1 WASP-140 b

From the exoplanets observed with TESS and analyzed in this work, the one with the largest radius uncertainty is WASP-140 b (see Table 5.1). In the discovery paper (Hellier et al. 2017), WASP-140 belongs, according to previous observations, to a binary system. WASP-140 A is a K0 star, rather active, with an effective temperature of $T_{\text{eff}} = 5300 \pm 100$ K and $V_{\text{mag}} = 11.1$, while WASP-140 B is about 2 magnitudes fainter. The planet of this system, WASP-140 b, has a mass of 2.4M_J and an orbital period of $P = 2.2$ days. It orbits around the host star, WASP-140 A, on a grazing, at an impact parameter value $b = 0.93$, and eccentric ($e = 0.047 \pm 0.004$) orbit. WASP-140 b is a massive exoplanet with a short period of a significant eccentricity. All these characteristics of a hot Jupiter are not met usually around K-type stars, and maybe the studies of those are the key indicators to understand the magnetic activity of the host (Poppenhaeger & Wolk 2014). Interestingly, WASP-140 A is considered as a magnetically active star, as there are detected some star-spots on some light curves in the discovery paper. The presence of star-spots on the received light curves are able to alter the correct derivation of the transit depth and the correct measurement of the planetary radius (Morris et al. 2018; Oshagh et al. 2013).

We are interested to investigate this system with TESS and focus on the precise determination of its planetary radius. The large uncertainty of this radius measurement might be attributed to the grazing nature of this system and/or the partial transits reported from ground-based observations. The activity of the host cannot be ruled out, either, as a contributor to this radius uncertainty value.

TESS observed WASP-140 b during the sectors 4, 5 and 31. A total of 28 available light curves were employed in this work to derive the properties of WASP-140 b. Since, WASP-140 system is a known binary with TESS Input Catalog (TIC) identifiers for both stars, the SPOC pipeline estimates a dilution factor and corrects for the amount of the light contamination in the final light curve (Thompson et al. 2016). This dilution metric is named "CROWDSAP" and it is presented on the header of the TESS target pixel files (TPFs). For WASP-140 b, we obtain an average of 0.85 as a crowding estimation, for all the sectors of observation. This value signifies that the contamination of the received flux by nearby sources, is approximately 14%. According to Guerrero et al. (2021), "CROWDSAP" values of less than 0.8 are not trustworthy regarding photometric measurements, therefore for WASP-140 b TESS observations, the resulting light curves can be considered as photometrically reliable, since they are not contaminated severely by the companion.

In Fig. 9.1, we present the TESS folded light curves of WASP-140 b and the

Table 5.3: Physical properties of WASP-140 b as derived in this work from the modeling of the TESS light curves and the emcee analysis, in comparison to the previously published work of Hellier et al. (2017).

	This work	Hellier et al. (2017)
Parameters [units]	Values $\pm 1\sigma$	Values $\pm 1\sigma$
T_c [BJD$_\mathrm{TDB}$]	$2456912.35261 \pm 0.00016$	$2456912.35183^{*} \pm 0.00015$
i [°]	84.30 ± 0.06	$83.3^{+0.5}_{-0.8}$
a/R_s	8.58 ± 0.06	7.98 ± 0.39
$R_\mathrm{p}/R_\mathrm{s}$	0.1464 ± 0.0010	$0.1656^{**}{}^{+0.0494}_{-0.0216}$
b	0.851 ± 0.011	$0.93^{+0.07}_{-0.03}$
R_p [R$_\mathrm{J}$]	1.27 ± 0.06	$1.44^{+0.42}_{-0.18}$
ρ_p [ρ_J]	1.19 ± 0.17	0.8 ± 0.4
$\log g_\mathrm{p}$ [cgs]	3.592 ± 0.009	3.4 ± 0.2
T_eq [K]	1270 ± 25	1320 ± 40
H [km]	123 ± 4	-

* Converted from Heliocentric Julian Date (HJD) of $2456912.35105 \pm 0.00015$ to BJD$_\mathrm{TDB}$ ** From the quoted R_p and R_s values; R_p was poorly constrained since the fitted b makes the transit grazing.

best fit transit model at the upper panel. The derived parameters from the emcee approach are shown on the corner plot, at the lower panel. A direct comparison of this work with the previously published parameters from Hellier et al. (2017) is in Table 5.3. We pinpoint that our results do not match the previous investigation within 1σ. We report a later mid-time point of 1.2 minutes, while the updated orbital parameters yield a more precise impact parameter value. Even though, the orbital parameters, i and a/R_s, are not in agreement either with the previous results, the uninterrupted TESS data, yielded a better acquisition of those measurements. The high-cadence datasets provided better constrained and more precise i and a/R_s values, which in turn yielded a more precise b for this system of 0.85. However, this newly derived determination of b is associated with a better determination of the transit depth, which now is greatly improved. Moreover, we report a refined measurement of a smaller planetary radius for WASP-140 b by approximately 12%. We also derived a better precision on the reported asymmetric radius uncertainty of WASP-140 b by approximately 86% and 67%. The uncertainty on the planetary radius has been greatly improved by this investigation and places the planet with conviction to a lower inflated radii regime with a smaller estimated temperature. However, the planet remains well beyond the cutoff temperature of 1000 K for the inflation to happen (Miller & Fortney 2011), and it continues to have an excess in its radius compatible with its temperature levels.

Exoplanets of grazing transits around moderately bright hosts are difficult to parameterize from the ground, as in the case of WASP-168 b in Hellier et al. (2019b). Nevertheless, in this work, using TESS, we improved significantly on the parameters of WASP-140 b, that now it is characterized as a less puffy and more dense exoplanet than it was thought to be.

5.6.2 WASP-136 b

Previous studies on WASP-136 b, have shown that this exoplanet belongs to an interesting category of planets, as a short-period hot Jupiter that orbits a sub-giant star. The limited candidates of this population might be attributed to tidal disruption that causes planets to spiral inwards and to the star (Lam et al. 2017).

WASP-136 b completes a full orbit around its evolved late-F host star ($V_{mag} = 9.93$) in 5.22 days and, with a radius of $R_{\mathrm{p}} = 1.38 \pm 0.16\,\mathrm{R_J}$ and mass of $M_{\mathrm{p}} = 1.51 \pm 0.08\,\mathrm{M_J}$, it is an inflated giant planet, which is half as dense as Jupiter. Intriguingly, WASP-136 is at its final main sequence phase and the derived planetary radius in the work of Lam et al. (2017) found to be 25% larger than expected in the models of Fortney et al. (2007). One plausible explanation is that the star moves towards the sub-giant branch and the intensity from the irradiation on the planet is expected to increase dramatically, the planet can heat up, through the stellar irradiation trapped in the interior of the planet, and trigger another re-inflation. A precise radius estimation might provide further clarifications on what the current status of this exoplanet's radius extension is.

We made use of six full transits of WASP-136 b, from the publicly available TESS 2-minutes cadence data in order to update/confirm the previous findings from the discovery paper (Lam et al. 2017), where one full and two partial transits were analyzed. We did not take into consideration the last transit light curve of sector 42, due to a starspot crossing throughout the transit chord that would lead to a biased measurement of the transit depth.

The final modeled light curve with the associated residuals are presented at the upper panel in Fig. 9.2, while the best fit parameters are shown in the corner plot at the lower panel. A comparison of the findings in this work with the previous complete study of Lam et al. (2017) is presented in Table 5.4. The derived $R_{\mathrm{p}}/R_{\mathrm{s}}$ varies significantly from the previous reported value by more than 3σ, indicating deeper transit light curves and larger planetary radius. However, the derived planetary radius is in agreement with the previously reported value, overall. We find an additional difference of 9% in the radius measurement between the two investigations, that makes it a total of 34% larger than expected in Fortney et al. (2007). The uncertainty on the planetary radius of this exoplanet has only been improved marginally with the analysis of the TESS data. We conclude to a larger planetary radius that yields a slightly more inflated and less dense exoplanet, that is consistent with the previous work of Lam et al. (2017).

5.6.3 WASP-113 b

WASP-113 b is a hot Jupiter that orbits a G1 type host star in a period of about 4.5 days. In the work of Barros et al. (2016), it is shown that the planet has a mass of $M_{\mathrm{p}} = 0.48\,\mathrm{M_J}$ and an inflated radius of $R_{\mathrm{p}} = 1.41\,\mathrm{R_J}$, hence a density of about $\rho_{\mathrm{p}} = 0.172\,\rho_{\mathrm{J}}$. However, the planetary radius was expected about 2σ smaller in the work of Fortney et al. (2007), assuming a coreless model. In our work, using TESS, we can confirm/refine the radius measurement of WASP-113 b, and investigate if we can improve on its radius uncertainty.

For this purpose, we analyzed a total of eight transit events (one partial transit was rejected), as they were observed with TESS during sectors 23 and 24. The

Table 5.4: Physical properties of WASP-136 b derived in this work with TESS data, in comparison to the previously published work of Lam et al. (2017).

Parameters [units]	This work Values ±1σ	Lam et al. (2017) Values ±1σ
T_c [BJD$_{\rm TDB}$]	2456776.9055 ± 0.0011	2456776.90615 ± 0.0011
i [°]	87.7 ± 1.2	$84.7^{+1.6}_{-1.3}$
a/R_s	7.4 ± 0.3	6.43 ± 0.65
R_p/R_s	0.0680 ± 0.0005	0.0641 ± 0.0012
b	0.30 ± 0.16	$0.59^{+0.08}_{-0.14}$
R_p [R$_J$]	1.50 ± 0.15	1.38 ± 0.16
ρ_p [ρ$_J$]	0.44 ± 0.14	$0.58^{+0.23}_{-0.15}$
$\log g_p$ [cgs]	3.29 ± 0.05	3.26 ± 0.09
T_{eq} [K]	1630 ± 40	1742 ± 82
H [km]	310 ± 40	-

best-fit model is shown on the upper panel in Fig. 9.3, while the best fit parameters are depicted on the corner plot at the lower panel, along with the values of the detrending coefficients. In Table 5.5, we present the comparison of the newly derived parameters with the previous work of Barros et al. (2016). The radius measurement is in agreement between the two independent investigations, along with the rest of the parameters that were confirmed now with independent datasets provided by TESS. Even though, the TESS data analysis improved only marginally the orbital parameters of this system, however it confirmed an exoplanet of a largely extended atmosphere ($H > 1000$ km) that orbits a bright host star, i.e., an excellent target for transmission spectroscopy investigations. This is one of the cases where ground-based observations and space-based ones, came into a complete agreement, highlighting this way the good function of the ground- and space-synergy.

5.6.4 WASP-120 b

WASP-120 b was discovered and characterized with the work of Turner et al. (2016). Five ground-based transit observations were used to determine the system's parameters, which yielded a massive exoplanet of $M_p = 4.85\,\mathrm{M_J}$ and an inflated radius of $R_p = 1.73\,\mathrm{R_J}$. The eccentricity of WASP-120 b is significant and equal to $e = 0.059 \pm 0.02$. Moreover, this exoplanet has an orbital period of 3.6 days, around its F5 type host. The host star is bright with $V_{mag} = 11$, an age of 0.7 Gyr and rather important activity (Turner et al. 2016). This activity was pinpointed due to an observed difference, of $1.2 \pm 0.4 \times 10^{-3}$, between the transit depths of two light curves. Another explanation for this difference could be the presence of a nearby companion. Interestingly, in the work of Bohn et al. (2020), there are hints that the host star belongs to a hierarchical triple system.

TESS revisited this system with four observing sectors. In our work, we employed 24 transit light curves of WASP-120 b, in total. We analyzed the TESS data as for the previous targets of our sample, and we kept the significant eccentricity of this planet as a fixed parameter during the transit light curve fit process. Our results

Table 5.5: Physical properties of WASP-113 b derived in this work from TESS data, in comparison to the previously published work of Barros et al. (2016).

	This work	Barros et al. (2016)
Parameters [units]	Values $\pm 1\sigma$	Values $\pm 1\sigma$
T_c [$\mathrm{BJD_{TDB}}$]	$2457197.09751 \pm 0.00045$	$2457197.098226^{*} \pm 0.000040$
i [°]	$86.9^{+1.4}_{-1.0}$	$86.46^{+1.2}_{-0.64}$
a/R_s	$8.2^{+0.6}_{-0.5}$	7.87 ± 0.59
$R_\mathrm{p}/R_\mathrm{s}$	$0.0917^{+0.0014}_{-0.0013}$	0.0899 ± 0.0015
b	0.45 ± 0.20	$0.486^{+0.063}_{-0.14}$
R_p [$\mathrm{R_J}$]	1.47 ± 0.11	$1.409^{+0.095}_{-0.14}$
ρ_p [ρ_J]	0.15 ± 0.04	$0.172^{+0.055}_{-0.034}$
$\log g_\mathrm{p}$ [cgs]	2.73 ± 0.08	$2.744^{+0.081}_{-0.072}$
T_eq [K]	1460 ± 70	1496 ± 60
H [km]	1030 ± 230	-

* Converted from HJD of $2457197.097459 \pm 0.00004$ to $\mathrm{BJD_{TDB}}$

have shown a smaller planetary radius of $R_\mathrm{p} = 1.39 \pm 0.08\,\mathrm{R_J}$ for WASP-120 b, in agreement with the previously published value at 1σ. Also, we report an earlier mid-time transit point by 2.3 minutes, and considering that WASP-120 b is the heaviest exoplanet of our sample, this might be an evidence that transit timing variations (TTVs) effects take place in this system. The large mass of the planet and the low metallicity of the host star indicate that the planet received a large portion of radiation from its host in order to puff-up and extend its radius. However, WASP-120 was reported to obtain significant activity in Turner et al. (2016) or, possibly, a companion star. The reported difference between two transit depths of independent observations is confirmed in our work with the analysis of the TESS datasets. More precisely, we fit the 24 light curves individually, with the same emcee process which is based on a MCMC approach, as for the rest of our targets, and obtained the fit transit depths for each of the 24 transit light curves of WASP-120 b. The largest transit depth difference occurs between the transits at the mid-time points of 2458426.172325 $\mathrm{BJD_{TDB}}$ and 2458447.839933 $\mathrm{BJD_{TDB}}$, at the observations of sector 4 and sector 5, respectively, and it is approximately $1.1 \pm 0.5 \times 10^{-3}$. We demonstrated that this difference between transit events is repeated and can be attributed to the stellar activity, in agreement with the previous investigation by Turner et al. (2016). Moreover, we can exclude significant contamination of the datasets due to a companion star by examining the crowding metric, "CROWDSAP", for all the observing sectors. This metric indicates that on average, for all the four sectors of this observation, only 4% of the received light has been obtained from nearby sources. By inspection of the TPF for this exoplanet from TESS, we observed that the companion falls in the detector's field-of-view, hence the SPOC team took this third light contamination into account in the derivation of the PDCSAP flux. This amount of contamination of 4% can be considered in practice negligible as the planet-to-star radius ratio would be underestimated only by 0.02%, hence the aforementioned transit depth difference might be attributed to the host activity and not to the presence of the nearby companion.

Table 5.6: Physical properties of WASP-120 b derived in this work with TESS data, in comparison to the previously published work of Turner et al. (2016).

Parameters[units]	This work Values $\pm 1\sigma$	Turner et al. (2016) Values $\pm 1\sigma$
T_c [BJD$_\mathrm{TDB}$]	2456779.4347 ± 0.0005	$2456779.4363^* \pm 0.0005$
i [°]	84.54 ± 0.35	82.54 ± 0.78
a/R_s	6.8 ± 0.2	5.90 ± 0.339
$R_\mathrm{p}/R_\mathrm{s}$	0.0751 ± 0.0005	$0.08093 \pm 0.00099^{**}$
b	0.65 ± 0.05	0.78 ± 0.02
R_p [R$_\mathrm{J}$]	1.39 ± 0.08	1.473 ± 0.096
ρ_p [ρ_J]	1.76 ± 0.32	$1.51^{+0.33}_{-0.26}$
$\log g_\mathrm{p}$ [cgs]	3.86 ± 0.03	3.707 ± 0.056
T_eq [K]	1749 ± 41	1880 ± 70
H [km]	90 ± 7	-

* Converted from HJD of $2456779.43556 \pm 0.00051$ to BJD$_\mathrm{TDB}$
** Computed from the given $(R_\mathrm{p}/R_\mathrm{s})^2 = 0.00655 \pm 0.00016$

Furthermore, with the analysis of the TESS data, we improved the precision of the orbital parameters of this system significantly. The i and a/R_s are not in agreement with the previous work of Turner et al. (2016), for more than 2σ. Our analysis yielded an updated impact parameter for this system that differs from the previous one for almost 3σ. The larger semi major axis, as derived from the fit, supports the presence of a smaller equilibrium temperature, that deviates from the literature value by approximately 3σ, which consequently yields a reduced atmospheric scale height equal to half its initial value. In Fig. 9.4, the final model fit is presented. The parameterization of the system after the emcee process and fit is shown on a corner plot at the lower part of the same figure, while a comparison with the work of Turner et al. (2016), is presented in Table 5.6. We conclude to a slightly smaller, denser and with a thin atmosphere of less than $H = 100$ km exoplanet.

5.6.5 WASP-93 b

WASP-93 b was discovered and characterized in the work of Hay et al. (2016). WASP-93 b has a mass of $M_\mathrm{p} = 1.47\,\mathrm{M_J}$ and it orbits a F4 star with period of about 2.73 days. Later on, in Gajdoš et al. (2019), the estimated radius of WASP-93 b was much smaller than the value published by Hay et al. (2016), $R_\mathrm{p} = 0.0873 \pm 0.0025\,\mathrm{R_s}$ and $R_\mathrm{p} = 0.1080 \pm 0.0059\,\mathrm{R_s}$, respectively. This inconsistency of more than 3σ regarding the planetary radii gave us additional motivation to revisit WASP-93 system and re-evaluate this transit depth measurement with TESS. Therefore, we made use of TESS light curves to compare the findings with this previous estimation, one of which is based on only one transit event (Gajdoš et al. 2019). We used TESS observations of sector 17 in order to revisit and refine the parameters of WASP-93 b. Grazing systems are hard to parameterize due to the fact that their transit light curves have rounded bottoms, constraining this way the information on the orbital parameters derived from a well-defined ingress and egress (when the planet starts to cross the projection of the stellar disk and when it exits). The planetary radii are sometimes poorly defined in grazing systems, but we expect TESS to provide insights on this domain.

For WASP-93 b, in total, there were employed six light curves, cleaned from outliers and detrended from systematics. We analyzed them similarly to our other targets of this investigation. In Fig. 9.5, we present the best-fit model on the folded light curves on the upper panel. In Hay et al. (2016), it is pinpointed that the mid-times are not well-defined due to uncertainties in the transit ephemeris. Hence, we used in our analysis the revised ephemeris in Gajdoš et al. (2019) ($T_\mathrm{c} = 2456079.553552 \pm 0.00457$ $\mathrm{BJD_{TDB}}$). We observed an offset in our transits' ingress of approximately 9.3 minutes later. The almost v-shaped transit gives indications of a background star that might contribute significantly to the received light curve. However, there are no companions with important brightness in the proximity in order to produce such effect, while another scenario could be that WASP-93 b belongs to a triple system (Hay et al. 2016). The final parameters of the system are shown at the corner plot in Fig. 9.5, while the comparison with the works of Hay et al. (2016) and Gajdoš et al. (2019) are presented in Table 5.7. The planetary radius of $R_\mathrm{p} = 1.54 \pm 0.06\,\mathrm{R_J}$ derived in our work is consistent with the work of Hay et al. (2016) of $R_\mathrm{p} = 1.597 \pm 0.077\,\mathrm{R_J}$, within 1σ. The derived parameters agree broadly with the published ones, while the transit depth and planetary radius are significantly different from in the work of Gajdoš et al. (2019) with $R_\mathrm{p}/R_\mathrm{s} = 0.0873 \pm 0.0025$ and $R_\mathrm{p} = 1.29 \pm 0.05\,\mathrm{R_J}$. This TESS investigation improved only marginally on the planetary radius uncertainty, it confirmed the findings in Hay et al. (2016) and solved a discrepancy between the two reported transit depths for WASP-93 b. Interestingly, the orbital parameters are consistent within 1σ, supporting a grazing exoplanet in all of these works, highlighting the need to parameterize grazing systems with caution. In a recent work published by Wong et al. (2021), the planetary radius and orbital parameters are in complete agreement with our work.

5.6.6 HAT-P-16 b

HAT-P-16 b is a transiting inflated hot Jupiter exoplanet that orbits a bright F8 dwarf ($V_{mag} = 10.8$) every 2.77 days on an eccentric orbit ($e = 0.036$). This is the second heaviest exoplanet of our sample. From previous investigations on this exoplanet (Buchhave et al. 2010), the planetary radius is estimated as $R_\mathrm{p} = 1.289 \pm 0.066\,\mathrm{R_J}$, its planetary mass as $M_\mathrm{p} = 4.193 \pm 0.094\,\mathrm{M_J}$ and its density $\rho_\mathrm{p} = 2.42 \pm 0.35$ g cm^{-3}.

Using seven light curves obtained with TESS, we revisited this system and defined its properties. We kept the eccentricity (as with the previously highly eccentric systems) fixed to the literature value during the transit light curve fit process. The best fit transit model is shown at the top panel of Fig. 9.6, and the associated best fit parameter corner plot on the lower panel of that same figure. At Table 5.8, we present the comparison of our work with the investigations by Buchhave et al. (2010) and Ciceri et al. (2013). With the analysis of the TESS datasets, we report a later transit by 15 minutes for HAT-P-16 b, an indication that probable TTVs are present. Since it is a massive exoplanet, TTVs are not unusual in this case. The derived orbital parameters are in a broad agreement with the works of Ciceri et al. (2013) and Buchhave et al. (2010), while the impact parameter is consistent within

Table 5.7: Physical properties of WASP-93 b derived in this work with TESS data, in comparison to the previously published works of Hay et al. (2016) and Gajdoš et al. (2019).

	This work	Hay et al. (2016)	Gajdoš et al. (2019)
Parameters [units]	Values $\pm 1\sigma$	Values $\pm 1\sigma$	
T_c [$\mathrm{BJD_{TDB}}$]	2456079.560 ± 0.0046	$2456079.5650^{*} \pm 0.0004$	$2456079.553552^{*} \pm 0.00457$
i [°]	81.55 ± 0.32	81.18 ± 0.29	82.27 ± 0.58
a/R_s	$6.11^{+0.18}_{-0.15}$	5.94 ± 0.13	6.45 ± 0.35
$R_\mathrm{p}/R_\mathrm{s}$	$0.1017^{+0.0028}_{-0.0020}$	$0.10474 \pm 0.00062^{**}$	0.0873 ± 0.0025
b	0.90 ± 0.04	0.904 ± 0.009	0.868 ± 0.080
R_p [$\mathrm{R_J}$]	1.54 ± 0.06	1.597 ± 0.077	$1.29 \pm 0.05^{***}$
ρ_p [ρ_J]	0.40 ± 0.09	0.360 ± 0.084	-
$\log g_\mathrm{p}$ [cgs]	3.17 ± 0.09	3.120 ± 0.093	-
T_eq [K]	1910 ± 40	1942 ± 38	-
H [km]	480 ± 110	-	-

* Converted to $\mathrm{BJD_{TDB}}$ from $2456079.56420 \pm 0.00045$ and $2456079.55280 \pm 0.00457$ HJD (Gajdoš et al. 2019).
** Computed from the given $(R_\mathrm{p}/R_\mathrm{s})^2 = 0.01097 \pm 0.00013$
***From the quoted R_p estimation in units of Earth radii provided in that work.

1σ with the work of Ciceri et al. (2013). The newly derived planetary radius is in better agreement with the work of Buchhave et al. (2010), within 1σ. Even though, with our TESS investigation we did not improve on the planetary radius uncertainty of this system, however we confirmed a planet with the same density and surface gravity as thought in Buchhave et al. (2010). In the future, TESS is not expected to observe HAT-P-16 b again.

5.6.7 WASP-123 b

WASP-123 b orbits a bright ($V_{mag} = 11.1$) G5 star, every 3 days. It is a hot Jupiter with an inflated radius of $R_\mathrm{p} = 1.32\ \mathrm{R_J}$. Considering the measurement of its mass of $M_\mathrm{p} = 0.9\,\mathrm{M_J}$, the planet has a density of about $\rho_\mathrm{p} = 0.4\,\rho_\mathrm{J}$ (Turner et al. 2016). It is a rather typical hot Jupiter and the revision of its planetary radius will contribute to the understanding of the general picture of this kind of exoplanets around evolved stars.

The analysis of the TESS datasets based on observations on this exoplanet from the sectors 13 and 27, interestingly, showed that there is a discrepancy regarding the derived transit depths. In sector 13, we derived an $R_\mathrm{p}/R_\mathrm{s} = 0.1240 \pm 0.0012$, while in sector 27, $R_\mathrm{p}/R_\mathrm{s} = 0.1054 \pm 0.0008$. To investigate this case, we made use of the "CROWDSAP" metric, that defines the ratio between the target flux and the total flux that falls on the photometric aperture. The PDCSAP fluxes are usually adjusted according to this crowding factor. For WASP-123 b observations at sector 13, the CROWDSAP metric is about 69.3%, while for sector 27, it is 89.8% and this indicates, for sector 13, a contamination due to third light of approximately 30%, while for sector 27, of about 10%. In Guerrero et al. (2021), it is pinpointed that "CROWDSAP" values of less than 0.8 yield an unreliable photometry. However, this metric can be sometimes underestimated by the PDC pipeline and can yield an

Table 5.8: Parameter refinement of HAT-P-16 b using high-cadence TESS data. The R_p value as derived from the analysis in our work is in better agreement with Buchhave et al. (2010) within 1σ significance.

	This work	Buchhave et al. (2010)	Ciceri et al. (2013)
Parameters [units]	Values $\pm 1\sigma$	Values $\pm 1\sigma$	Values $\pm 1\sigma$
T_c [BJD$_\mathrm{TDB}$]	$2455027.60356 \pm 0.00035$	$2455027.59293 \pm 0.00031$	$2455027.59281 \pm 0.00040$
i [°]	88.4 ± 1.0	86.6 ± 0.7	87.74 ± 0.59
a/R_s	7.73 ± 0.23	7.17 ± 0.28	7.67 ± 0.18*
$R_\mathrm{p}/R_\mathrm{s}$	0.1063 ± 0.0007	0.1071 ± 0.0014	0.1067 ± 0.0014
b	0.220 ± 0.130	$0.439^{+0.065}_{-0.098}$	0.30 ± 0.08*
R_p [R$_\mathrm{J}$]	1.31 ± 0.06	1.289 ± 0.066	$1.190 \pm 0.035 \pm 0.012$
ρ_p [ρ_J]	1.87 ± 0.25	1.95 ± 0.28**	2.33 ± 0.20
$\log g_\mathrm{p}$ [cgs]	3.804 ± 0.027	3.8 ± 0.04	3.87 ± 0.024
T_eq [K]	1566 ± 31	1626 ± 40	1567 ± 22
H [km]	93 ± 7	-	-

* Estimated from the given values for the angular separation of the system in AU and for the inclination in Ciceri et al. (2013). ** Converted to units of Jupiter's density from $\rho_\mathrm{p} = 2.42 \pm 0.35$ g cm^{-3} (Buchhave et al. 2010).

overestimated third light contamination, as in the work of Parviainen et al. (2021) for the exoplanet TOI-519 b. Sector 27 observations support an exoplanet much less contaminated from third sources than sector 13. Based on this, we expect the transits in sector 13 to yield a biased parameter refinement.

We checked the TOI-catalog [7], to investigate further this discrepancy and find the reason of its occurrence. As a public comment, it is mentioned that the transits of WASP-123 b affected the star with TIC31858844, for the entire sector observation. In the work of Bohn et al. (2020), the companion to WASP-123 has only a separation of 4.8″. It has a stellar mass of $0.4\,\mathrm{M}_\odot$ and effective temperature $T_\mathrm{eff} = 3524$ K. One scenario is that this is a highly active M2 dwarf that is blended in the photometry of its companion during the transiting event of WASP-123 b, hence the lower flux that was received in the photometric aperture from WASP-123. We neglected the transits of sector 13, since we cannot account for the missing light, and in our analysis we used only the data from sector 27, which contains transit observations with better target focused photometry. The TIC number of the stellar companion is registered in the TOI-catalog, indicating that the crowding factor is taken into account for the correction of the final PDCSAP light curve.

In total, we employed seven light curves for our analysis. The best model fit is shown at the upper left panel in Fig. 9.7 (while the best fit model from sector 13 investigation is presented on the right panel for comparison), and the final parameters are presented at the corner plot at the lower panel of the same figure. The comparison with the previous work of Turner et al. (2016) is shown in Table 5.9. Our TESS findings, other than a later transit midpoint by 2.3 minutes, are completely consistent with this previous work, even though they did not show any significant improvement on the uncertainty on the planetary radius of this exoplanet either.

---

[7] https://tev.mit.edu/data/

Table 5.9: Physical properties of WASP-123 b derived in this work with TESS data solely from Sector 27 (see in text), in comparison to the previously published work of Turner et al. (2016).

	This work	Turner et al. (2016)
Parameters[units]	Values $\pm 1\sigma$	Values $\pm 1\sigma$
$T_{\rm c}$ [BJD$_{\rm TDB}$]	2456845.1735 ± 0.0004	$2456845.171610 \pm 0.00039$ *
i [°]	86.2 ± 0.5	85.74 ± 0.55
$a/R_{\rm s}$	7.29 ± 0.20	7.13 ± 0.25
$R_{\rm p}/R_{\rm s}$	0.1053 ± 0.0007	0.10536 ± 0.00128 **
b	0.48 ± 0.06	0.530 ± 0.049
$R_{\rm p}$ [R$_{\rm J}$]	1.35 ± 0.05	1.318 ± 0.065
$\rho_{\rm p}$ [$\rho_{\rm J}$]	0.37 ± 0.05	0.393 ± 0.056
$\log g_{\rm p}$ [cgs]	3.063 ± 0.026	3.07 ± 0.04
$T_{\rm eq}$ [K]	1500 ± 40	1520 ± 50
H [km]	490 ± 40	–

* Converted to BJD$_{\rm TDB}$ from $2456845.17082 \pm 0.00039$ HJD in Turner et al. (2016).
** Computed from the given $(R_{\rm p}/R_{\rm s})^2 = 0.01110 \pm 0.00027$ in Turner et al. (2016).

5.6.8 WASP-76 b

WASP-76 b was discovered and characterized with the work of West et al. (2016). This exoplanet is an inflated hot Jupiter ($R_{\rm p} = 1.83\,{\rm R_J}$) that orbits its bright ($V_{mag} = 9.5$) F7 host in 1.8 days. In the recent work of Southworth et al. (2020), the authors wanted to account for the partial transits of the discovery paper that they were highly contaminated with red noise, and they proceeded with a refinement of this system using one full transit light curve of WASP-76 b obtained from CAHA 1.23m. The authors have discovered that the transit occurred 8.6 minutes earlier than predicted and the orbital period was 0.54s shorter than the expected value. Hence, it is suggested that TTVs might be responsible for this deviation. Moreover, they reported a larger radius ($R_{\rm p}/R_{\rm J} = 1.885^{+0.117}_{-0.042}$) and a higher equilibrium temperature ($T_{\rm eq} = 2235^{+56}_{-25}$ K) in comparison to the discovery paper.

During the previous years, numerous studies were conducted on this exoplanet, interestingly some of them using large ground-based telescopes such as the Very Large Telescope (VLT) (Ehrenreich et al. 2020) and/or space telescopes such as the Hubble Space Telescope (HST) (von Essen et al. 2020). Observations with TESS are currently available to contribute to the understanding of the WASP-76 b planetary system. For this purpose, we made use of TESS observations during sectors 30 and 42. In total, 23 light curves were employed in our analysis. Interestingly, we derived a new transit mid-time, as a free parameter from our MCMC analysis, using emcee, and it appears to occur approximately 14 minutes earlier than expected from West et al. (2016), while the orbital period is found to agree with Southworth et al. (2020) and be 0.47s shorter. We, therefore, confirm the need for a TTV analysis for this system. Moreover, even though our analysis did not improve on the planetary radius uncertainty of this exoplanet either, the high photometric quality of TESS yielded a planetary radius of $R_{\rm p} = 1.83 \pm 0.04\,{\rm R_J}$, which is in complete agreement with West et al. (2016). However, the analysis in order to derive the transit depth in West et al. (2016) neglects completely the contribution of WASP-76 A's companion. WASP-76 B has a $0.4438''$ separation, and it is 2.58 times fainter than WASP-76 A. The flux contrast between the two stars is approximately 10 (Ehrenreich et al. 2020). Using Eq. 5 in Ciardi et al. (2015), we applied a correction factor of $\sqrt{1.1}$ to our transit depth, which is compatible with the value of 1.4 that it is suggested in Ciardi et al. (2015), as a typical factor to apply, to account for the contamination of the third light when the planet transits the primary (instead of the secondary) star. This correction yielded a new $R_\mathrm{p}/R_\mathrm{s} = 0.111425 \pm 0.000094$, and moreover a new planetary radius of $R_\mathrm{p} = 1.92 \pm 0.04\,\mathrm{R_J}$, which is in complete agreement with the latest works on this subject (Ehrenreich et al. 2020; Southworth et al. 2020; von Essen et al. 2020). The corrected planetary radius yields also a new density estimation of $\rho_\mathrm{p} = 0.13 \pm 0.01\,\rho_\mathrm{J}$ (consequently more parameters are affected by this change in radius and density, and yield a $\log g_\mathrm{p} = 2.750 \pm 0.007$ cgs, and a $H = 1471 \pm 34$ km), which is in agreement with the previous within 2σ, and suggests now a less dense exoplanet. This TESS analysis confirmed the latest reports on this exoplanet, however it also provided a valuable precision in $R_\mathrm{p}/R_\mathrm{s}$, in comparison to all the other works, which is very useful for transmission spectroscopy investigations. Regarding the TESS light curve of this target, and the crowding metric being "CROWDSAP" = 0.99972, this signifies that only the 0.3% of this PDCSAP flux comes from contaminating sources. In this case, the analysis of the TESS light curves support the work of Ehrenreich et al. (2020) where they did not confirm the companion either, or, as they suggest, it is completely hiding behind WASP-76 A and does not contribute to the received photometry significantly. It is worthy noting that WASP-76 B is not registered with an allocated TIC number, which might be a reason why the SPOC team did not consider a dilution factor for this system. In Fig. 9.8, we present at the upper panel, the final fit of the TESS light curves along with the associated residuals, while at the lower panel, we present the derived values from the emcee process. We pinpoint here that our work is in a direct comparison to West et al. (2016), where the authors did not account for the third light contribution, since at the TESS datasets, the companion is not taken under consideration either, or its contribution is not significant, as it appears from the value of the crowding metric.

5.6.9 WASP-20 b

WASP-20 b was discovered and characterized in the work of Anderson et al. (2015). The binarity of this system (companion at $0.26''$) was analyzed in the work of Evans et al. (2016), where three scenarios were considered. WASP-20 b is an inflated, Saturn-mass planet. If we ignore the binarity of the system, the planetary radius and planetary mass are $R_\mathrm{p} = 1.20 \pm 0.14\,\mathrm{R_J}$ and $M_\mathrm{p} = 0.291 \pm 0.017\,\mathrm{M_J}$, if the planet transits the brighter star of this system then $R_\mathrm{p} = 1.28 \pm 0.15\,\mathrm{R_J}$ and $M_\mathrm{p} = 0.378 \pm 0.022\,\mathrm{M_J}$ and if the planet orbits the fainter star then $R_\mathrm{p} = 1.69 \pm 0.12\,\mathrm{R_J}$ and $M_\mathrm{p} = 1.30 \pm 0.19\,\mathrm{M_J}$. With TESS, we revisited this interesting system. Using two sectors of TESS observations and a total of ten light curves, we refined the planetary radius to $R_\mathrm{p} = 1.38 \pm 0.04\,\mathrm{R_J}$. Recently, Southworth et al. (2020) tried to determine the planetary radius of WASP-20 b with TESS observations of sector 2. They concluded to $R_\mathrm{p} = 1.382 \pm 0.057\,\mathrm{R_J}$ for a transit around the brighter star and $R_\mathrm{p} = 1.69 \pm 0.11\,\mathrm{R_J}$ for a transit around the fainter star. We used TESS observa-

Table 5.10: Physical properties of WASP-76 b, as derived in this work with TESS data, in comparison to the previously published work of West et al. (2016). In brackets, we present the derived values considering the third light contamination.

	This work - [L3 correction]	West et al. (2016)
Parameters[units]	Values $\pm 1\sigma$	Values $\pm 1\sigma$
T_c [BJD$_\mathrm{TDB}$]	$2456107.84623 \pm 0.00030$	$2456107.855819^{*} \pm 0.00034$
i [°]	$89.4^{+0.5}_{-0.6}$	$88.0^{+1.3}_{-1.6}$
a/R_s	4.1 ± 0.01	4.102 ± 0.062
$R_\mathrm{p}/R_\mathrm{s}$	0.10624 ± 0.00009 – $[0.111425 \pm 0.000094]$	$0.10630^{**} \pm 0.0035$
b	0.04 ± 0.05	$0.14^{+0.11}_{-0.09}$
R_p [R$_\mathrm{J}$]	1.83 ± 0.04 – $[1.92 \pm 0.04]$	$1.83^{+0.06}_{-0.04}$
ρ_p [ρ_J]	0.15 ± 0.01 – $[0.13 \pm 0.01]$	0.151 ± 0.010
$\log g_\mathrm{p}$ [cgs]	2.791 ± 0.007 – $[2.750 \pm 0.007]$	2.80 ± 0.02
T_eq [K]	2182 ± 35	2160 ± 40
H [km]	1335 ± 31 – $[1471 \pm 34]$	-

* Converted from $2456107.85507 \pm 0.00034$ HJD. **Estimated from the quoted R_p and R_s values in West et al. (2016).

tions of all the available sectors, sector 2 and sector 29, to eventually confirm those findings. The best fit model is shown in Fig. 9.9, at the upper panel therein, and the final parameterization appears on the corner plot at the lower panel. The comparison with the previous work that yielded a full parameterization of the system (Anderson et al. 2015) is presented in the Table 5.11.

In TESS observations the companion star is not identified with a TIC number, hence the "CROWDSAP" metric of, an average from both sectors, of 0.997, might not take into account the third light contribution from WASP-20 B. Therefore, to account for this contamination of 3%, we used the correction factor of 1.34, as in Southworth et al. (2020) for the analysis of the TESS data of sector 2. We adopted the stellar radius of the work of Southworth et al. (2020) of $R_\mathrm{s} = 1.242 \pm 0.044\,\mathrm{R}_\odot$ and with a derived $R_\mathrm{p}/R_\mathrm{s} = 0.1153 \pm 0.0005$, which agrees within 1σ with the previous work on TESS data, we concluded to a planetary radius of $R_\mathrm{p} = 1.43 \pm 0.05\mathrm{R}_\mathrm{J}$. This planetary radius is in good agreement with both previous works of Anderson et al. (2015) and Southworth et al. (2020). However, the stellar radii considered in those works are much different with $R_\mathrm{s} = 1.392 \pm 0.044\,\mathrm{R}_\odot$ and $R_\mathrm{s} = 1.242 \pm 0.044\,\mathrm{R}_\odot$ respectively. Taken into account the stellar radius derived in the ground based investigation instead, we concluded to a planetary radius of $R_\mathrm{p} = 1.6\,\mathrm{R}_\mathrm{J}$. This is another example of the necessity of the correct parameterization of the stellar parameters in order to obtain accurate planetary parameters. For this same system, furthermore, we report a later transit, by approximately 13.7 minutes, hence TTVs might be present, even though it is unlikely considering the small mass of the planet. The derived planetary radius is in agreement with Anderson et al. (2015), and also consistent with the "planet transits star A" scenario in Southworth et al. (2020). The planetary radius uncertainty is confirmed as well with the TESS independent space observations and the orbital parameters are verified too. Overall, TESS confirmed an inflated giant with many kms of atmospheric scale height, suitable for transmission spectroscopy investigations.

Table 5.11: Physical properties of WASP-20 b, as derived in this work with TESS data, in comparison to the previously published work of Anderson et al. (2015). The dataset is in rather complete agreement with the work of Southworth et al. (2020) (see in text). In brackets, we present the derived values considering the third light contamination of the companion star.

	This work - [L3 correction]	Anderson et al. (2015)
Parameters[units]	Values $\pm 1\sigma$	Values $\pm 1\sigma$
T_c [$\mathrm{BJD_{TDB}}$]	$2455715.66591 \pm 0.00034$	2455715.6564 ± 0.0003 *
i [°]	85.82 ± 0.16	85.56 ± 0.22
a/R_s	9.50 ± 0.17	9.29 ± 0.23
$R_\mathrm{p}/R_\mathrm{s}$	0.09963 ± 0.00047 - [0.1153 ± 0.0005]	0.10775 ± 0.00102**
b	0.691 ± 0.028	0.718 ± 0.018
R_p [$\mathrm{R_J}$]	1.38 ± 0.04 - [1.43 ± 0.05]	1.458 ± 0.057
ρ_p [ρ_J]	0.118 ± 0.012 - [0.108 ± 0.013]	$0.1006^{+0.0131}_{-0.0099}$
$\log g_\mathrm{p}$ [cgs]	2.585 ± 0.027 - [2.46 ± 0.03]	2.527 ± 0.036
T_eq [K]	1362 ± 26	1379 ± 32
H [km]	1340 ± 90 - [1790 ± 123]	-

* Converted from $2455715.65562 \pm 0.00028$ $\mathrm{BJD_{UTC}}$ ** Computed from the given $(R_\mathrm{p}/R_\mathrm{s})^2 = 0.01161 \pm 0.00022$ in Anderson et al. (2015).

5.6.10 WASP-108 b

WASP-108 b was discovered and characterized in the work of Anderson et al. (2014). The authors presented a bloated hot Jupiter of an inflated radius of $1.284 \pm 0.047\,\mathrm{R_J}$ which orbits a relatively bright ($V_{mag} = 11.2$) F9 star on a 2.68-days period. Recently, a companion star to WASP-108 was reported in the work of Bohn et al. (2020).

Even though, this previous work of Anderson et al. (2014) appears only in the archive, eventually this planet is confirmed with independent space observations with TESS. Observing sectors 11, 37 and 38, provided a total of 25 transit light curves to analyze. Interestingly, our MCMC process, based on the emcee implementation, yielded a difference in $R_\mathrm{p}/R_\mathrm{s}$ by more than 3σ. However, the crowding metric indicated that there was a correction of the received light curves for a contamination of approximately 13% by nearby sources, and this can be the main reason for the observed difference in the transit depth between our analysis and the previous work by Anderson et al. (2014). We report also a later transit mid-time by 5.6 minutes, while the orbital parameters are all in agreement with this previous investigation, within 1σ. However, the derived planetary radius is consequently larger, since the third light contamination is taken into account, and supports now a less dense exoplanet scenario for WASP-108 b. The modeled TESS light curve is shown on the upper panel of Fig. 9.10, while the derived parameters for this exoplanet are shown in the corner plot on the lower part of the figure. A direct comparison with the previously derived values of Anderson et al. (2014) is shown in Table 5.12.

Table 5.12: Physical properties of WASP-108 b, as derived in this work with TESS data, in comparison to the work of Anderson et al. (2014).

	This work	Anderson et al. (2014)
Parameters[units]	Values $\pm 1\sigma$	Values $\pm 1\sigma$
T_{c} [$\mathrm{BJD_{TDB}}$]	$2456413.79490 \pm 0.00018$	$2456413.79098 \pm 0.00015$ *
i [°]	89.2 ± 0.7	88.49 ± 0.84
a/R_{s}	7.03 ± 0.08	7.05 ± 0.13
$R_{\mathrm{p}}/R_{\mathrm{s}}$	0.11165 ± 0.00029	0.10867 ± 0.00069 **
b	0.10 ± 0.09	0.19 ± 0.10
R_{p} [$\mathrm{R_J}$]	1.35 ± 0.04	1.284 ± 0.047
ρ_{p} [ρ_{J}]	0.36 ± 0.04	0.422 ± 0.033
$\log g_{\mathrm{p}}$ [cgs]	3.040 ± 0.017	3.093 ± 0.023
T_{eq} [K]	1589 ± 33	1590 ± 36
H [km]	547 ± 26	-

* Converted from 2456413.79019 ± 0.00015 HJD ** Computed from the given $(R_{\mathrm{p}}/R_{\mathrm{s}})^2 = 0.01181 \pm 0.00015$ in Anderson et al. (2014).

5.7 Discussion

In the following paragraphs, we discuss the highlights of our analysis. More specifically, how the R_{p} (and the uncertainties on their measurements) derived from previous investigations and the measurements of R_{p} from our TESS analysis can be compared. Furthermore, we compare our newly derived b for these systems to the previously reported b values, and eventually we assess how these two quantities (R_{p} and b) are related. Better constrained b values, derived from a well acquired information on ingress and egress, place the planet in a more precise orbital configuration around its host. This consequently can yield a more robust R_{p} value, since the planetary radii are usually vulnerable towards the stellar limb darkening modeling process (Alexoudi et al. 2020).

5.7.1 Planetary radius refinement

For each one of the exoplanets of our sample, we derived their planetary radii through the analysis of TESS observations of single and multiple sectors. In Fig. 5.1, we present the derived planetary radii with their uncertainties. The radii measurements are located approximately on the line of equality for $R_{\mathrm{p}} = R_{\mathrm{p(TESS)}}$. However, for WASP-140 b there is a significant decrease in the planetary radius by 12% and its uncertainty is reduced by a factor of 3. This can be attributed to the fact that the transit analysis of the previously published work on this exoplanet concluded to a system with larger impact parameter value, hence a more grazing orbit. For the rest of exoplanets of the sample, the planetary radii agree within 1σ with the previous investigations. It is currently investigated by our group if TESS can improve to this extent the radii uncertainty of other exoplanets like WASP-140 b, regarding its grazing orbit around a host star of similar brightness. In our sample, WASP-93 b is similar to WASP-140 b in terms of a grazing orbit and similar host's apparent magnitude. However, for WASP-93 b, the radius uncertainty was confirmed by TESS, rather than improved. It is interesting to investigate if TESS can improve on the planetary radii and orbital parameters of similar systems to WASP-140 b, orbiting early K-type host stars. Interestingly, WASP-177 (Turner et al. 2019) is a K2 type host (V_{mag}=12.3) of a planet with a grazing orbit ($b = 0.98$) and will be observed with TESS during sectors 42 and 55. WASP-183 b (Turner et al. 2019), which belongs also to a grazing system ($b = 0.92$), orbits a slightly fainter star of G9/K0 type with V_{mag}=12.76 and will be observed by TESS during sectors 45 and 46. The photometric investigations of those two candidates might shed light whether there is a window in photometric observations where TESS in practice holds an advantage.

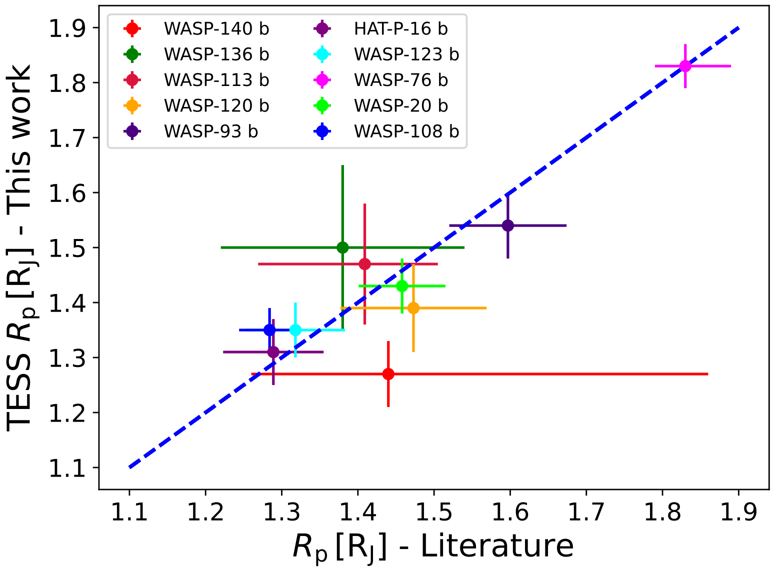

Figure 5.1: The new planetary radii as derived from TESS observations for each one of the exoplanets of our sample, in comparison to the previously published planetary radii values. The uncertainties on the radii are mostly the same within 1σ. The exception is the uncertainty on the radius of WASP-140 b, which has been greatly improved by TESS.

5.7.2 Impact Parameter refinement

The analysis of the TESS datasets has shown that for some cases the orbital parameter refinement also resulted in a different impact parameter estimation. In Fig. 5.2, we present the expected literature value for the impact parameter of each system and the derived TESS value. All the impact parameters derived with TESS are smaller (or equivalent) to the expected ones, likely due to the better continuous photometry provided by TESS. The ingress and egress of each system is monitored in high-quality data, and the orbital parameters i and a/R_s are better constrained. Overall, the TESS b values are in agreement with the previous investigations within 1σ. Except the cases of WASP-140 b, WASP-136 b, WASP-120 b and HAT-P-16 b. For these, i and a/R_s deviate between $1 - 2.5\sigma$ from the previous researches, and this yields a b for these systems that deviates also accordingly. For some systems of our sample, the eccentricity is not negligible. However, the non-zero eccentricity of WASP-140 b ($e = 0.047 \pm 0.004$), WASP-120 b ($e = 0.059 \pm 0.02$) and HAT-P-16 b ($e = 0.036 \pm 0.004$), is expected to play a minor role in the derivation of the impact parameters, based on Eq.7 from Winn et al. (2010).

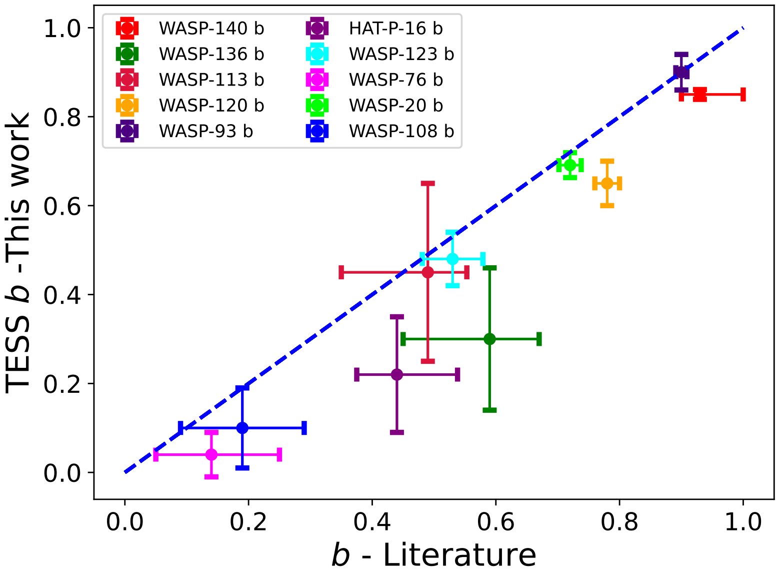

Figure 5.2: Here, we depict a comparison between the b values from the literature, and the b measurements as derived from the analysis of high-cadence TESS data. TESS confirmed b within 2σ significance for all the exoplanets of our sample, except for WASP-120 b. The new b measurement for this exoplanet varies by more than 2σ from the previous estimation, since the TESS analysis refined significantly ($> 2\sigma$) its orbital parameters of i and a/R_s.

5.7.3 The relations between the planetary radii and the impact parameters

The derived value of the radius of an exoplanet is strongly affected by the orbital set-up of the system. If the planet is transiting its host star centrally ($b = 0$) or over the limbs ($b = 1$), this plays a major role in the correct estimation of the transit depth (Alexoudi et al. 2020). As we saw previously, b depends on i and a/R_s. This information on the orbital parameters is usually acquired from a well-defined ingress and egress in the received light curve. For specific ground-based observations that the analysis is solely based on light curves from partial transits or really noisy datasets, this might yield poorly constrained orbital parameters. However, TESS with a 27-days uninterrupted photometry, confirmed b for most of the planets in our sample, while it also provided a better constrained b for the ones that their orbital parameters were refined within 2σ from the previous investigations.

In the upper panel, in Fig. 5.3, we present the previous investigations of the R_p and b measurements of these systems in fainter colors, while in vivid colors we depict the results as derived in this work using TESS. At the lower panel, it is noticeable that for systems of $b > 0.6$ the planetary radii have been overestimated by the previous investigations, while for centrally transiting systems the published radii were slightly underestimated. This is an indication that poorly constrained grazing systems likely yield an overestimation of planetary radii. However, our sample is small to verify this. The importance of this finding is currently under investigation by our team, using a rich sample of grazing systems observed with TESS.

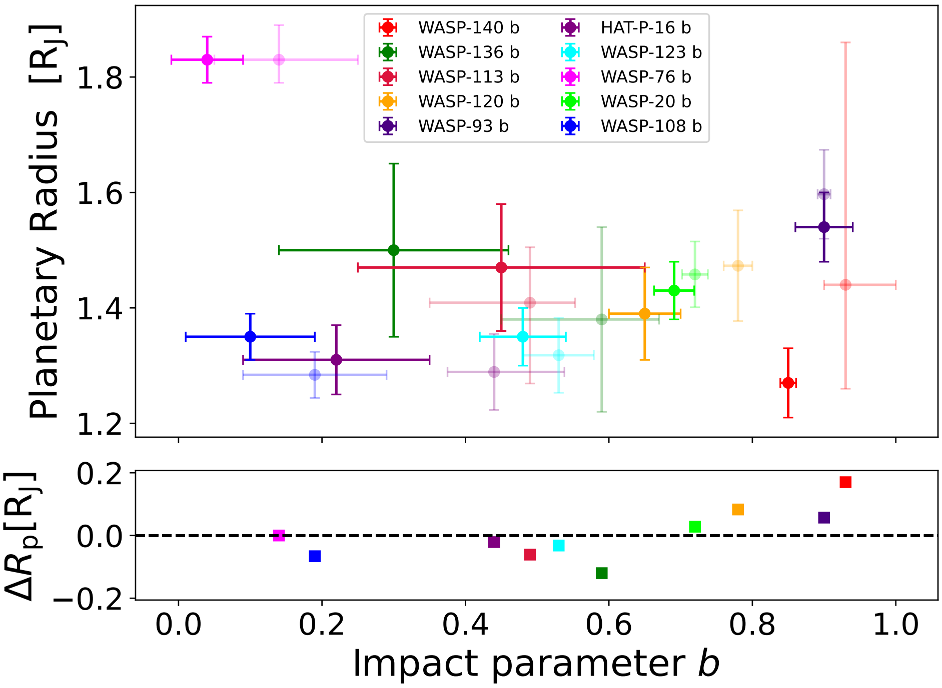

Figure 5.3: In the upper panel, we show the planetary radii derived in this work, in comparison to the impact parameter of these systems. In fainter colors, we present the literature measurements, while in vivid colors we depict the measurements as derived from the analysis of high-cadence TESS data. WASP-140 b, WASP-136 b, WASP-120 b and HAT-P-16 b are not in a complete agreement with the previous investigations. On the lower panel, we present the difference between the planetary radius reported in the literature and the planetary radius derived from TESS observations (colored squares). We plotted this difference versus the literature b value. For $b > 0.6$, the R_p values appear slightly overestimated by the ground-based investigations.

5.8 Summary and Conclusions

In this work, we employed a small sample of inflated hot giants and using high-quality uninterrupted datasets, provided by TESS, we aimed to improve on their planetary radius uncertainty. For this purpose, we chose exoplanets that have the largest reported uncertainty on their planetary radii, in the literature. The precise measurement of the planetary radius can help the evolutionary models to predict the presence or the absence of a planetary core and the interior energy of the planet (Bodenheimer et al. 2003).

First, we obtained the publicly available transit light curves from each system and then we fit those light curves using a detrending and a transit model. Through a MCMC approach, using emcee, we provided best fit values for each model that was applied on the light curves. Then we used these best fit values to derive the new planetary parameters for each system.

The results have shown that only WASP-140 b was benefited significantly from the TESS investigation with respect to its planetary radius uncertainty. Nevertheless, by using TESS's unprecedented precision, we were able to report the planetary radii refinement/confirmation of a sample of inflated hot giant exoplanets. The high precision of TESS not only yielded refined planetary parameters for WASP-140 b, it also improved the orbital parameters of WASP-120 b. For the latter, the large amount of continuous high-quality data, spread over four sectors of TESS observations, was the reason to derive better constrained orbital parameters for this system. Another outcome of our investigation is the clarification on the discrepancy regarding the planetary radius of WASP-93 b, between the independent investigations in Hay et al. (2016) and Gajdoš et al. (2019). For all the other exoplanets of our sample, the derived parameters are in agreement with the previous investigations (within $1 - 2\sigma$). Last but not least, we report an indication that the ground-based investigations likely have overestimated the R_{p} value for systems with $b > 0.6$. This needs to be confirmed with the analysis of high-quality TESS datasets of a rich sample of (near-)grazing systems.

For most of the cases, TESS confirmed the previous investigations demonstrating that excellent photometric studies can be achieved with small telescopes of the class of 1m (e.g. 1.2m STELLA[8] (Strassmeier et al. 2004, 2010) or the 1.23m CAHA[9]), that can reach photometric sensitivity of 1 mmag (e.g. Ciceri et al. (2013); Mallonn et al. (2015)) or even lower in some cases (Mallonn et al. 2021). However, the correct parameterization from the ground is sometimes vulnerable, due to the large point-to-point scatter of the data at the transit light curve, or due to incomplete transit datasets that lack the information on ingress and egress. For these investigations, TESS, with uninterrupted (exception is the data downloading time) and high-quality light curves, can contribute as a complementary tool to the ground-based investigations, in order to verify, or to refine the parameters of exoplanetary systems with independent measurements from space. Moreover, TESS observations could be combined with ground-based observations delivering high-fidelity datasets. One option is to try to combine TESS's precision with high-quality photometry from ground-based instruments in order to construct a transmission spectrum for atmospheric characterization (Yip et al. 2021). Eventually, future instrumentation (e.g. JWST (Gardner et al. 2006), PLATO (Rauer et al. 2014)) is expected to improve on the exoplanetary parameters tremendously. Till then, TESS will hold the fort by providing photometric data of the highest quality, available to the community for further researches and investigations on exoplanetary systems.

---

[8] stella.aip.de

[9] www.caha.es/CAHA/Telescopes/1.2m.htm

6 Comparative study of nearly-grazing and fully-grazing exoplanet system parameters derived with TESS and ground-based instruments

6.1 Abstract

Grazing transiting systems are rare and difficult to parameterize due to their partial transit geometry. We investigated a sample of 43 nearly-grazing to fully-grazing transiting exoplanetary systems, using datasets provided by the Transiting Exoplanet Satellite Survey (TESS), aiming first to refine major system parameters. We focus on the two parameters, impact parameter b and planetary radius R_{p}, through a comparison of TESS light curves with ground-based light curves. We investigate if there is a potential systematic trend between ground-based and space-based investigations that would possibly lead to a re-definition of the grazing nature of those exoplanetary systems. Our results have shown that the b value is confirmed for most of the systems within 2σ, and refined significantly for KELT-8 b, while the uncertainty on b was improved for five systems with $b > 0.8$. The R_{p} measurements of four systems were successfully refined, while the uncertainty of R_{p} was improved for the majority of exoplanets with $b > 0.9$. Furthermore, a systematic trend is more pronounced for systems with $b > 0.9$, where there is a mean overestimation on the ground-based derived R_{p} by $0.15 R_{\mathrm{J}}$. We concluded eventually that from our sample, only five systems are truly grazing, while four systems that were considered as grazing are not.

6.2 Introduction

The number of discovered exoplanets is constantly increasing and currently exceeds 5000 according to NASA Exoplanet Archive[1].

A very well-known method of detecting these exotic worlds is the transit method, where at the right orbital configuration, the planet is passing in front of its host star and blocks a fraction of the starlight (e.g., Haswell 2010). For an observer that follows the event, the received light curve has a dim in the brightness for the duration that the planet is in front of its host star. This depth during the transit event is equal to the planet-to-star surfaces ratio $\Delta F = (R_{\mathrm{p}}/R_{\mathrm{s}})^2$ (e.g., Seager &

---

[1] exoplanetarchive.ipac.caltech.edu

Mallén-Ornelas 2003), and can be used to correctly determine the planetary radius R_p with respect to the stellar radius R_s. This technique is extremely efficient on large gaseous exoplanets which belong to very close-in orbits and have the size of Jupiter. These type of exoplanets produce a larger dip in the received brightness on a light curve of about $1-2\%$. Moreover, there are four contact points to consider that describe the transiting planet event (e.g., Winn et al. 2010) and that shape the form of the light curve from an observer's point of view (see Figure 6.1). If the planet is transiting the star over the stellar equator (centrally), or over the limb, can be identified with a measurable quantity that is called the impact parameter b. This quantity depends on the semi-major axis of the system a usually estimated in units of stellar radii R_s, and the inclination i as: $b = \cos i \times a/R_\mathrm{s}$. A centrally transiting system has $b = 0$, while a transiting system over the outermost limb of the star has $b = 1$.

Interestingly, there are a handful of known exoplanets that transit their host star only partially, since not all of their planetary disc passes in front of the stellar disc. This type of exoplanets are in a grazing orbit and due to their special orbital trajectories the received light curves lack a distinguishable 2^nd and 3^rd contact points. Their V-shaped light curves compromise the correct determination of major physical parameters of the system, such as the planetary radius R_p and the impact parameter b. As we demonstrate in an example in Figure 6.2, the applied transit model differs tremendously from a well-defined transit model of a centrally transiting exoplanetary system. Consequently, the correct atmospheric characterization of the planet is at risk as well. The use of incorrect orbital parameters in a transit light curve fit can yield misplaced optical slopes and can affect strongly the transmission spectrum of the system (Alexoudi et al. 2018, 2020). Usually, those quantities have large uncertainties for grazing systems and the planetary radii are often overestimated (Hellier et al. 2012; Lillo-Box et al. 2015; Temple et al. 2018; Parviainen et al. 2019; Nielsen et al. 2020), hence the need for high-quality photometric datasets and much caution in order to derive precise parameters.

For planets of nearly-grazing to fully-grazing configurations, there are significant degeneracies between the transit parameters. Even though for non-grazing systems $R_\mathrm{p}/R_\mathrm{s}$ and b are not correlated, for grazing trajectories these parameters appear particularly correlated with each other. This degeneracy is studied in the works of Rowe et al. (2014) and Gilbert (2022), where the authors point the importance of this problem for systems with $b > 0.7$.

The uninterrupted and continuous observations of grazing systems facilitates identification of periodical modifications of the depth, duration and midtime of their transits which can be indicative of, e.g., additional bodies in the system that perturb the shape of the light curve, stellar pulsations, or polar-spot crossing events (Lillo-Box et al. 2015). These phenomena can all be detected with high-quality, high-cadence photometry.

Currently, from space, the Transiting Exoplanet Satellite Survey (TESS, Ricker et al. 2015) is a mission focused on bright stars and on more than 100 exoplanets. It provides, for more than four years, high-quality photometric datasets that in combination with ground-based photometric projects (e.g. The Hungarian Automated Telescope Network, HATNet project (Bakos 2018), The Wide Angle Search for Planets, SuperWASP project (Street et al. 2003)), and radial velocities (RV) studies (e.g., HARPS (Mayor et al. 2003), CARMENES (Quirrenbach et al. 2018),

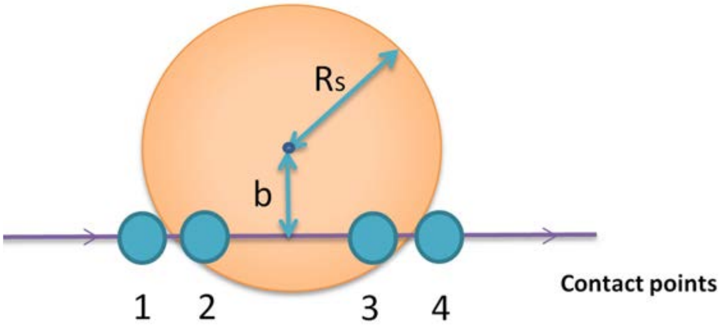

Figure 6.1: Schematic of the four contact points of a transiting event. The first contact point is when the planet's limb encounters the stellar limb (beginning of ingress), as seen from the observer's point of view. The second contact point is when the planetary disc appears to be entirely within the stellar disc (end of ingress). The third contact point is met when the planet's limb encounters again the stellar limb (beginning of egress) as it moves away towards the fourth contact point which is also the end of the transit (end of egress).

Reiners et al. (2010) Dumusque (2018)), contributes to the characterization of exoplanetary systems with precise measurements of their planetary radii and masses; eventually with precise measurements of their planetary densities.

In this work, we aim to ameliorate the uncertainties of those two major parameters of R_p and b using uninterrupted space data from TESS. Moreover, we investigate the hypothesis that ground-based observations are biased due to the grazing nature of those systems and always yield overestimated planetary radii. A trend of this scenario was observed in a small group of inflated giants with large b ($b > 0.6$) in Alexoudi (2022), while in the current work, we investigate a collection of well-known nearly-grazing to fully-grazing systems within a range of $0.6 < b < 1.0$, observed with ground-based instruments and TESS. Our work, in combination with recently published studies involving TESS data, compares directly to these ground-based investigations and provides a confirmation or a refinement of their two aforementioned parameters and a redefinition of the grazing nature of those systems.

In Section 6.3, we describe the TESS observations that we used in this work, while in Section 6.4 we show the analysis process that we employed. Section 6.5, follows with the presentation of our results and Section 6.6 contains the discussion and interpretation of them. In Section 6.7 we summarize our final conclusions.

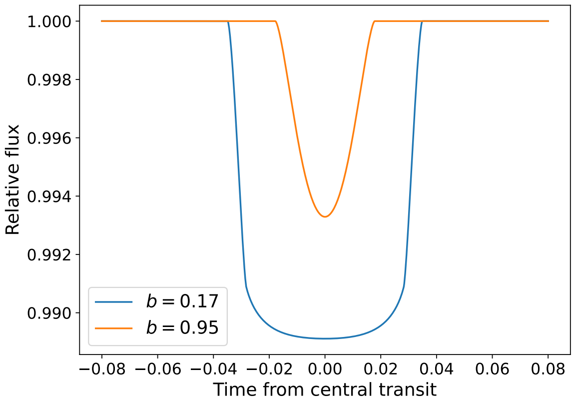

Figure 6.2: Transiting models generated with the BATMAN software for two systems with different orbital inclinations yielding different impact parameters (b values). Grazing systems (orange) exhibit a shorter, shallower and V-shaped transit light curves, than the centrally transiting systems (blue)

6.3 Observations

In this work, we employed a sample of 43 known giant exoplanets (Jupiter-like) orbiting stars with various brightness between 9.8 and 13.3 V_{mag}. These exoplanets allegedly have impact parameters at a range of $0.6 < b < 1.0$, being in a nearly-grazing or fully-grazing orbital configuration, as reported from ground-based observations. These systems were successfully observed by TESS, and we made use of observations that were made since the beginning of TESS' operation up to the end of 2021. The datasets consist of approximately 27-days of observations of each sector and a two-minute cadence. The TESS light curves were processed by the Science Processing Operations Center (SPOC) according to the work described in Jenkins et al. (2016). We used the Pre-search DATA Conditioning SAP Flux (PDCSAP_FLUX) for our transit model fit over the Simple Aperture Photometry Flux (SAP_FLUX), because it is a better quality product of the SPOC's pipeline (Tenenbaum & Jenkins 2018), as it is corrected for pointing and focus systematics, for outliers and third light contamination (Jenkins et al. 2016). We considered only high-quality datasets, which are publicly available at the Mikulski Archive for Space Telescopes (MAST) [2]. The observations of our sample made by TESS are presented in the Appendix (Tables 10.1 to 10.4), based on the information provided by the Web TESS Viewing Tool[3] (WTV). They are broken in 4 groups, A,B,C,D, each of which is described below. We note here that there are discovered systems with $b > 1.0$, mainly from Kepler and TESS observations. However, ground-based investigations are not reported for these, and therefore, lacking the comparison element, we did not include them in our work.

---

[2] https://archive.stsci.edu/

[3] heasarc.gsfc.nasa.gov/cgi-bin/tess/webtess/wtv.py

6.4 Data Analysis

We proceeded with the data analysis as presented previously in Alexoudi (2022). Here is a brief description of the process. We employed the `Lightkurve` package (Lightkurve Collaboration et al. 2018), which is a suitable software for TESS and Kepler datasets. Cadences with poor quality are excluded by using a conservative setting of the `Lightkurve` package to account for problematic pixels, contaminated by various effects (cf. Table 32 in Tenenbaum & Jenkins 2018). Each light curve is clipped to the 6σ level, and normalized by the median. We used a Savitzky-Golay filter with a window length of 1501 points and break tolerance of 50, which removes additional trends in the light curve. This method is favored in cases with large observational time gaps in the datasets. In addition, we applied a second order time-dependent polynomial to handle persistent trends in the light curves. We examined the Bayesian Information Criterion, BIC Schwarz (1978), from different detrending models and concluded that the second order time dependent polynomial minimizes the criterion value (cf. Mallonn et al. 2015, 2016). Finally, the TESS light curves for each target were folded to a common zero transit mid-time reference point.

The fit model is a combination of the detrending polynomial and the transit model. We employed the Bad-Ass Transit Model cAlculatioN (BATMAN, Kreidberg 2015) - a software developed for transit light curve modeling. To correct for the effects of the limb darkening, we used the quadratic law (cf. Howarth 2011). The limb darkening coefficients (LDCs) were derived using the calculator of the Exoplanet Characterization Toolkit[4]. This estimation of the LDCs was based on ATLAS stellar atmospheric model grids, which are suitable for TESS investigations (according to Claret 2017), and are calculated for the wavelength band at which the TESS detector is centered, corresponding to the Cousins I - band[5]. For the fitting model presented in this work we set, as initial parameter values, the ones published in the ground-based studies (see Table 6.1 for the publications references). We chose a uniform time frame for the mid-times of the selected transiting systems, i.e., the Barycentric Julian Date as the Barycentric Dynamical Time ($\mathrm{BJD_{TDB}}$) standard. This is generally recommended as more suitable for astrophysical events (Eastman et al. 2010) and complies with the TESS light curve's time format. Many of the time conversions were adopted directly from the ExoClock Project[6] (Kokori et al. 2021).

Prior to beginning our fit process, we kept all the parameters fixed to their theoretical/literature values – either calculated or referred in the ground-based publications. The mid-time of the transit T_0, the orbital inclination of the system i, the semi-major axis normalized in stellar radii a/R_s, the ratio of the planet-to-star radii $R_\mathrm{p}/R_\mathrm{s}$, and the three terms of the second order time dependent polynomial c_0, c_1 and c_2 are left free to vary during the fit.

We considered that the systems have circular orbits. For the systems with published eccentricity values, these were included in the model, but kept fixed during the model fit. Fixed parameter were kept also for the orbital period P and the LDCs. Furthermore, we used the maximum likelihood optimization in order to fit our data taking into account these free model parameters. For this purpose, we

---

[4] exoctk.stsci.edu/limb_darkening

[5] heasarc.gsfc.nasa.gov/docs/tess/the-tess-space-telescope.html

[6] https://www.exoclock.space/

made use of the "optimize" module of `SciPy` [7], which applies an optimization to the likelihood function and yields the most suitable parameters that maximize it. Then we used `emcee` [8] (Foreman-Mackey et al. 2013) in order to obtain the posterior distributions of the parameters, after the application of the combined transit model, with their respective errors. This algorithm can draw samples from uniform prior values for each parameter, aiming to define their posterior values. The combination of the prior function and the likelihood function yields the final probability function for each parameter. We initialized 30 walkers around the maximum likelihood estimations and performed 20000 `emcee` iterations. The "EnsembleSampler.get chain" method was used to access the chains. The walkers are expected to wander around the maximum likelihood value for each of the parameters, and then after a certain time, they start to converge to the posterior distribution. This time is calculated with the τ metric that measures the autocorrelation time needed by `emcee`. Chains longer than 50τ are considered well-converged. A burn-in phase is mandatory in order to clean the chains from the randomly acquired values prior to convergence of the chains. We used a burn-in phase of 10000 steps, which upon inspection was sufficient to cover all the different datasets of all the targets of our sample. Then, after thinning and flattening of each chain, we obtained a final list of samples for each model parameter. We adopted the median value of each parameter's posterior distribution as the best-fit value, while the 16^{th} and 84^{th} percentile intervals correspond to the $\pm 1\sigma$ uncertainties.

In Fig. 6.3 we present an example of the obtained TESS light curves for 3 sectors of observations of the exoplanet WASP-183 b. The transits were detrended, folded and fit as shown at the lower panel of the figure. The corner plot that shows the best fit values of the free model parameters is shown in Fig. 10.1. For a direct comparison with the ground-based work, we present in Fig. 6.4 the obtained light curves from the analysis in Turner et al. (2019) (see also Fig. 3 therein). The observations consisted of two transiting events of WASP-183 b, where a full and a partial transit light curves were acquired. We highlight how the model on the TESS data (this current work) supports a rather U-shaped transit, while the ground-based investigation shows a V-shaped.

6.5 Results

The parameter refinement/confirmation for R_{p}, $R_{\mathrm{p}}/R_{\mathrm{s}}$ and b measured for a rich sample of nearly-grazing to fully-grazing transiting exoplanetary systems is presented in the following Table 6.1. These references contain studies of ground-based and TESS observations, along with our, recently published work on the subject (Alexoudi 2022).

6.5.1 Impact parameter investigation

Exoplanets of Group A

Group A consists of exoplanets with impact parameter b between 0.6 and 0.7, as obtained from the publications in the literature (see Table 6.1). Using high quality

---

[8] emcee.readthedocs.io/en/stable/

datasets from TESS, we revisited those systems and focused on improving their b measurements. In the top left panel of Figure 6.5 we present the b values derived based on TESS observations (our work and literature) in comparison with the investigations derived from the ground (only literature). The results for this first group of exoplanets have shown that most of these systems' b measurement from TESS analyses (this work and literature), agrees within 1σ with those reported by ground-based observation studies (see upper-left panel in Figure 6.5 and Ground-based versus TESS in Table 6.1) in the literature. For the exoplanets XO-6 b, WASP-50 b, KELT-3 b and HATS-1 b, the newly derived b value is in agreement within 2σ from the ground-based investigations. Regarding WASP-43 b, in the work of Davoudi et al. (2021), the authors used a combination of ground-based data from the TÜBİTAK National Observatory of Turkey and TESS observations in order to provide a parameter refinement of this exoplanet, along with an investigation on its orbital decay. The authors report a 2.6σ decrease of b in comparison to results presented by Saha et al. (2021). The increased precision of the b uncertainties for the systems XO-6 b, WASP-72 b and KELT-3 b, which are improved by 70%, 60% and 35% − 48%, respectively, is notable. For WASP-100 b the uncertainty is improved significantly, i.e., in the range 75% − 88%, as reported with results presented in Jansen & Kipping (2020). Our study of XO-6 b is in agreement within 1σ with the work of Ridden-Harper et al. (2020).

Exoplanets of Group B

The exoplanets of the sample, which populates the Group B, are reported with an impact parameter $0.7 < b < 0.8$, as indicated in the literature of ground-based investigations. In this work, using TESS high-quality datasets, we derived anew these values and the results are depicted in the top right panel of Figure 6.5. For the majority of the systems, the b values are confirmed within 2σ of their ground-based investigations. However, there are two exceptions, i.e., the exoplanets WASP-120 b and KELT-8 b. The b measurement of WASP-120 b, reported in Alexoudi (2022), has a difference of 2.6σ with the previous ground-based investigation, while in our current work, KELT-8 b is found to differ by approximately 4σ from the ground-based investigation of Fulton et al. (2015). For KELT-8 b, we observed a large crowding metric provided by the header at TESS's target pixel file (TPF) of this specific observation, which shows that approximately 33% of the received light was contaminated by other sources in the field-of-view (FOV) and it had to be corrected. The contribution of this third light contamination is possibly the reason why there is so much difference between the orbital parameters derived from ground-based investigations and TESS. Moreover, the light curve itself exhibits strong rotation signals from the host star. In our analysis, we attempted to model the most prominent rotation signals and remove them from the light curve of KELT-8 b. We used the periodogram of the received light curve and identified the oscillations as peaks in the frequency domain. The highest peak corresponds to an estimate of the rotation period. We modeled the rotation signals in time domain using a Lomb-Scargle periodogram (VanderPlas 2018), which essentially fits a sinusoidal curve at the periodogram's frequencies and provides the power of each frequency. We removed signals that are defined by the 10 highest peaks from the time series, prior to fitting the transit and detrending models on this target's TESS light curve.

Exoplanets of Group C

Exoplanets of Group C, are considering those with impact parameter of $0.8 < b < 0.9$. With our analysis of TESS datasets of these systems, we found that all the exoplanets of Group C have b values that agree with the previous ground-based investigations (see Figure 6.5 - bottom left panel) within 1σ, with the exception of TrES-2 b where the b differs slightly above 1σ. The uncertainties on b were also improved significantly for KELT-14 b and HAT-P-30 b by 50% and 40%, respectively.

Exoplanets of Group D

Group D contains exoplanets with $0.9 < b < 1.0$. For this last group of exoplanets, the b value, as derived in this work using TESS high quality datasets, agrees within 1σ with the previous studies. Moreover, we provide significantly improved uncertainties of b for WASP-183 b, WASP-168 and WASP-177 b by 75%, 55% and 33%, respectively (Figure 6.5 - bottom right panel). The precision of the b value was improved significantly for WASP-140 b by 86% (on the positive uncertainty of b), as reported in Alexoudi (2022), while for WASP-174 b by 90% as reported in Mancini et al. (2020).

6.5.2 Planetary radius investigation

Exoplanets of Group A

The planetary radii of the exoplanets of Group A are confirmed with independent observations from space with TESS. In the upper-left panel, Figure 6.6, the hereby derived planetary radii are in the range of 1σ of the previous investigations. Whereas, the R_p measurements for the exoplanets WASP-43 b (Saha et al. 2021), and WASP-36 b (this work), agree overall within 2σ with their previous ground-based estimations. The uncertainty on the planetary radius is lower in the work of Davoudi et al. (2021) for WASP-43 b by approximately 98%, and for WASP-100 b by 31%−65%, in the work of Jansen & Kipping (2020). In the current work, we improved the positive uncertainty for HATS-1 b by approximately 40%. Moreover, our TESS investigation on X0-6 b is in complete agreement with the work of Ridden-Harper et al. (2020) within 1σ. We analyzed one more Sector of TESS observations (Sector 40), in addition to the datasets obtained from the previous three sectors that were reported in Ridden-Harper et al. (2020).

Exoplanets of Group B

The results of the planetary radii measurements of the second group of our nearly-grazing to fully-grazing systems sample, Group B, are shown in the upper-right panel of Figure 6.6. The planetary radii agree within 2σ with the previous investigations. Exceptions are the WASP-167 b with a difference of about 2.6σ and HATS-68 b with a difference of 2.1σ in comparison to the planetary radius reported from ground-based investigations.

Exoplanet	Ground based work				TESS			
	b	$R_\mathrm{p}/R_\mathrm{s}$	$R_\mathrm{p}\,(\mathrm{R_J})$	Reference	b	$R_\mathrm{p}/R_\mathrm{s}$	$R_\mathrm{p}\,(\mathrm{R_J})$	Reference
WASP-87A b	0.604 ± 0.028	0.08746 ± 0.00074	1.39 ± 0.06	Addison et al. (2016)	0.57 ± 0.05	0.0862 ± 0.0006	1.40 ± 0.05	this work
KELT-3 b	$0.61^{+0.04}_{-0.046}$	0.0939 ± 0.0011	$1.34^{+0.07}_{-0.072}$	Pepper et al. (2013)	0.671 ± 0.024	0.09477 ± 0.00035	1.39 ± 0.07	this work
WASP-92 b	$0.610^{+0.040}_{-0.043}$	0.1120 ± 0.0013	1.46 ± 0.077	Hay et al. (2016)	0.59 ± 0.07	0.1064 ± 0.0011	1.42 ± 0.06	this work
WASP-124 b	0.610 ± 0.020	0.1241 ± 0.0008	1.240 ± 0.03	Maxted et al. (2016)	0.67 ± 0.07	0.1265 ± 0.0014	1.284 ± 0.029	this work
HAT-P-50 b	$0.629^{+0.032}_{-0.041}$	0.0782 ± 0.0012	$1.29^{+0.06}_{-0.064}$	Hartman et al. (2015)	0.68 ± 0.06	0.0781 ± 0.0006	1.32 ± 0.06	this work
HATS-1 b	$0.633^{+0.020}_{-0.023}$	0.1288 ± 0.0020	$1.30^{+0.16}_{-0.098}$	Penev et al. (2013)	0.71 ± 0.04	0.1252 ± 0.0008	1.29 ± 0.09	this work
XO-6 b	0.633 ± 0.034	0.110 ± 0.006	2.07 ± 0.22	Crouzet et al. (2017)	0.70 ± 0.01	0.11471 ± 0.00027	2.20 ± 0.21	this work
WASP-100 b	$0.64^{+0.08}_{-0.16}$	0.08718 ± 0.00287	1.69 ± 0.29	Hellier et al. (2014)	0.537 ± 0.020	0.08683 ± 0.00037	$1.40^{+0.20}_{-0.1}$	Jansen & Kipping (2020)
QATAR-1 b	$0.645^{+0.010}_{-0.011}$	$0.14629^{+0.00063}_{-0.00064}$	$1.143^{+0.026}_{-0.025}$	Collins et al. (2017)	0.625 ± 0.021	0.1469 ± 0.0006	1.174 ± 0.024	this work
WASP-19 b	0.645 ± 0.012	0.14206 ± 0.00074	$1.38^{+0.05}_{-0.046}$	Lendl et al. (2013)	0.657 ± 0.025	0.1455 ± 0.0009	1.44 ± 0.05	this work
WASP-72 b	0.66 ± 0.12	0.0651 ± 0.0031	1.27 ± 0.2	Addison et al. (2018)	0.67 ± 0.05	0.0651 ± 0.0005	1.28 ± 0.16	this work
WASP-50 b	$0.669^{+0.018}_{-0.007}$	0.139 ± 0.0006	$1.17^{+0.04}_{-0.043}$	Chakrabarty & Sengupta (2019)	0.714 ± 0.019	0.1384 ± 0.0006	1.16 ± 0.04	this work
WASP-36 b	0.676 ± 0.016 [1]	0.13677 ± 0.00056	1.327 ± 0.019	Mancini et al. (2016)	0.693 ± 0.035	0.1311 ± 0.0009	1.285 ± 0.018	this work
WASP-43 b	0.681 ± 0.0058	$0.16214^{+0.00123}_{-0.00121}$	$1.09^{+0.06}_{-0.059}$	Saha et al. (2021)	0.660 ± 0.006	0.15805 ± 0.00035	1.0050 ± 0.0014	Davoudi et al. (2021)
WASP-170 b	0.689 ± 0.021	0.1175 ± 0.0041	$1.10^{+0.09}_{-0.085}$	Barkaoui et al. (2019)	0.67 ± 0.06	0.1216 ± 0.0013	1.14 ± 0.07	this work
XO-7 b	0.709 ± 0.023	0.09532 ± 0.00093	1.373 ± 0.026	Crouzet et al. (2020)	0.755 ± 0.021	0.0937 ± 0.0004	1.380 ± 0.020	this work
WASP-96 b	0.710 ± 0.019	0.11747 ± 0.00128	1.20 ± 0.06	Hellier et al. (2014)	0.71 ± 0.04	0.1177 ± 0.0011	1.23 ± 0.06	this work
WASP-98 b	0.710 ± 0.010	0.1603 ± 0.0008	1.10 ± 0.04	Hellier et al. (2014)	0.68 ± 0.04	0.161 ± 0.0014	1.190 ± 0.03	this work
WASP-20A b	0.718 ± 0.018	0.10789 ± 0.00107	1.462 ± 0.059	Anderson et al. (2015)	0.691 ± 0.028	0.1153 ± 0.0005	1.43 ± 0.05	Alexoudi (2022)
HATS-68 b	$0.736^{+0.014}_{-0.012}$	0.0725 ± 0.0016	$1.23^{+0.039}_{-0.029}$	Hartman et al. (2019)	0.79 ± 0.07	0.0762 ± 0.0009	1.326 ± 0.026	this work
WASP-101 b	0.736 ± 0.013	0.11225 ± 0.0009	1.41 ± 0.05	Hellier et al. (2014)	0.741 ± 0.017	0.10865 ± 0.00033	1.39 ± 0.04	this work
KELT-8 b	$0.741^{+0.027}_{-0.033}$	0.1145 ± 0.0026	$1.86^{+0.18}_{-0.16}$	Fulton et al. (2015)	0.56 ± 0.03	0.1086 ± 0.0004	1.80 ± 0.15	this work
WASP-49A b	0.745 ± 0.014	0.11730 ± 0.0016	1.115 ± 0.047	Lendl et al. (2012)	0.775 ± 0.023	0.1139 ± 0.0006	1.11 ± 0.04	this work
KPS-1 b	$0.75^{+0.04}_{-0.049}$	$0.1143^{+0.0037}_{-0.0034}$	$1.03^{+0.13}_{-0.12}$	Burdanov et al. (2018)	0.75 ± 0.06	0.1093 ± 0.0016	0.99 ± 0.10	this work
WASP-142 b	0.770 ± 0.02	0.09571 ± 0.00136	1.53 ± 0.08	Hellier et al. (2017)	0.77 ± 0.06	0.0967 ± 0.0013	1.58 ± 0.08	this work
WASP-167 b	0.770 ± 0.010	0.09055 ± 0.00055	1.58 ± 0.05	Temple et al. (2017)	0.766 ± 0.029	0.0988 ± 0.0006	1.76 ± 0.05	this work
WASP-31 b	0.780 ± 0.013	0.12708 ± 0.00106	1.55 ± 0.05	Anderson et al. (2011)	0.765 ± 0.027	0.1239 ± 0.0008	1.54 ± 0.04	this work
WASP-120 b	0.780 ± 0.02	0.08093 ± 0.00099	1.47 ± 0.096	Turner et al. (2016)	0.65 ± 0.05	0.0751 ± 0.0005	1.39 ± 0.08	Alexoudi (2022)
WASP-164 b	$0.822^{+0.008}_{-0.0091}$	0.1242 ± 0.0013	$1.13^{+0.04}_{-0.043}$	Lendl et al. (2019)	0.81 ± 0.07	0.1226 ± 0.0021	1.13 ± 0.04	this work
KELT-14 b	0.831 ± 0.02	$0.1143^{+0.0029}_{-0.0026}$	$1.52^{+0.12}_{-0.11}$	Rodriguez et al. (2016)	0.84 ± 0.01	0.11068 ± 0.00035	1.51 ± 0.09	this work
TrES-3 b	$0.832^{+0.004}_{-0.005}$	$0.16704^{+0.00261}_{-0.00177}$	1.51 ± 0.08	Saha et al. (2021)	0.846 ± 0.017	0.1648 ± 0.0023	1.33 ± 0.05	this work
WASP-192 b	0.840 ± 0.030	0.09623 ± 0.00317	1.23 ± 0.08	Hellier et al. (2019a)	0.77 ± 0.11	0.0945 ± 0.0018	1.24 ± 0.07	this work
TrES-2 b	0.854 ± 0.006	0.1253 ± 0.0010	1.22 ± 0.04	Torres et al. (2008)	0.835 ± 0.015	0.1236 ± 0.0006	1.23 ± 0.04	this work
HAT-P-30 b	$0.860^{+0.028}_{-0.027}$	$0.1109^{+0.0016}_{-0.0014}$	$1.469^{+0.039}_{-0.037}$	Maciejewski et al. (2016)	0.829 ± 0.017	0.1093 ± 0.0006	1.32 ± 0.06	this work
HAT-P-56 b	0.87 ± 0.01	0.10540 ± 0.00086	1.47 ± 0.04	Huang et al. (2015)	0.95 ± 0.04	0.1057 ± 0.0012	1.50 ± 0.04	this work
WASP-75 b	$0.882^{+0.006}_{-0.008}$	0.10344 ± 0.00145	1.27 ± 0.048	Gómez Maqueo Chew et al. (2013)	0.88 ± 0.05	0.1047 ± 0.002	1.31 ± 0.05	this work
WASP-34 b	$0.90^{+0.02}_{-0.01}$	0.11229 ± 0.00116	$1.22^{+0.11}_{-0.08}$	Smalley et al. (2011)	0.88 ± 0.03	0.1164 ± 0.0020	1.07 ± 0.10	this work
WASP-93 b	0.904 ± 0.009	0.10474 ± 0.00062	$1.60^{+0.08}_{-0.077}$	Hay et al. (2016)	0.90 ± 0.04	0.0751 ± 0.0005	1.54 ± 0.06	Alexoudi (2022)
WASP-183 b	$0.92^{+0.16}_{-0.09}$	0.15033 ± 0.01995	$1.5^{+0.9}_{-0.33}$	Turner et al. (2019)	0.82 ± 0.04	0.152 ± 0.004	1.33 ± 0.06	this work
WASP-140 b	$0.93^{+0.07}_{-0.03}$	$0.1656^{+0.0494}_{-0.0216}$ [2]	$1.4^{+0.4}_{-0.18}$	Hellier et al. (2017)	0.850 ± 0.011	0.1464 ± 0.001	1.27 ± 0.06	Alexoudi (2022)
WASP-174 b	0.940 ± 0.03	0.09434 ± 0.00159	1.3 ± 0.5	Temple et al. (2018)	$0.9530^{+0.0060}_{-0.0066}$	0.1098 ± 0.003	1.437 ± 0.050	Mancini et al. (2020)
WASP-168 b	$0.97^{+0.06}_{-0.04}$	$0.10909^{+0.00688}_{-0.0032}$	$1.5^{+0.5}_{-0.3}$	Hellier et al. (2019b)	0.904 ± 0.027	0.1163 ± 0.0027	1.30 ± 0.08	this work
WASP-177 b	$0.98^{+0.09}_{-0.06}$	$0.136015^{+0.01287}_{-0.00515}$	$1.58^{+0.66}_{-0.36}$	Turner et al. (2019)	0.91 ± 0.06	0.156 ± 0.016	1.25 ± 0.10	this work

Table 6.1: Comparison of the parameters b, $R_\mathrm{p}/R_\mathrm{s}$ and $R_\mathrm{p}(R_\mathrm{J})$ between ground-based (literature) and TESS (literature and our work) investigations, for each system. The sample consists of four groups according to their b value from the ground-based references, sorted in increasing order. Group A has $0.6 < b < 0.7$,Group B has $0.7 < b < 0.8$, Group C has $0.8 < b < 0.9$ and Group D has $0.9 < b < 1.0$.

---

[1] Calculated from the given values for a/R_s and i in the reference in comparison.

[2] From the quoted R_p and R_s values; R_p was poorly constrained since the fitted b makes the transit grazing.

Exoplanets of Group C

The radii of the exoplanets in Group C from the TESS investigation agree within 1σ with the ground-based works in comparison. For the exoplanets TrES-3 b and HAT-P-30 b, our investigation yielded a planetary radius refinement. The newly derived values differ from the literature by 2.9σ and 2.1σ, respectively.

Exoplanets of Group D

The planetary radii of the exoplanets which populate Group D agree within 1σ with the previous ground-based works. The uncertainties of the planetary radii values have been improved with the current TESS investigation, for the exoplanets WASP-183 b, WASP-168 b and WASP-177 b, by 93%, 84%, and 82%, respectively. For WASP-140 b and WASP-174 b, the uncertainties on R_p are improved significantly by 86% and 90%, in the works of Alexoudi (2022) and Mancini et al. (2020), respectively.

6.6 Discussion

We have acquired a sample of 43 nearly-grazing to fully-grazing exoplanets and revised two of their major physical properties, using TESS photometry based on recent literature works and our own. Sometimes, partial transits and noisy datasets acquired from ground-based instruments might result in poorly constrained orbital parameters and transit depth. TESS's uninterrupted 27-days of high quality photometry obtained from each observing sector, can be employed to settle this matter. The entire sample is presented in Table 6.1. We compare the findings of our work, and results derived in recent works with TESS data of a number of these systems, with previously conducted investigations based on ground-based observations. We were successful in confirming, or refining, the two major parameters affected by a grazing orbit, the impact parameter b and planetary radius R_p, through the planet-to-star radii ratio $R_\mathrm{p}/R_\mathrm{s}$ estimation. In the following, we discuss and examine the existence of a trend, previously mentioned in Alexoudi (2022), which hints to planetary radii measurements of systems with $b > 0.6$, obtained from ground-based investigations, being overestimated. In our work, we discuss, with a richer sample of gas giant exoplanets in nearly-grazing to fully-grazing configurations, the planetary radii differences between ground and space-based observations, specifically with TESS. In most of the cases, b and $R_\mathrm{p}/R_\mathrm{s}$ are confirmed within 2σ. In the end, we investigated how the TESS visits might have caused a redefinition of the grazing nature of these systems.

6.6.1 Comparison between planetary radii measurements from ground-based and TESS observations

In this section, we investigate the hypothesis that ground-based observations always yield overestimated measurements for the planetary radius in comparison to TESS (space) observations. There was a hint in the work of Alexoudi (2022), towards this assumption, where the author used a small sample of inflated hot Jupiters with various b values. In their work, for the systems with $b > 0.6$, they pointed at overestimation of the R_p measurement coming from the ground-based observations. In our work now, we test this hypothesis with 43 exoplanetary systems of $0.6 < b < 1.0$.

In Fig. 6.7, on the upper panel, we present the difference between the derived radii from the ground (literature) and from TESS (literature and this work) with respect to the impact parameter of the systems of our sample as derived with TESS observations (literature and this work). On the lower panel, in violin-shaped plots, we demonstrate how for each individual group the concentration of the planetary radii difference $\Delta R_{\rm p}$ accumulates around zero, except for the most grazing systems, where the scatter appears to be increased. For Group D, the median value of the difference on the radii, ascends to 0.15. Clearly, the sample is too small to draw conclusions for the most-grazing systems. However, in this work, we demonstrated that an ill fitted light curve from the ground would rather yield an overestimation of the planetary radius. This is largely based on a bias in the fitting process where the model fit unable to discern a second and third contact points, will try to maintain the transit depth intact. This degeneracy happens mainly due to the impact parameter, which, being a free parameter during the fitting process, will try to adjust the radius of the planet in order to maintain the true transit depth. Consequently, the errorbars of the fitted parameters will be large in order to account for the possible correct values for $R_{\rm p}$ and b. Therefore, the large errorbars from the ground contribute to this large mean value in the difference between Ground-based and TESS observations. With this work, we quantified this phenomenon and presented that it can be severe and up to $0.15 R_{\rm J}$ of radii difference for the most grazing systems. If we compare this overestimation with a typical standard error of the planetary radii derived with TESS observations of 0.04 $R_{\rm J}$, then it is indeed significant.

Regarding the four systems (HATS-68 b and WASP-167 b from Group B, and TrES-3 b and HAT-P-30 b from Group C) that yielded improved $R_{\rm p}$ with the TESS observations, we considered the biases introduced by the different wavelengths of observation as an explanation for the new measurements. TESS observations are centered at the red part of the spectrum, at 786.5 nm, therefore, the derived planetary radii would appear smaller in comparison to a system that was observed at the blue wavelengths from the ground and had an atmosphere. Using transmission spectrophotometry, one can identify Rayleigh scattering in the atmosphere of a planet that makes the apparent radius of the planet appear larger for the bluer wavelengths. We investigated this possibility for the planetary radii of the four systems that we refined in this work (WASP-167 b, HATS-68 b,TrES-3 b and HAT-P-30 b), and we confirmed that all the works in comparison from the literature, are conducted using observation at the red part of the spectrum. Exception is the system WASP-167 b because in the work of Temple et al. (2017), from the 18 light curves used in their analyses, the 5 light curves are obtained from observations at the bluer part of the spectrum. A Rayleigh dominated atmosphere would make the planet appear larger and the transit depth deeper for those wavelengths. However, no such an effect is observed, and our TESS investigation yielded an even larger $R_{\rm p}$ for this system. Similarly, for HATS-68 b, the TESS radius appears to be larger in comparison to the ground-based works of observations at the red wavelengths of the spectrum. For TrES-3 b and HAT-P-30 b, we find smaller planetary radii in comparison to their ground-based observations, that were all performed at comparable to TESS's wavelength bands. For this reason, we are confident that we refined the $R_{\rm p}$ measurements for those four planetary systems.

6.6.2 Grazing Nature

As a further step in order to understand the importance of the correct system parameterization, i.e. in the construction of evolutionary models of these systems, we assessed the grazing nature of the 43 systems investigated in this work. With the newly derived TESS parameters of b and R_p, the nearly-grazing to fully-grazing scenario can be in question. Truly grazing transits are met when only a part of the planet is transiting in front of its host star. According to the grazing criterion (Smalley et al. 2011), the impact parameter b and the planetary-to-star radii ratio $R_\mathrm{p}/R_\mathrm{s}$ need to fulfill the following condition, where:

$$b + \left(\frac{R_\mathrm{p}}{R_\mathrm{s}}\right) > 1, \tag{6.1}$$

in order to consider a system as truly grazing. Therefore, we discuss the updated redefinition of the true nature of the orbital configuration of the most grazing systems with TESS.

In Fig. 6.8, we present the grazing criterion estimation, as derived from the results in Table 6.1 in comparison to the impact parameter, of exoplanets of Group C and Group D. Essentially, we depict the grazing criterion versus b of those systems that are more likely to be affected by the new parameterization with TESS. The squares represent the grazing criterion estimations for systems that were parameterized using literature ground-based investigations, while the circles of the same color depict the parameters as derived with TESS (from the literature and this work). Evidently, the majority of the exoplanets in our sample belong to a non-grazing or nearly-grazing configuration (see also Fig. 10.2 for the grazing criterion re-defined for systems of Group A and Group B indicating non-grazing systems). However, with this work, the exoplanets TrES-3 b and HAT-P-56 b are considered now as grazing systems, since the grazing criterion exceeds unity for these two exoplanets. The exoplanets WASP-174 b, WASP-168 b and WASP-177 b of Group D, are confirmed as grazing systems, while, on the other hand, WASP-140 b and WASP-93 b (Alexoudi 2022), and WASP-183 b and WASP-34 b (this work), are no longer considered, according to this criterion, as grazing systems.

6.7 Summary and Conclusions

We used TESS observations to revisit 43 known exoplanetary transiting nearly-grazing to fully-grazing systems and estimated the major parameters, i.e., planetary radius and the impact parameter, which can be biased by their grazing nature. For most of the cases of nearly-grazing to fully-grazing exoplanetary systems, we found parameter estimations of their planetary radius and impact parameter that are consistent with the ground-based works in comparison, within error bars. We refined the impact parameters of KELT-8 b, and improved significantly the precision of the impact parameter uncertainty for the systems XO-6 b, WASP-72 b, KELT-3 b, KELT-14 b, HAT-P-30 b, WASP-183 b, WASP-168 b and WASP-177 b. We refined the planetary radii of WASP-167 b, HATS-68 b, TrES-3 b and HAT-P-30 b. And we estimated significantly more precise uncertainties on the planetary radii for the systems WASP-183 b,WASP-168 b and WASP-177 b.

Furthermore, we addressed the hypothesis that ground-based investigations likely yield overestimated planetary radii for systems with $b > 0.6$. However, in our work, this hypothesis is not confirmed for the majority of the systems in the sample, and only for the most grazing systems, of $b > 0.9$, there is a tension to have overestimated radii from the ground by 0.15 R_J.

Last, but not least, we re-assessed the grazing nature of those systems. We conclude mainly to non-grazing or nearly-grazing systems. The systems WASP-140 b and WASP-93 b (Alexoudi 2022), and WASP-183 b and WASP-34 b (this work) appear to not hold on to the grazing system definition anymore. While we promoted with our work, the systems TrES-3 b and HAT-P-56 b towards the truly-grazing systems regime. At the end, we confirmed the systems WASP-174 b, WASP-168 b and WASP-177 b as truly-grazing systems.

For most of the cases, with the independent observations from TESS, there was a confirmation of the impact parameters and planetary radii measurements of these systems. This is an excellent demonstration of how high fidelity photometric studies can be conducted with small sized telescopes of 1 m, e.g., 1.2 m STELLA[9] (Strassmeier et al. 2004, 2010), suitable to reach a photometric sensitivity of 1 mmag (cf. Mallonn et al. 2015) or even lower (cf. Mallonn et al. 2021).

Fully-grazing systems are indeed rare, and this short number can be attributed partially to the hypothesis regarding the existence of polar spots on the host star. In Oshagh et al. (2015), the authors highlight the plausibility that a grazing transit event might be wiped out totally by a polar spot. Even though nearly-grazing and grazing systems are difficult to characterize and estimate their major physical and orbital parameters, they are proven as the most useful tools when in search of third non-transiting bodies in a system. An example is GJ-436c, an exoplanet that was found due to unexpected perturbations of the orbital inclination of GJ-436b (Ribas et al. 2008). For a close-in transiting hot Jupiter exoplanet, under the presence of a third non-transiting planet in the system (Miralda-Escudé 2002), or an exomoon (Kipping 2009, 2010), one should expect impact parameter variations due to precessions of the periastron and line of nodes, which will affect the duration and the depth of the transit significantly (e.g., Davis et al. 2020). The sensitivity of the nearly-grazing or fully-grazing systems to small variations of their inclinations and duration of their transit duration during different epochs can be a powerful tool in order to discover all the components of an exoplanetary system. For systems with $b > 1.0$, different approaches should be used. A modeling solution is described in detail in Gilbert (2022) using umbrella sampling. Major advances in the characterization of grazing systems are expected to be done with future instrumentation such as PLATO (Rauer et al. 2014), which will provide unprecedentedly precise planetary radii for a large sample of systems.

---

[9] stella.aip.de

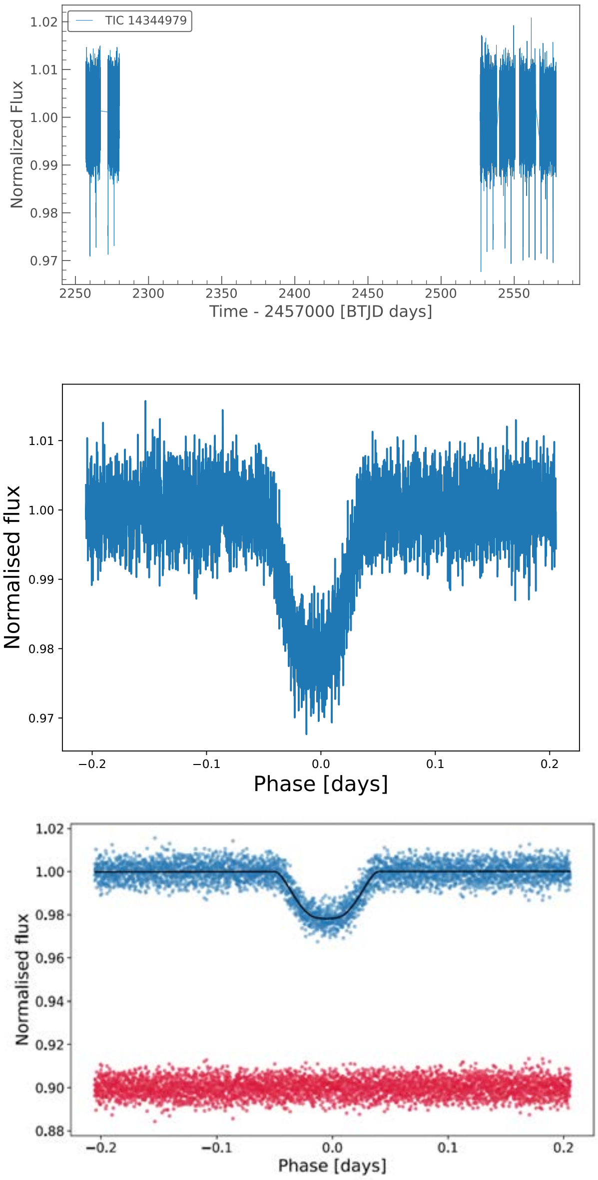

Figure 6.3: The obtained transit light curves from three observing sectors (35,45,46) with TESS of the exoplanet WASP-183 b or TIC 14344979 (*top panel*). The light curves were detrended and folded to a common transit mid-point (*middle panel*). The final transit model fit is shown on the *lower panel* (black solid line) along with the residuals (red dots) shifted on the y-axis for clarity.

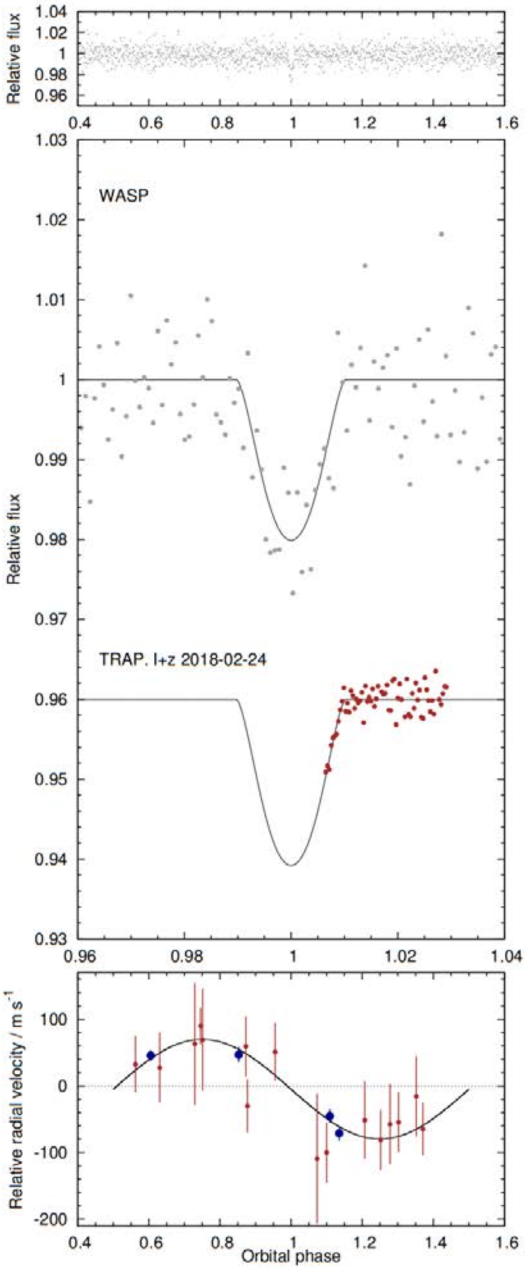

Figure 6.4: Adopted from Fig. 3 of Turner et al. (2019). The WASP-183 b discovery light curve phase-folded (*top panel*). The transit light curves used in joint analysis and overplotted with the transit model (*middle panel*). The radial velocities obtained with the CORALIE spectrograph, fitted with a model, are presented in the bottom panel.

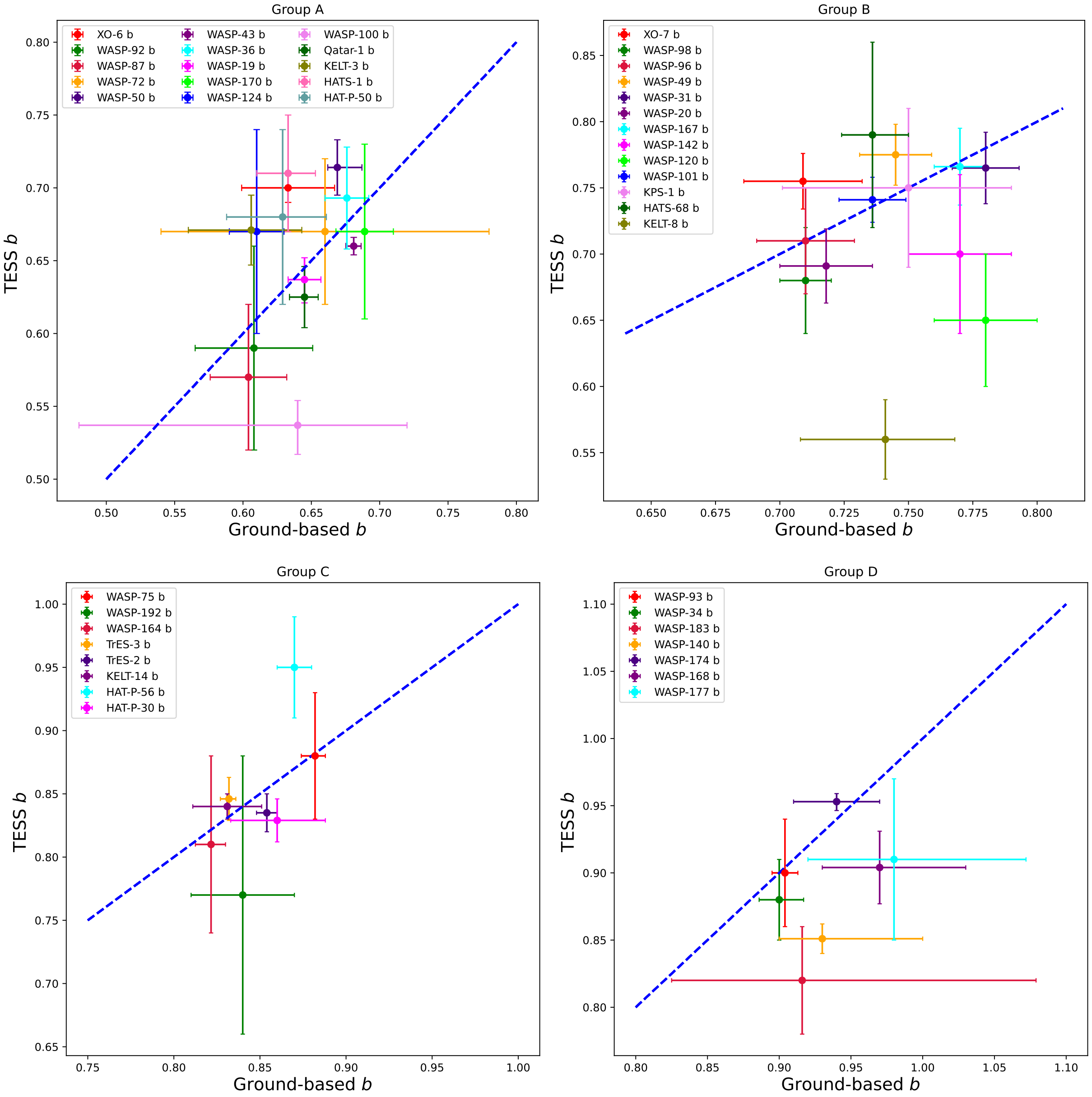

Figure 6.5: Comparison between the derived b values from TESS investigations (literature and this work), and the ground-based measurements from the literature. These are comparative plots for Group A (*top left*), Group B (*top right*), Group C (*bottom left*), and Group D (*bottom right*). The blue dashed line denotes an equality line.

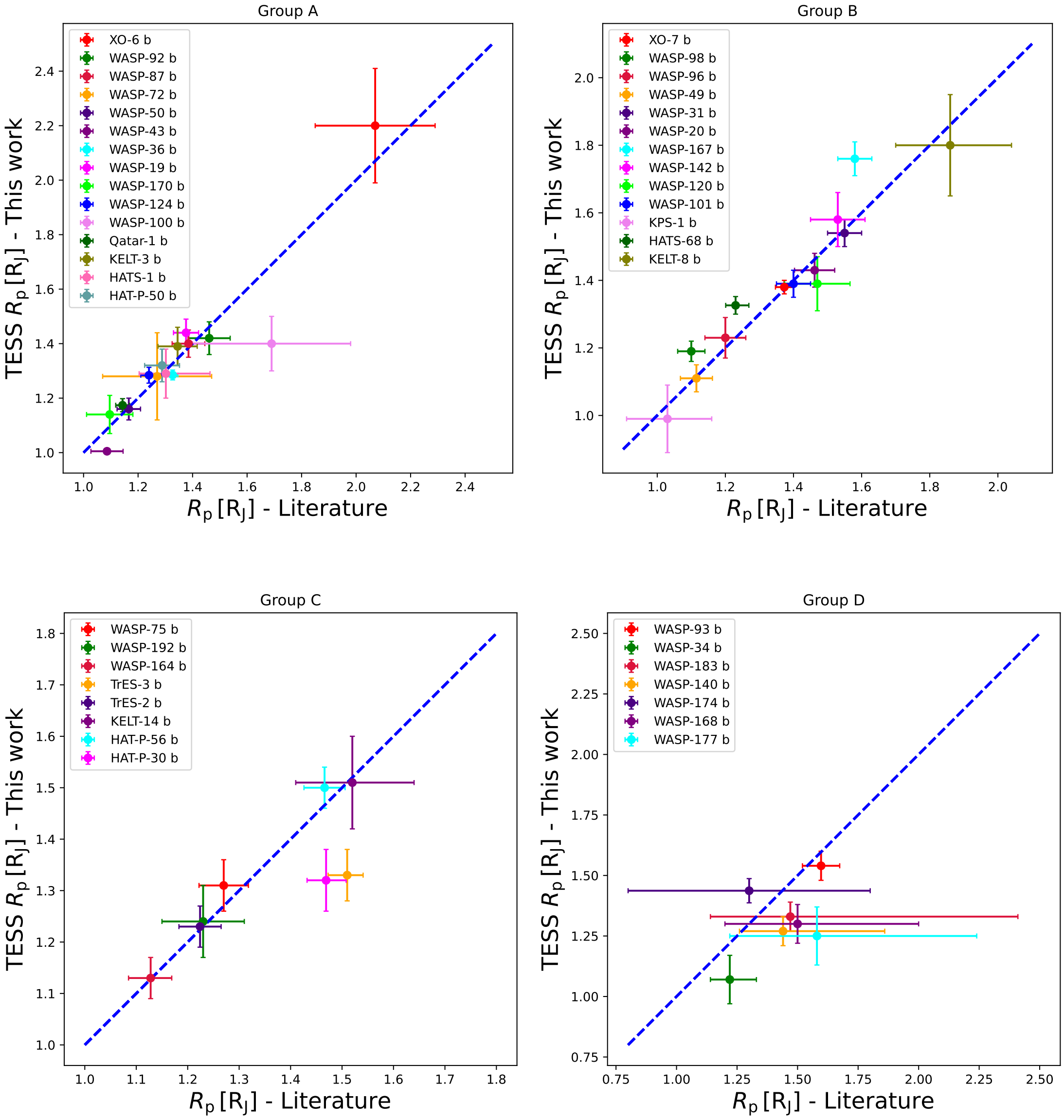

Figure 6.6: Planetary radii of the exoplanets of each group, as derived with TESS data (this work and literature), in comparison to a ground-based research from the literature, according to Table 6.1 references. In the upper left panel, we present the planetary radii comparison of the exoplanets of Group A. The upper right panel shows the comparison of the Group B planetary radii, while at the lower left panel is the comparison for Group C. Finally, at the lower right panel there is the comparison between the derived planetary radii from Group D. The blue dashed line denotes an equality line.

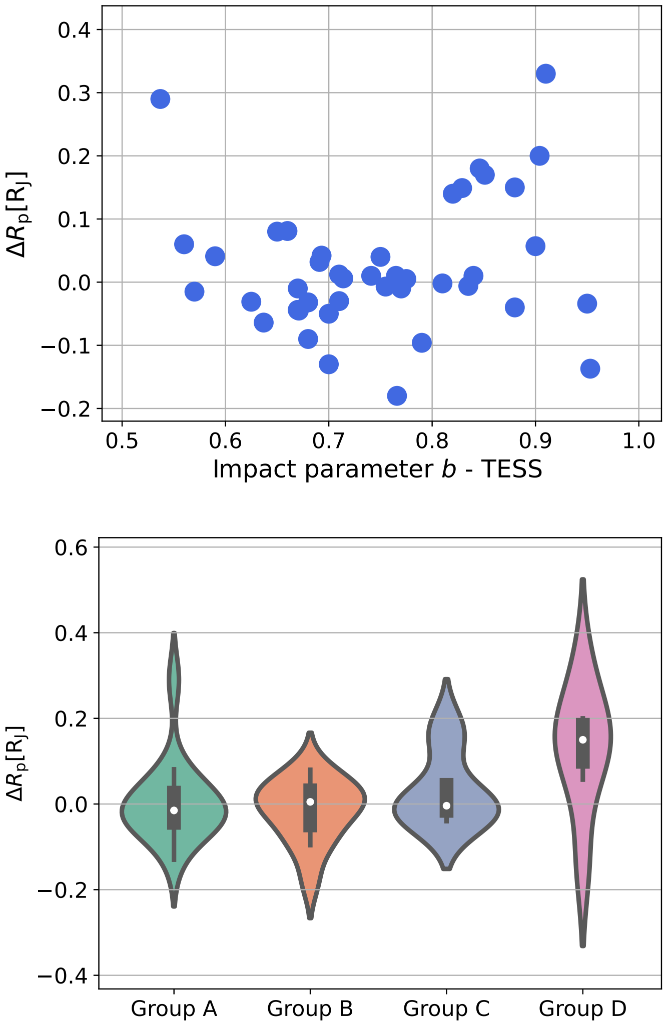

Figure 6.7: Top panel depicts the difference between the planetary radii measurements reported from ground-based investigations (from the literature) and TESS investigations (from the literature and newly derived in this work) plotted against the impact parameters derived from TESS observations (from the literature and newly derived in this work). The violin-shaped plots showing the distribution of the differences between ground-based and TESS derived radii for each group is shown in the bottom panel. The median values are approximately zero for systems with $b < 0.8$. On the other hand, towards most grazing systems ($b > 0.9$), we observe an excess and a tendency to have a median radius overestimation of 0.15 from the ground.

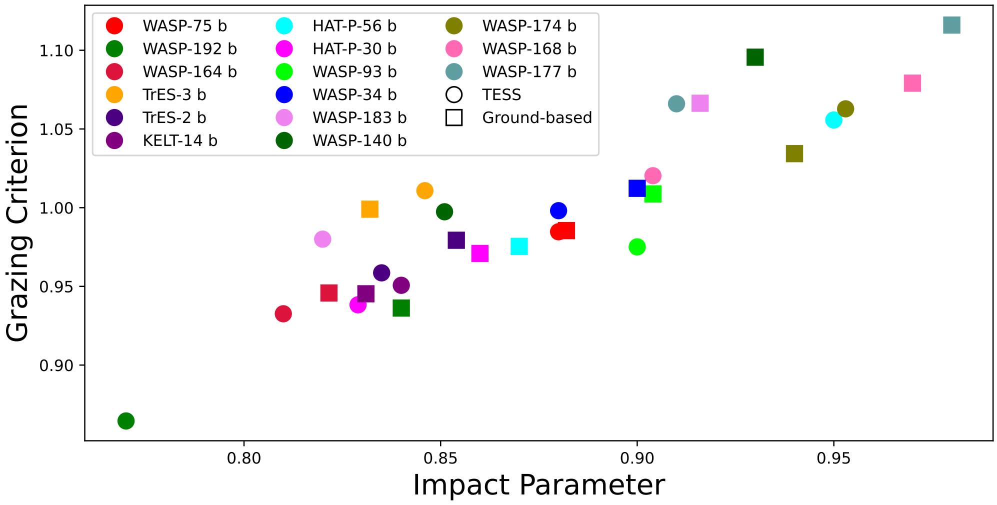

Figure 6.8: The estimated grazing criterion value with respect to the impact parameter measurements for the exoplanets of Group C and Group D, that are more likely to exhibit grazing criterion of 1. The values derived from ground-based investigations from the literature are represented by squares. The measurements derived based on TESS results from the literature and our own work are represented by circles in corresponding colors.

7 Discussion and conclusions

7.1 On the role of the impact parameter degeneracy

Transmission spectroscopy is currently one of the most powerful techniques for probing the atmospheres of exoplanets. However, sometimes, due to the faint transmission signals, stellar activity of the host star, or the contribution of the limb darkening effect, this technique can prove challenging, and it can yield inconsistencies regarding the atmospheric characterization of the same system. One way to investigate the source of these reported discrepancies is to consider the impact parameter degeneracy.

With synthetic transit light curves, simulating transiting events, at different wavelengths of observation, it is proved that the spectral slope changes based on the uncertainty of the employed orbital parameters; more specifically, that it changes with deviations from the true impact parameter measurement b. This degeneracy persists with different spectral types of hosts. For exoplanets orbiting K-type stars it is more likely to exhibit steeper optical slopes, while various features might appear at the blue wavelengths for exoplanets around M-type stars. Moreover, at the wavelengths where the limb darkening effect is stronger, there is a wavelength dependent offset. This produced slope tends to be steeper with larger b measurements. The variations in the adopted b value, introduce positive or negative slopes, creating an envelope of possibilities for the true transmission spectrum. For a typical b uncertainty, the amplitude of the spectral slope from blue to near-infrared wavelengths is of at least one atmospheric pressure scale height. This estimation is made for an inflated hot Jupiter with large scale height; a suitable target for transmission spectroscopy. Exoplanets with smaller scale heights, hence weaker transmission signals, may experience a stronger impact parameter degeneracy of higher values in units of scale height. Therefore, the precision in defining b is crucial for a correct atmospheric characterization.

The impact parameter degeneracy can sometimes explain discrepancies of atmospheric characterization of individual targets. In numerous works in the literature, the authors proceeded with their investigations only after considering this effect described in Alexoudi et al. (2018), and after a complete, extended, and thorough analysis in Alexoudi et al. (2020) (and Chapter 4 in this dissertation). In Todorov et al. (2019), in order to construct the transmission spectrum for the exoplanet HAT-P-1 b, a fixed inclination value was employed in the transit light curve fit, only after being certain that it is of extreme precision. In von Essen et al. (2020), regarding HST/STIS observations of WASP-76 b, the authors kept fixed orbital parameters to their values from the literature using their 1σ uncertainties to verify that the resulting transmission spectrum will remain unchangeable. Moreover, in the work of Wong et al. (2020), the authors considered that the uncertainties of the orbital parameters are correlated with the transit depth and this is possibly a reason to result in altered transmission spectrum. In the same sense, Edwards et al. (2020)

fixed the inclination of the system for the exoplanet WASP-76 b, in order to avoid the degeneracy of the impact parameter with the spectral slope. A similar approach was adopted for atmospheric studies on the exoplanets WASP-117 b(Anisman et al. 2020), for KELT-11 b (Changeat et al. 2020), for LHS-1140 b (Edwards et al. 2021b), for WASP-96 b (Yip et al. 2021), for HAT-P-14 b (Sheppard et al. 2021) and for KELT-1 b (von Essen et al. 2021). Moreover, the importance of using the correct orbital parameters in order to avoid alterations of the spectrum due to the limb darkening effect was pinpointed also in the works of Chen et al. (2021), Edwards & Stotesbury (2021), Fu et al. (2021), Arfaux & Lavvas (2022) and Li et al. (2023).

However, even though the impact parameter degeneracy can explain some misinterpretations of the transmission spectra, there are individual cases that it was not the main driver of the discrepancy. One example is described in the work of Murgas et al. (2020), where the impact parameter degeneracy was used in order to solve discrepancies regarding the atmospheric characterization of WASP-69 b. The inconsistency was identified between measurements obtained from HST/WFC3 (Wide-field camera 3 from the Hubble Space Telescope) and OSIRIS/GTC (Optical System for Imaging and low-Intermediate-Resolution Integrated Spectroscopy at Gran Telescopio CANARIAS). The OSIRIS spectrum appears higher in comparison with the WFC3 transmission spectrum yielding an overall offset in $\Delta R_p/R_s$ of ~ 0.00221. The reanalysis included both datasets from the different instruments and the same orbital parameters were used as fixed parameters during the transit light curve fit process. Nevertheless, the authors concluded that the observed offset induced with the previous use of different orbital parameters, could not be explained with the impact parameter degeneracy, since it was smaller with $\Delta R_p/R_s$ of ~ 0.00076. Both Murgas et al. (2020) and later on Khalafinejad et al. (2021) attributed the inconsistency rather to stellar activity. Similarly, in the work of Jiang et al. (2021) for inconsistencies between 2 datasets of HAT-P-12 b, from OSIRIS/GTC, the authors attributed the observed offsets due to stellar spots and faculae, rather than the different orbital parameters employed in the analysis.

We see that potentially, in practice, there are definitely more error sources to consider that are able to shape the transmission spectra, especially regarding stellar activity phenomena. Nonetheless, the quantification of the impact parameter degeneracy in Chapter 4 and in Alexoudi et al. (2020), driven by the limb-darkening, and especially its ability to introduce positive or negative slopes, that can reach up to at least one scale height, should be taken into consideration for the atmospheric characterization of exoplanets. In Rackham et al. (2022), this phenomenon is identified as a major influence on the retrieved transmission spectra, and in Allen et al. (2022) as a source for spurious features in the transit spectrum, if it is not correctly accounted for.

7.2 On photometric studies of exoplanets with TESS

The photometric investigations with TESS, of systems of particular interest, are described in Chapters 5 and 6. High quality photometric precision is able to provide the most suitable orbital parameters and transit depth for the correct construction of an optical transmission spectrum. Even though TESS's broadband filter covers all the wavelengths from 600 - 1000 nm, it is of particular interest to investigate how known exoplanetary systems are consistent with ground-based observations regarding the presence of clouds, for example, or the presence or absence of water vapor at the 900nm (z' band) (e.g., Yang et al. 2022).

In this dissertation, I investigated two samples of different sets of exoplanet populations with particular interest, as they were revisited by TESS. The first investigation refers to a sample of 10 inflated hot-Jupiters. The planetary radius investigation of those irradiated planets has shown a tentative trend that grazing systems have radii always overestimated by ground-based investigations. Therefore, during the second investigation, I proceeded with a refinement of the planetary radii of a rich sample of known grazing (or nearly-grazing) systems, in order to investigate this hypothesis and to make a comparison between space- and ground-based parameter estimations. Last but not least, as pinpointed in Chapter 4, grazing systems are those that suffer mostly from the degeneracy of the orbital parameters with the optical slope. Therefore, this parameter refinement is of particular importance, for future atmospheric characterization of grazing transiting exoplanets.

7.2.1 Investigation of 10 inflated hot Jupiters with TESS

One surprising thing about hot Jupiters is that they are usually found to have larger planetary radii, by $10\% - 15\%$ (e.g., Stassun et al. 2018), than they were expected from evolutionary models (e.g., Dawson & Johnson 2018; Komacek et al. 2022). Being in close-in orbits, the strong stellar flux of the host star is able to heat their interiors and inflate them (e.g., Enoch et al. 2012; Fortney et al. 2021). Those targets are particularly favorable for atmospheric characterization with transmission spectroscopy because of their strong transmission signals produced by their inflated, puffy atmospheres (Komacek et al. 2022). TESS is expected to provide accurate determination of the major systems' parameters for our sample of irradiated hot Jupiters and solve potential discrepancies regarding their atmosphere.

Furthermore, TESS can be valuable in determining interior structure and dynamics of those systems. One way to investigate the interior structure of inflated hot Jupiters and derive a bulk composition of the planet, is to develop theoretical structure models. One major component of those models is a measurement of a very precise planetary radius parameter. If the age of the host is known, and the mass of the planet, then the composition can be determined by comparing the predicted radius from the model with the radius determined by the observations. This is particularly challenging for inflated hot-Jupiters (Sarkis et al. 2021). An example is presented in the works of Batygin & Stevenson (2010) and Wu & Lithwick (2013), for the exoplanet TrEs-4 b. The structure model of the first group suggested a radius for the planet of $1.9R_J$, while the one of the second group yielded a planetary radius of $1.6R_J$. This discrepancy can be attributed to the different assumptions adopted in each model's procedure.

In Chapter 5 and in Alexoudi (2022), it is presented a planetary radius determination (confirmation or refinement) of a sample of inflated giant exoplanets using datasets from TESS. In that investigation, TESS and ground-based investigations found to be in agreement, regarding the orbital parameters of the majority of these systems (within $1 - 2\sigma$). However, a discrepancy regarding the planetary radius of WASP-93 b was solved, the planetary radius of WASP-140 b was refined by approximately 12%, while a better precision on its asymmetric radius uncertainty by approximately 86% and 67% was reported as well. Moreover, the orbital parameters of WASP-120 b were refined by 2σ. In practice, three inflated hot Jupiters are refined and based on those new measurements, new estimations on their atmospheres and interior structures can be inferred in the future.

Even though the sample was small, there was a tendency for systems with $b > 0.6$ to have always larger radii, as derived with ground-based measurements. This outcome triggered the third investigation of this dissertation, aiming to confirm or reject this hypothesis with a larger sample of nearly-grazing to fully-grazing exoplanet systems.

7.2.2 Comparative study of the radii of (nearly-) grazing systems

This comparative study of 43 known hot-Jupiters with $b > 0.6$ (presented in Chapter 6 and in Alexoudi et al. (2023)) is a small population study, aiming to investigate if the planetary radii derived from ground-based observations are always overestimated. One of the main results in that work is that, the trend regarding overestimation of the planetary radii from the ground, is not valid from all the exoplanets of the sample, but rather only for the systems with $b > 0.9$. Moreover, this overestimation was quantified, and it was found equal to $0.15R_J$, which is particularly significant. The refined parameters of some of the systems in this study, can be used in order to confirm or reject possible atmospheric characterizations, since it was shown that grazing systems are more likely to be vulnerable towards the impact parameter degeneracy with the spectral slope (see Chapter 4 and Alexoudi et al. (2020)). In many cases, the uncertainties on the orbital parameters were refined significantly, being able to constrain the optical slopes of those systems in future studies. Currently, transmission spectra of fully-grazing systems are challenging to retrieve, therefore, revisiting of those systems in order to assess their atmospheres might be a possibility for future observatories, combined with advanced transit modeling techniques that can account for the peculiar geometries of their grazing orbits. The grazing nature for some systems was also redefined with their parameter refinement. However, from the photometric investigation of the majority of the systems in this work with TESS, it is shown that ground- and space- based findings are mostly in agreement.

8 End notes and Outlook

To conclude, the impact parameter degeneracy must be kept in mind for the correct interpretation of the transmission spectrum resulting from the atmospheres of exoplanets. This phenomenon can explain some discrepancies when the employed orbital parameters for the light curve analysis differ a lot between independent investigations. Currently, TESS can provide sufficient photometric precision for the planetary radius derivation and most importantly for the impact parameter estimation. High quality datasets from space can confirm ground-based findings regarding clouds or hazes in an atmosphere and can determine accurately the orbital parameters to employ for the light curve modeling of systems observed from ground-based instruments.

A key-role of TESS regarding solutions to reported discrepancies, is that it can provide insights on the misconceptions of spectra due to an offset that cannot be explained otherwise. For example, in Fig. 8.1, we see how a single TESS measurement can discern between two different interpretations of this exoplanet's atmosphere from two different groups, Jordán et al. (2013) and Nikolov et al. (2015). The discrepancy was mentioned also in Chapter 4, but it could not be solved based on the impact parameter degeneracy. Now with TESS, with multiple sectors of observations, discrepancies such as the one mentioned for WASP-6b can be solved. In the work of Carter et al. (2020) only one sector of observations of this exoplanet was analyzed using TESS, while in the currently ongoing work of Alexoudi et al. (in prep.), an analysis containing datasets from two TESS sectors of WASP-6b is presented. Both TESS investigations agree with the spectrum suggested by Nikolov et al. (2015).

The majority of this work focused on TESS observations, since during the course of this dissertation it was a powerful tool with publicly available datasets to facilitate an abundance of project possibilities. However, the access to space-based instruments is in general a high-competitive process and comparative studies like the planetary radii refinement of inflated giants or of grazing systems investigations (see Chapters 5 and 6), would not be possible considering writing observing proposals for each target. Undoubtedly, TESS has been a massive benefit for the community since its first observations in 2018.

The future of transiting exoplanet studies appears brighter than ever, as discrepancies regarding their atmospheric characterization, hopefully will no longer be an issue, as more powerful instruments will reach the unparalleled precision, in order to construct the transmission spectra beyond doubt. Currently, a space mission which, within only its first year of operations, has achieved major advances in atmospheric characterization of exoplanetary systems, with significant parameter precision, is the James Webb Space Telescope (JWST) Mission (Gardner et al. 2006). JWST managed to provide atmospheric characterization of exoplanets revealing an abundance of elements and features, e.g., in WASP-39 b (Rustamkulov et al. 2022)

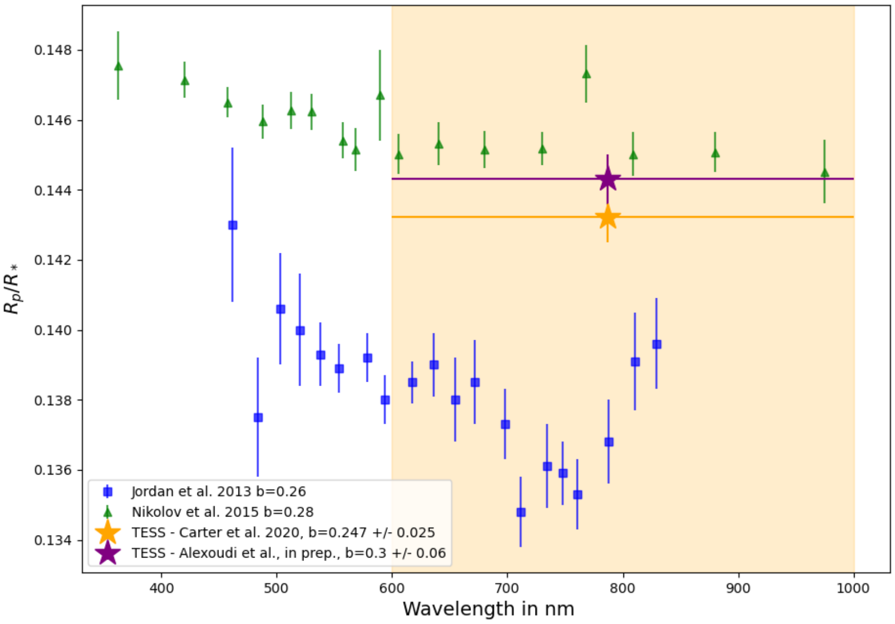

Figure 8.1: Reported discrepancy between transmission spectra constructed for WASP-6b by Jordán et al. (2013) (blue squares) and Nikolov et al. (2015) (green triangles). TESS observations from a single sector(Carter et al. 2020) yield a result (orange star) towards an agreement with Nikolov et al. (2015). In an ongoing study by Alexoudi et al. (in prep.), the analysis of two sectors observation datasets with TESS, yield a result (purple star) which is definitely compatible with Nikolov et al. (2015). The x-axis errorbars for the TESS measurements correspond to the wavelength coverage by TESS's broadband filter.

and WASP-96 b[1]. Moreover, a cloud coverage was also identified for the exoplanet LHS 475 b (Lustig-Yaeger et al. 2023), which is a terrestrial planet. Missions like PLATO (Rauer et al. 2014) and ARIEL (Tinetti et al. 2018) will be dedicated to exoplanet detection and characterization, along with the next generation of ground-based telescopes e.g., the Giant Magellan Telescope (GMT) [2], and the Thirty-Meter Telescope (TMT) [3].

Therefore, many more highlights of exoplanetary characterization are expected during the years to come, with an ultimate goal to identify a second Earth and assess precisely its properties. This thesis can assist solving potential discrepancies regarding the atmospheric characterizations of transiting exoplanets, possibly of terrestrial worlds and eventually Earth-like planets around Solar-type stars, where the impact parameter degeneracy effects could be stronger. Then, an investigation of the persistence of the impact parameter degeneracy in practice and on transmission spectra of these systems will definitely need to be re-addressed again.

---

[1] https://webbtelescope.org/contents/news-releases/2022/news-2022-032

[2] https://giantmagellan.org/

[3] https://www.tmt.org/

9 Appendix - A

9.1 Best fit transit models and corner plots for all the fit parameters.

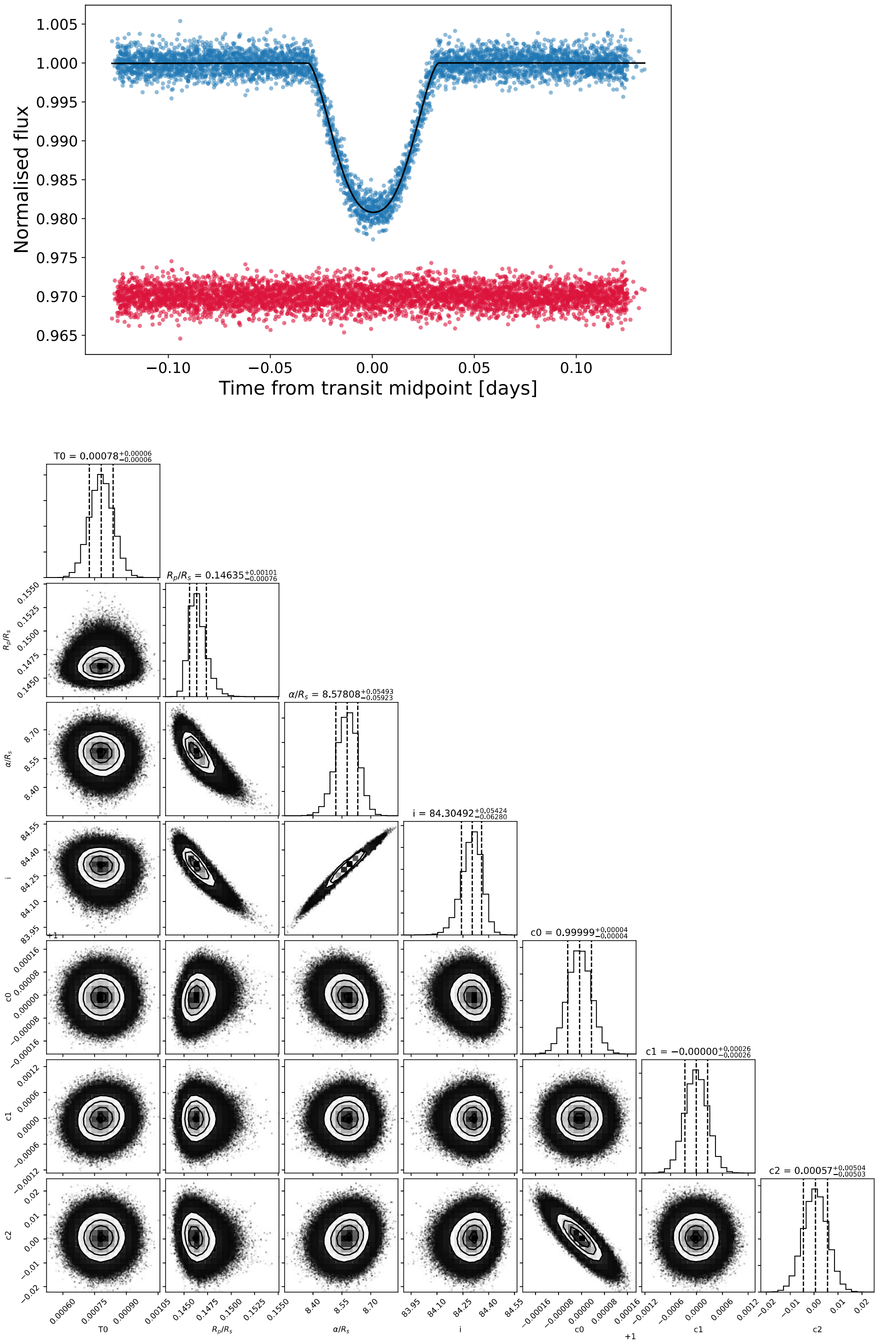

Figure 9.1: In the upper panel, we show the folded TESS light curves of WASP-140 b (blue dots) along with the best fit transit model (black solid line). The residuals are presented with red dots and an offset for clarity. In the lower panel, we show the corner plot of the best fit parameters. It is the 2D projection of the sample plotted in a way to show covariance between the parameters.

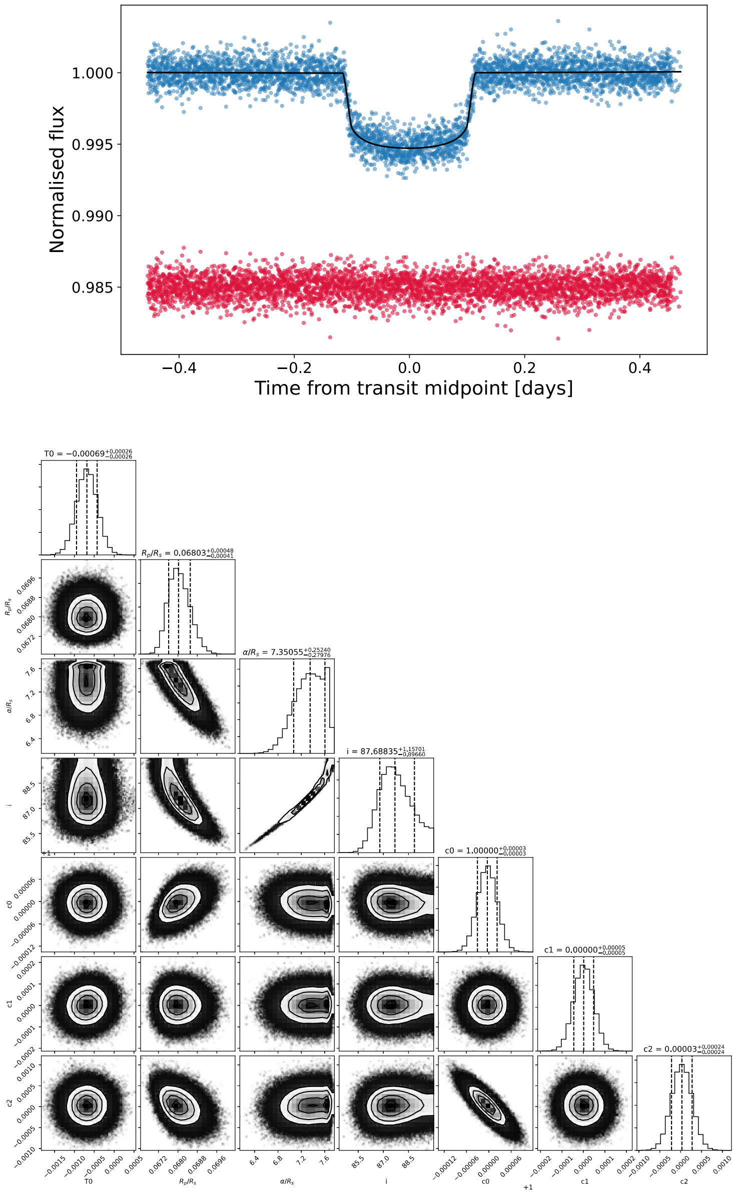

Figure 9.2: The same as Fig. 9.1, but for the exoplanet WASP-136 b.

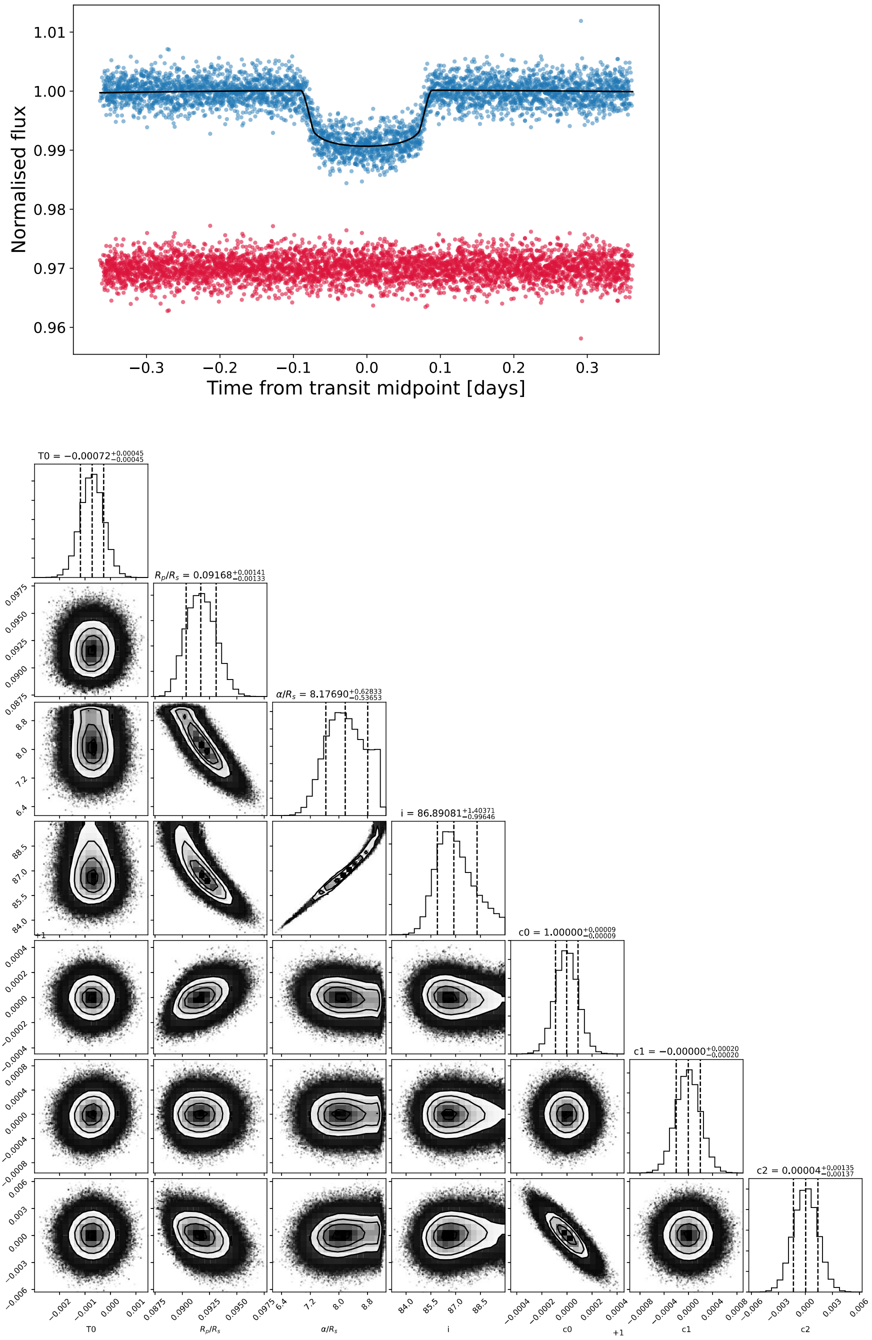

Figure 9.3: The same as Fig. 9.1, but for the exoplanet WASP-113 b.

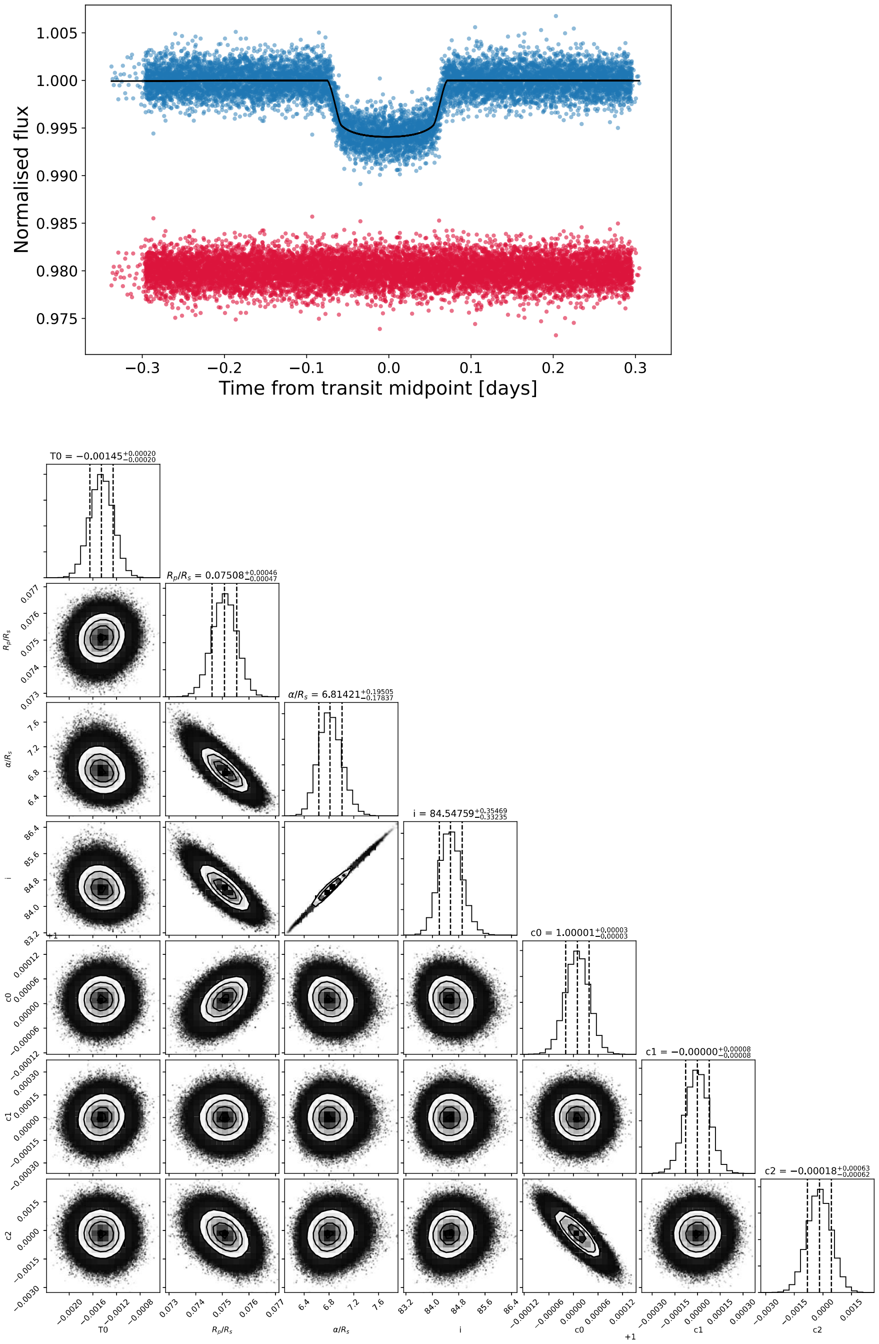

Figure 9.4: The same as Fig. 9.1, but for the exoplanet WASP-120 b.

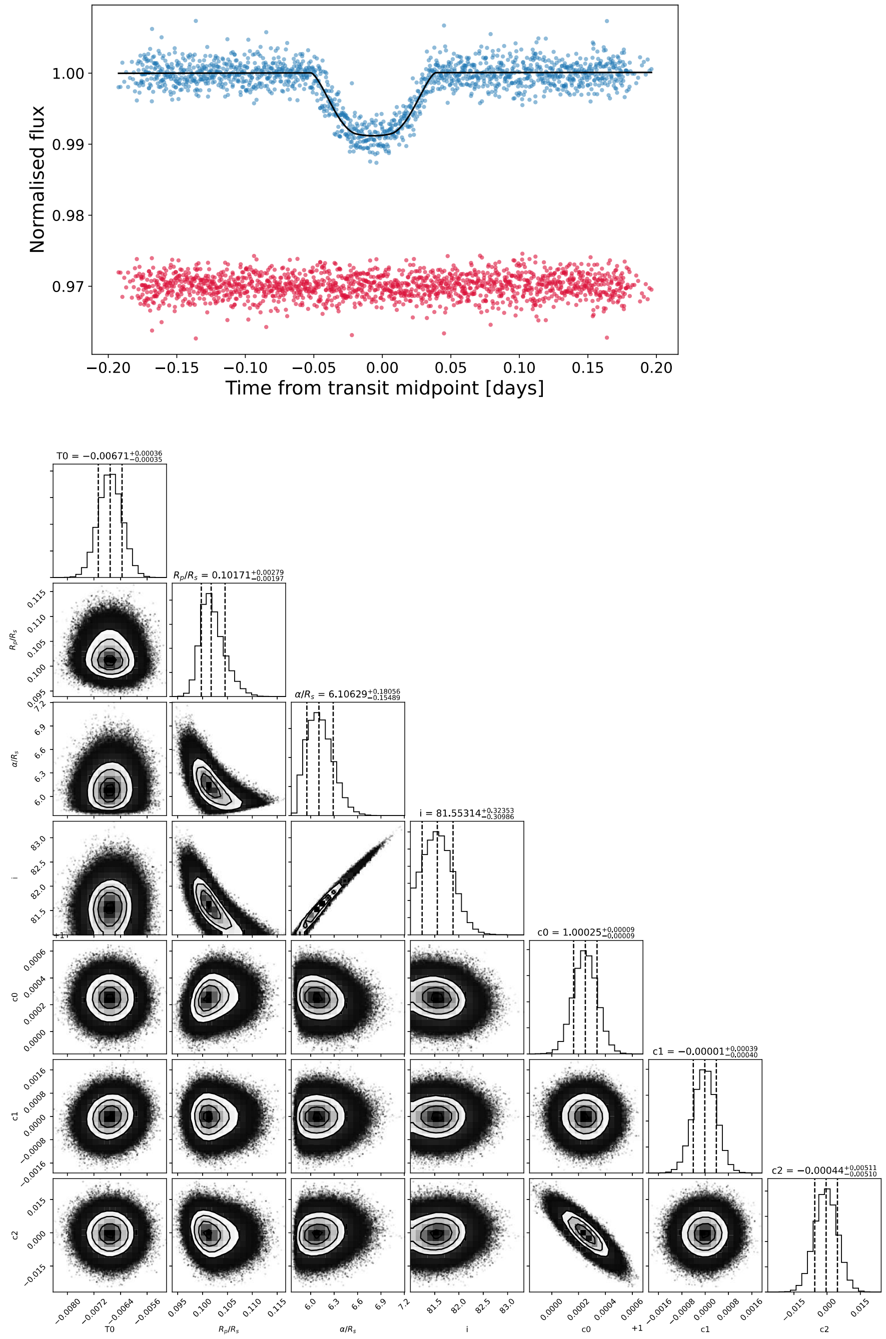

Figure 9.5: The same as Fig. 9.1, but for the exoplanet WASP-93 b.

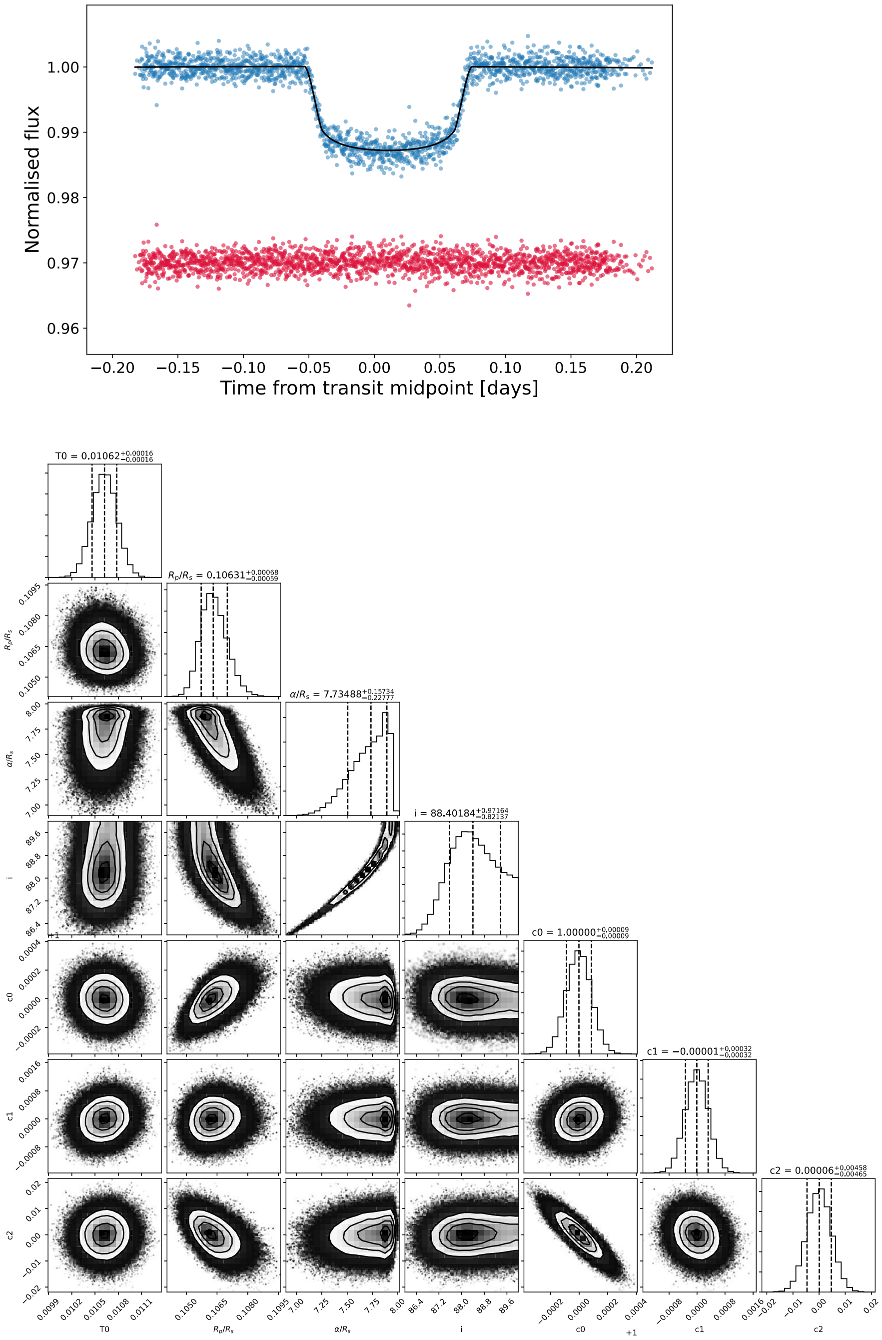

Figure 9.6: The same as Fig. 9.1, but for the exoplanet HAT-P-16 b.

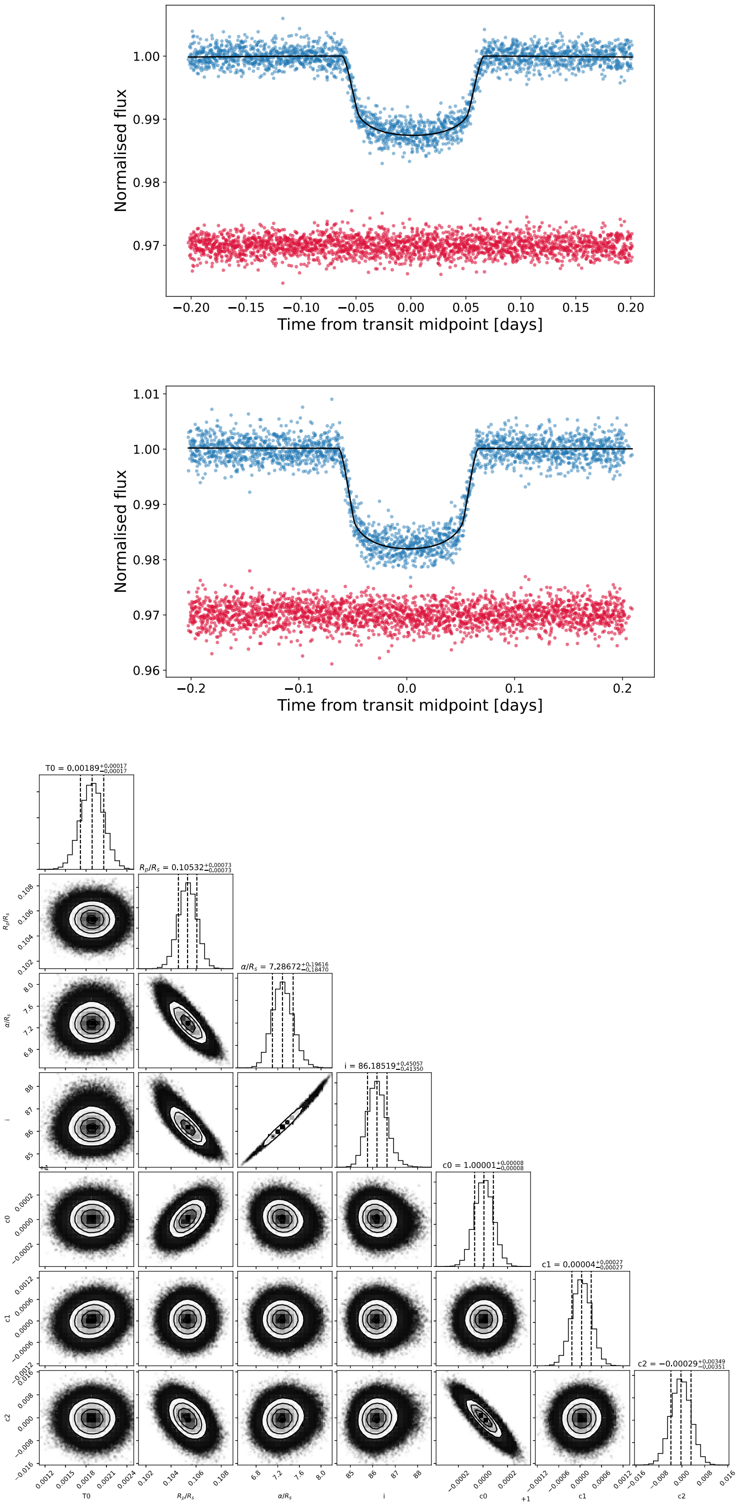

Figure 9.7: Best fit transit model for the TESS light curves of WASP-123 b. On the upper left panel there are observations from sector 27 and on the upper right panel from sector 13. On the lower panel, the corner plot of the best fit parameters for WASP-123 b.

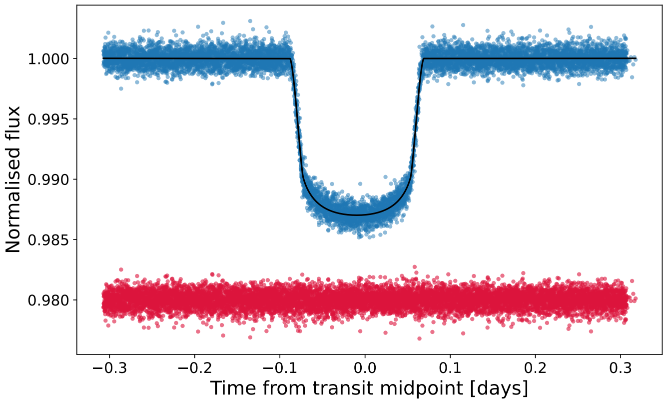

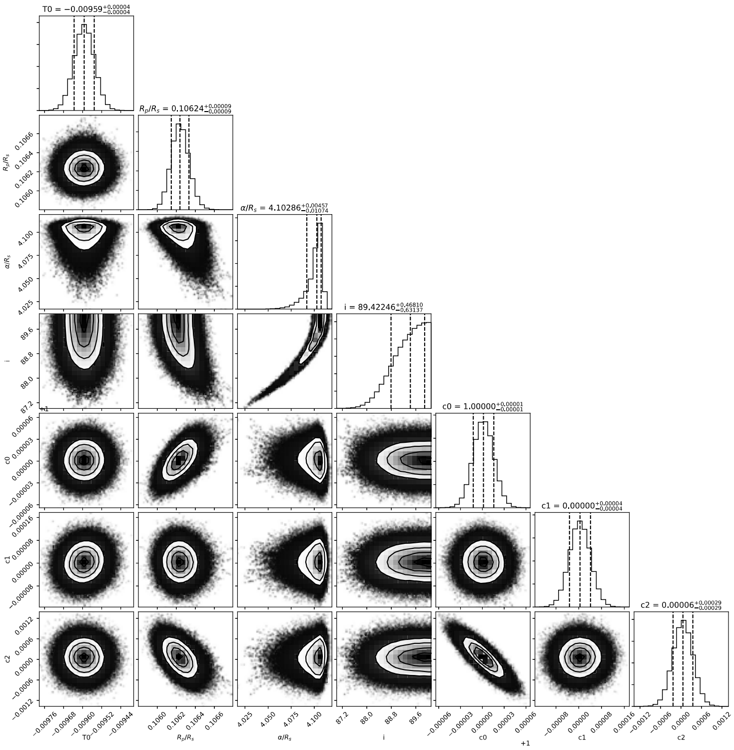

Figure 9.8: The same as Fig. 9.1, but for the exoplanet WASP-76 b.

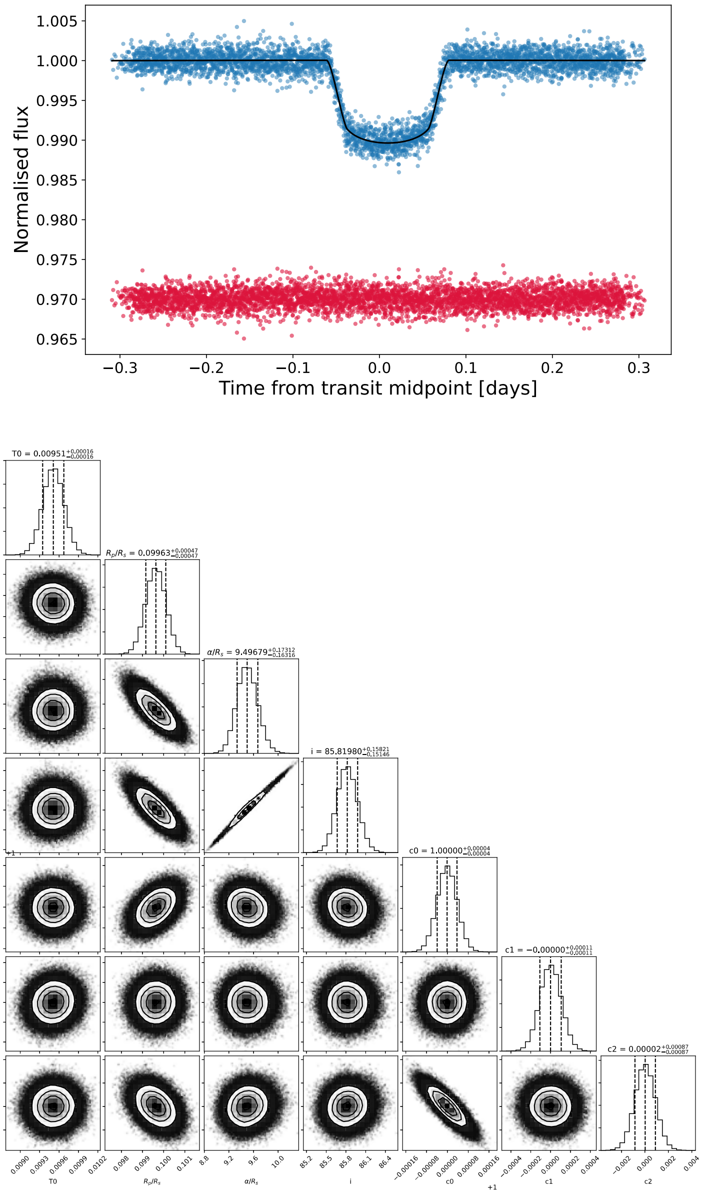

Figure 9.9: The same as Fig. 9.1, but for the exoplanet WASP-20 b.

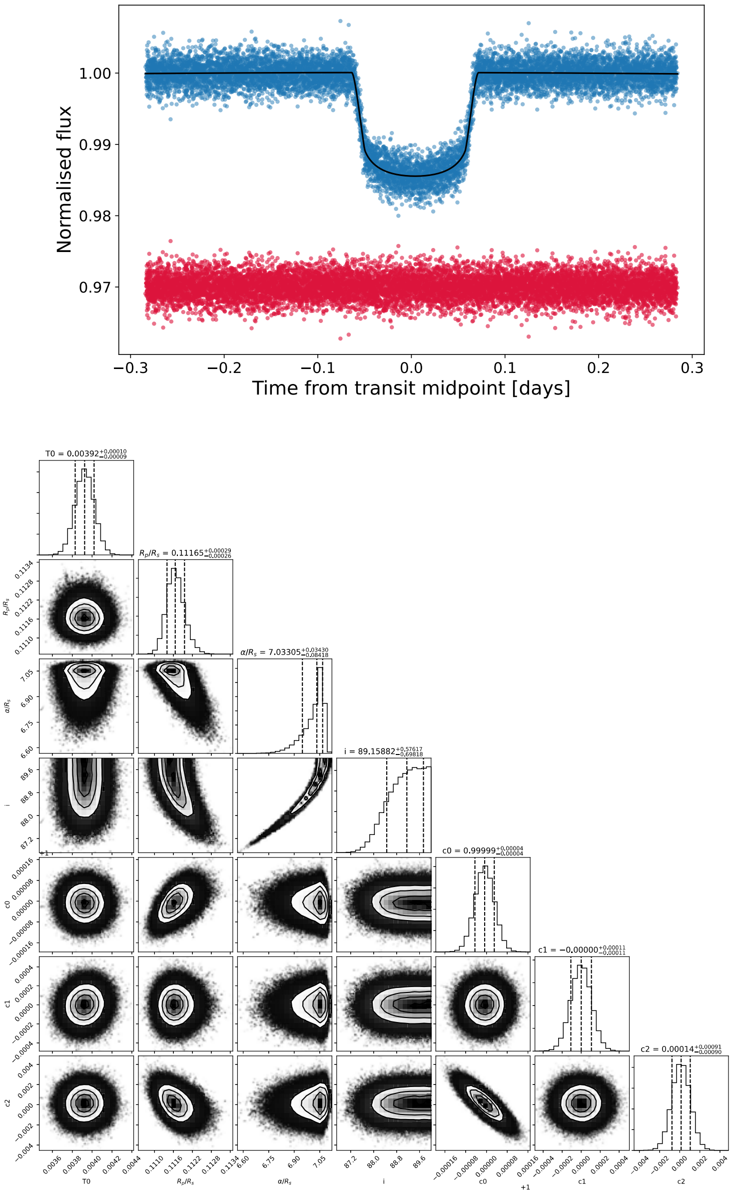

Figure 9.10: The same as Fig. 9.1, but for the exoplanet WASP-108 b.

10 Appendix - B

10.1 Example of corner Plot for the best fit parameter determination

10.2 Non-grazing systems of our sample

10.3 Information on TESS observations

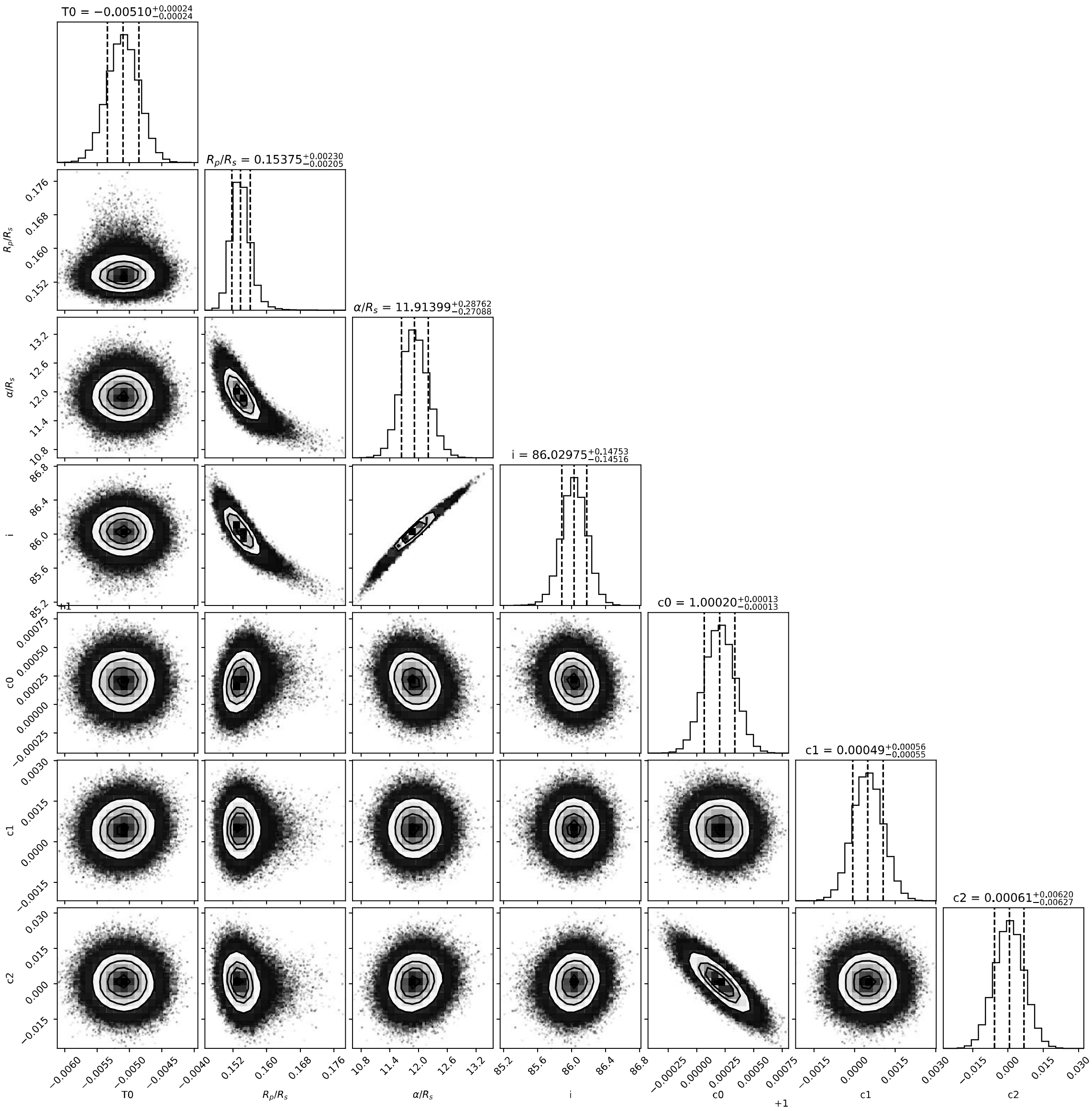

Figure 10.1: The corner plot of the best fit parameters for WASP-183 b. It is the 2D projection of the sample plotted in a way to show covariance between the parameters.

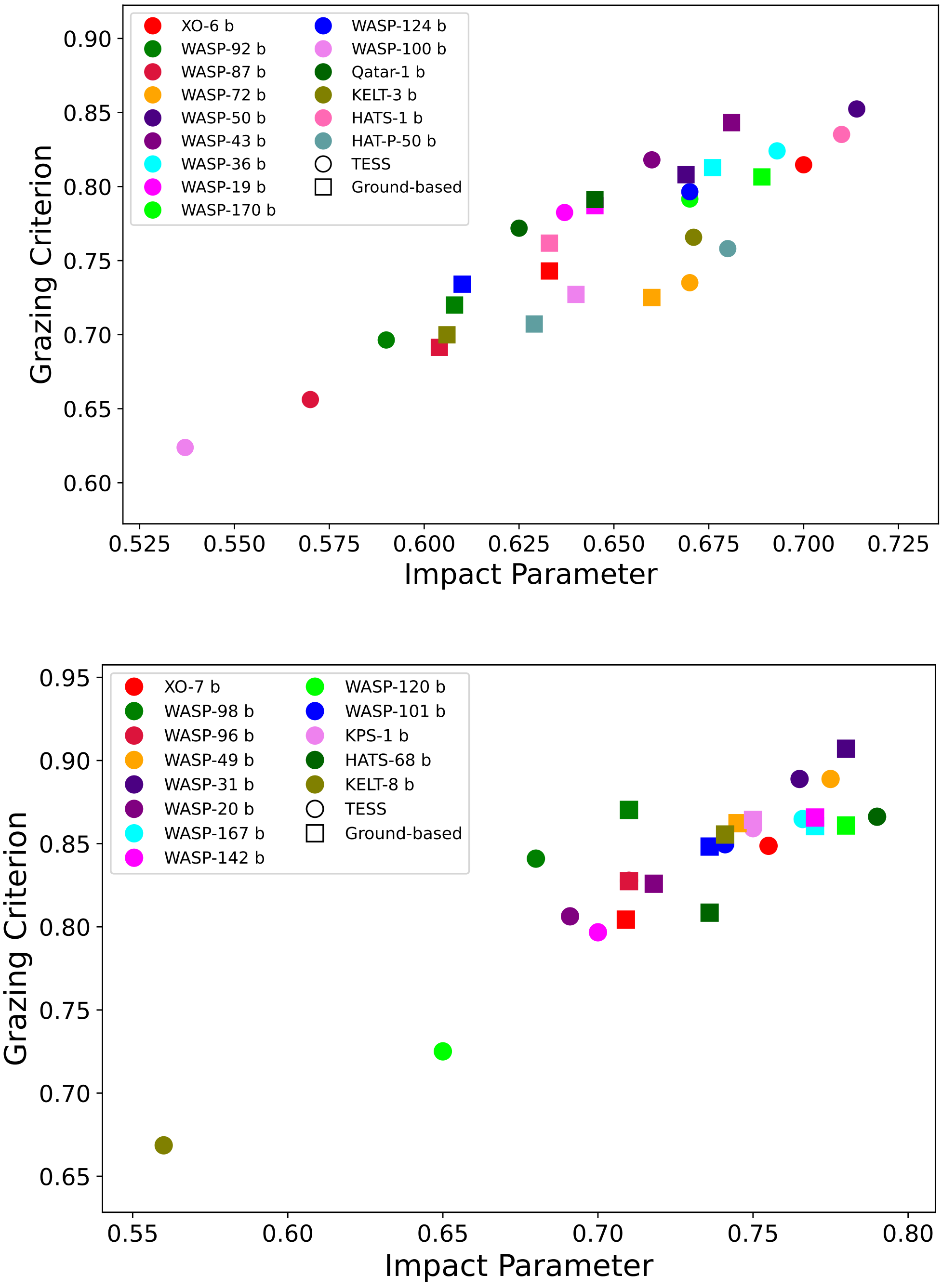

Figure 10.2: The same as Fig. 6.8, but for the exoplanets of Group A (top panel) and for Group B (bottom panel).

Target	Sector	Cycle	Camera
XO-6 b	19	2	2
	20	2	2
	26	2	4
	40	4	4
WASP-92 b	23	2	3
	24	2	2
	25	2	2
WASP-87A b	10	1	2
	11	1	2
	37	3	2
WASP-72 b	3	1	2
	4	1	2
	30	3	2
	31	3	2
WASP-50 b	4	1	1
	31	3	1
WASP-43 b(Davoudi et al. 2021)	9	1	1
	35	3	1
WASP-36 b	8	1	1
	34	3	1
WASP-19 b	9	1	2
	36	3	2
WASP-170 b	35	3	2
WASP-124 b	1	1	1
WASP-100 b (Jansen & Kipping 2020)	From 1 to 13	1	4
QATAR-1 b	17	2	3
	21	2	4
	24	2	3
	25	2	3
	41	4	2
KELT-3 b	21	2	1
HATS-1 b	10	1	1
	36	3	1
HAT-P-50 b	7	1	1
	34	3	1
	44	4	4
	45	4	2

Table 10.1: The TESS observations of the exoplanets in Group A, that took place in recent investigations in the literature and this current work. There is information on the sector (multiple sectors in many cases), the observing cycle and the camera that was used for that certain observation.

Target	Sector	Cycle	Camera
XO-7 b	25	2	3
	26	2	3
	40	4	3
WASP-98 b	4	1	2
	31	3	2
WASP-96 b	2	1	2
	29	3	2
WASP-49A b	6	1	2
	33	3	2
WASP-31 b	9	1	1
	36	3	1
WASP-20A b (Alexoudi 2022)	2	1	1
	29	3	1
WASP-167 b	10	1	1
	37	3	1
WASP-142 b	8	1	2
	35	3	2
WASP-120 b (Alexoudi 2022)	4	1	3
	5	1	3
	30	3	3
	31	3	3
WASP-101 b	6	1	2
	33	3	2
KPS-1 b	21	2	2
	41	4	4
HATS-68 b	28	3	3
	29	3	3
KELT-8 b	26	2	1
	40	4	1

Table 10.2: Similar to Table 10.1, but for the exoplanets of Group B.

Target	Sector	Cycle	Camera
WASP-75 b	42	4	1
WASP-192 b	38	3	1
WASP-164 b	28	3	2
TrES-3 b	25	2	2
	26	2	2
	40	4	2
TrES-2 b	26	2	2
	40	4	2
	41	4	2
KELT-14 b	7	1	3
	33	3	3
	34	3	3
HAT-P-56 b	43	4	4
	44	4	3
	45	4	1
HAT-P-30 b	7	1	1
	34	3	1

Table 10.3: Similar to Table 10.2, but for the exoplanets of Group C.

Target	Sector	Cycle	Camera
WASP-93 b (Alexoudi 2022)	17	2	2
WASP-34 b	9	1	1
	36	3	1
WASP-183 b	35	3	1
	45	4	4
	46	4	3
WASP-140 b (Alexoudi 2022)	4	1	2
	5	1	2
	31	3	2
WASP-174 b (Mancini et al. 2020)	10	1	2
WASP-168 b	32	3	3
	33	3	3
	34	3	3
WASP-177 b	42	4	1

Table 10.4: Similar to Table 10.3, but for the exoplanets of Group D.

Bibliography

Addison, B. C., Tinney, C. G., Wright, D. J., & Bayliss, D. 2016, ApJ, 823, 29

Addison, B. C., Wang, S., Johnson, M. C., et al. 2018, AJ, 156, 197

Ahrer, The JWST Transiting Exoplanet Community Early Release Science Team, E.-M., Alderson, L., et al. 2022, arXiv e-prints, arXiv:2208.11692

Akeson, R. L., Chen, X., Ciardi, D., et al. 2013, PASP, 125, 989

Alam, M. K., Lopez-Morales, M., Nikolov, N., et al. 2020, arXiv e-prints, arXiv:2005.11293

Alexoudi, X. 2022, Astronomische Nachrichten, 343, e24012

Alexoudi, X., Dineva, E., Barnes, S., & Strassmeier, K. G. 2023, Astronomische Nachrichten, 344, easna.20220075

Alexoudi, X., Mallonn, M., Keles, E., et al. 2020, A&A, 640, A134

Alexoudi, X., Mallonn, M., von Essen, C., et al. 2018, A&A, 620, A142

Allen, N. H., Espinoza, N., Jordán, A., et al. 2022, AJ, 164, 153

Alonso, R., Brown, T. M., Charbonneau, D., et al. 2007, in Astronomical Society of the Pacific Conference Series, Vol. 366, Transiting Extrapolar Planets Workshop, ed. C. Afonso, D. Weldrake, & T. Henning, 13

Anderson, D. R., Brown, D. J. A., Collier Cameron, A., et al. 2014, arXiv e-prints, arXiv:1410.3449

Anderson, D. R., Collier Cameron, A., Hellier, C., et al. 2015, A&A, 575, A61

Anderson, D. R., Collier Cameron, A., Hellier, C., et al. 2011, A&A, 531, A60

Anisman, L. O., Edwards, B., Changeat, Q., et al. 2020, AJ, 160, 233

Arfaux, A. & Lavvas, P. 2022, MNRAS, 515, 4753

Auvergne, M., Bodin, P., Boisnard, L., et al. 2009, A&A, 506, 411

Bakos, G., Noyes, R. W., Kovács, G., et al. 2004, PASP, 116, 266

Bakos, G. Á. 2018, The HATNet and HATSouth Exoplanet Surveys, ed. H. J. Deeg & J. A. Belmonte, 111

Barclay, T., Pepper, J., & Quintana, E. V. 2018, ApJS, 239, 2

Barge, P., Baglin, A., Auvergne, M., & CoRoT Team. 2008, in Exoplanets: Detection, Formation and Dynamics, ed. Y.-S. Sun, S. Ferraz-Mello, & J.-L. Zhou, Vol. 249, 3–16

Barkaoui, K., Burdanov, A., Hellier, C., et al. 2019, AJ, 157, 43

Barros, S. C. C., Brown, D. J. A., Hébrard, G., et al. 2016, A&A, 593, A113

Batygin, K. & Stevenson, D. J. 2010, ApJL, 714, L238

Bodenheimer, P., Laughlin, G., & Lin, D. N. C. 2003, ApJ, 592, 555

Bodenheimer, P., Lin, D. N. C., & Mardling, R. A. 2001, ApJ, 548, 466

Bohn, A. J., Southworth, J., Ginski, C., et al. 2020, A&A, 635, A73

Borucki, W. J., Koch, D., Basri, G., et al. 2010, Science, 327, 977

Buchhave, L. A., Bakos, G. Á., Hartman, J. D., et al. 2010, ApJ, 720, 1118

Burdanov, A., Benni, P., Sokov, E., et al. 2018, Publications of the Astronomical Society of the Pacific, 130, 074401

Burrows, A. S. 2014, Nat, 513, 345

Carter, A. L., Nikolov, N., Sing, D. K., et al. 2020, MNRAS, 494, 5449

Chachan, Y., Jontof-Hutter, D., Knutson, H. A., et al. 2020, AJ, 160, 201

Chakrabarty, A. & Sengupta, S. 2019, AJ, 158, 39

Changeat, Q., Edwards, B., Al-Refaie, A. F., et al. 2020, AJ, 160, 260

Charbonneau, D., Brown, T. M., Latham, D. W., & Mayor, M. 2000, ApJL, 529, L45

Charbonneau, D., Brown, T. M., Noyes, R. W., & Gilliland, R. L. 2002, ApJ, 568, 377

Chen, G., Guenther, E. W., Pallé, E., et al. 2017, A&A, 600, A138

Chen, G., Pallé, E., Parviainen, H., Murgas, F., & Yan, F. 2021, ApJL, 913, L16

Ciardi, D. R., Beichman, C. A., Horch, E. P., & Howell, S. B. 2015, ApJ, 805, 16

Ciceri, S., Mancini, L., Southworth, J., et al. 2013, A&A, 557, A30

Claret, A. 2000, A&A, 363, 1081

Claret, A. 2017, A&A, 600, A30

Claret, A. & Bloemen, S. 2011, A&A, 529, A75

Collins, K. A., Kielkopf, J. F., & Stassun, K. G. 2017, AJ, 153, 78

Crouzet, N., Healy, B. F., Hébrard, G., et al. 2020, AJ, 159, 44

Crouzet, N., McCullough, P. R., Long, D., et al. 2017, AJ, 153, 94

Davis, A. B., Wang, S., Jones, M., et al. 2020, AJ, 160, 229

Davoudi, F., Özgür Baştürk, Yalçınkaya, S., Esmer, E. M., & Safari, H. 2021, AJ, 162, 210

Dawson, R. I. & Johnson, J. A. 2018, ARA&A, 56, 175

Daylan, T., Günther, M. N., Mikal-Evans, T., et al. 2021, AJ, 161, 131

de Mooij, E. J. W., Brogi, M., de Kok, R. J., et al. 2013, ApJ, 771, 109

de Wit, J. & Seager, S. 2013, Science, 342, 1473

Deming, L. D. & Seager, S. 2017, J. Geophys. Res. Planets, 122, 53

Dumusque, X. 2018, A&A, 620, A47

Eastman, J., Siverd, R., & Gaudi, B. S. 2010, PASP, 122, 935

Edwards, B., Changeat, Q., Baeyens, R., et al. 2020, AJ, 160, 8

Edwards, B., Changeat, Q., Mori, M., et al. 2021a, AJ, 161, 44

Edwards, B., Changeat, Q., Mori, M., et al. 2021b, AJ, 161, 44

Edwards, B. & Stotesbury, I. 2021, AJ, 161, 266

Ehrenreich, D., Lovis, C., Allart, R., et al. 2020, Nat, 580, 597

Enoch, B., Collier Cameron, A., & Horne, K. 2012, A&A, 540, A99

Espinoza, N., Brahm, R., Henning, T., et al. 2020, MNRAS, 491, 2982

Espinoza, N. & Jordán, A. 2015, MNRAS, 450, 1879

Espinoza, N. & Jordán, A. 2016, MNRAS, 457, 3573

Evans, D. F., Southworth, J., & Smalley, B. 2016, ApJL, 833, L19

Fischer, P. D., Knutson, H. A., Sing, D. K., et al. 2016, ApJ, 827, 19

Foreman-Mackey, D., Hogg, D. W., Lang, D., & Goodman, J. 2013, PASP, 125, 306

Fortney, J. J., Dawson, R. I., & Komacek, T. D. 2021, J. Geophys. Res. Planets, 126, e06629

Fortney, J. J., Marley, M. S., & Barnes, J. W. 2007, ApJ, 659, 1661

Fu, G., Deming, D., Lothringer, J., et al. 2021, AJ, 162, 108

Fulton, B. J., Collins, K. A., Gaudi, B. S., et al. 2015, ApJ, 810, 30

Gaia Collaboration, Brown, A. G. A., Vallenari, A., et al. 2018, A&A, 616, A1

Gajdoš, P., Vaňko, M., Jakubík, M., et al. 2019, MNRAS, 485, 3580

Gao, P., Wakeford, H. R., Moran, S. E., & Parmentier, V. 2021, J. Geophys. Res. Planets, 126, e06655

Gardner, J. P., Mather, J. C., Clampin, M., et al. 2006, Space Sci. Rev., 123, 485

Gibson, N. P., Aigrain, S., Barstow, J. K., et al. 2013a, MNRAS, 428, 3680

Gibson, N. P., Aigrain, S., Barstow, J. K., et al. 2013b, MNRAS, 436, 2974

Gibson, N. P., Nikolov, N., Sing, D. K., et al. 2017, MNRAS, 467, 4591

Gilbert, G. J. 2022, AJ, 163, 111

Gómez Maqueo Chew, Y., Faedi, F., Pollacco, D., et al. 2013, A&A, 559, A36

Guerrero, N. M., Seager, S., Huang, C. X., et al. 2021, ApJS, 254, 39

Guillot, T. & Showman, A. P. 2002, A&A, 385, 156

Guo, X., Crossfield, I. J. M., Dragomir, D., et al. 2020, AJ, 159, 239

Hartman, J. D., Bakos, G. Á., Bayliss, D., et al. 2019, AJ, 157, 55

Hartman, J. D., Bakos, G. Á., Torres, G., et al. 2009, ApJ, 706, 785

Hartman, J. D., Bhatti, W., Bakos, G. Á., et al. 2015, AJ, 150, 168

Haswell, C. A. 2010, Transiting Exoplanets (Cambridge University Press)

Hay, K. L., Collier-Cameron, A., Doyle, A. P., et al. 2016, MNRAS, 463, 3276

Hellier, C., Anderson, D. R., Barkaoui, K., et al. 2019a, MNRAS, 490, 1479

Hellier, C., Anderson, D. R., Bouchy, F., et al. 2019b, MNRAS, 482, 1379

Hellier, C., Anderson, D. R., Collier Cameron, A., et al. 2017, MNRAS, 465, 3693

Hellier, C., Anderson, D. R., Collier Cameron, A., et al. 2014, MNRAS, 440, 1982

Hellier, C., Anderson, D. R., Collier Cameron, A., et al. 2012, MNRAS, 426, 739

Howarth, I. D. 2011, MNRAS, 418, 1165

Howell, S. B., Sobeck, C., Haas, M., et al. 2014, PASP, 126, 398

Huang, C. X., Hartman, J. D., Bakos, G. Á., et al. 2015, AJ, 150, 85

Huitson, C. M., Sing, D. K., Pont, F., et al. 2013, MNRAS, 434, 3252

Jansen, T. & Kipping, D. 2020, MNRAS, 494, 4077

Jenkins, J. M., Twicken, J. D., McCauliff, S., et al. 2016, in Software and Cyberinfrastructure for Astronomy IV, ed. G. Chiozzi & J. C. Guzman, Vol. 9913, International Society for Optics and Photonics (SPIE), 1232 – 1251

Jiang, C., Chen, G., Pallé, E., et al. 2021, A&A, 656, A114

Jordán, A., Espinoza, N., Rabus, M., et al. 2013, ApJ, 778, 184

Khalafinejad, S., Molaverdikhani, K., Blecic, J., et al. 2021, A&A, 656, A142

Kipping, D. M. 2009, MNRAS, 396, 1797

Kipping, D. M. 2010, MNRAS, 407, 301

Kirk, J., Wheatley, P. J., Louden, T., et al. 2018, MNRAS, 474, 876

Kokori, A., Tsiaras, A., Edwards, B., et al. 2021, Experimental Astronomy

Komacek, T. D., Gao, P., Thorngren, D. P., May, E. M., & Tan, X. 2022, ApJL, 941, L40

Kreidberg, L. 2015, PASP, 127, 1161

Kreidberg, L. 2018, Handbook of Exoplanets, 2083–2105

Kreidberg, L., Bean, J. L., Désert, J.-M., et al. 2014, Nat, 505, 69

Kreidberg, L., Line, M. R., Thorngren, D., Morley, C. V., & Stevenson, K. B. 2018, ApJL, 858, L6

Kurucz, R. L. 1979, ApJS, 40, 1

Lam, K. W. F., Faedi, F., Brown, D. J. A., et al. 2017, A&A, 599, A3

Laughlin, G., Crismani, M., & Adams, F. C. 2011, ApJL, 729, L7

Leconte, J., Chabrier, G., Baraffe, I., & Levrard, B. 2010, A&A, 516, A64

Lendl, M., Anderson, D. R., Bonfanti, A., et al. 2019, MNRAS, 482, 301

Lendl, M., Anderson, D. R., Collier-Cameron, A., et al. 2012, A&A, 544, A72

Lendl, M., Gillon, M., Queloz, D., et al. 2013, A&A, 552, A2

Li, X.-K., Chen, G., Zhao, H.-B., & Wang, H.-C. 2023, Research in Astronomy and Astrophysics, 23, 025018

Lightkurve Collaboration, Cardoso, J. V. d. M., Hedges, C., et al. 2018, Lightkurve: Kepler and TESS time series analysis in Python, Astrophysics Source Code Library

Lillo-Box, J., Barrado, D., Santos, N. C., et al. 2015, A&A, 577, A105

Littlefield, C., Garnavich, P., Mukai, K., et al. 2019, ApJ, 881, 141

Louden, T., Wheatley, P. J., Irwin, P. G. J., Kirk, J., & Skillen, I. 2017, MNRAS, 470, 742

Lustig-Yaeger, J., Fu, G., May, E. M., et al. 2023, arXiv e-prints, arXiv:2301.04191

MacDonald, R. J., Goyal, J. M., & Lewis, N. K. 2020, ApJL, 893, L43

Maciejewski, G., Dimitrov, D., Mancini, L., et al. 2016, Acta Astron., 66, 55

Mackebrandt, F., Mallonn, M., Ohlert, J. M., et al. 2017, A&A, 608, A26

Madhusudhan, N. 2012, ApJ, 758, 36

Madhusudhan, N. 2019, Annu. Rev. Astron. Astrophys., 57, 617

Mallonn, M., Bernt, I., Herrero, E., et al. 2016, MNRAS, 463, 604

Mallonn, M., Herrero, E., Juvan, I. G., et al. 2018, A&A, 614, A35

Mallonn, M., Köhler, J., Alexoudi, X., et al. 2019, A&A, 624, A62

Mallonn, M., Nascimbeni, V., Weingrill, J., et al. 2015, A&A, 583, A138

Mallonn, M., Poppenhaeger, K., Granzer, T., Weber, M., & Strassmeier, K. G. 2021, arXiv e-prints, arXiv:2110.14344

Mallonn, M. & Strassmeier, K. G. 2016, A&A, 590, A100

Mallonn, M. & Wakeford, H. R. 2017, Astronomische Nachrichten, 338, 773

Mancini, L., Kemmer, J., Southworth, J., et al. 2016, MNRAS, 459, 1393

Mancini, L., Sarkis, P., Henning, T., et al. 2020, A&A, 633, A30

Mancini, L., Southworth, J., Ciceri, S., et al. 2014, A&A, 568, A127

Mancini, L., Southworth, J., Mollière, P., et al. 2019, MNRAS, 485, 5168

Mandel, K. & Agol, E. 2002, ApJL, 580, L171

Maxted, P. F. L., Anderson, D. R., Collier Cameron, A., et al. 2016, A&A, 591, A55

Mayor, M., Pepe, F., Queloz, D., et al. 2003, Messenger, 114, 20

McCullough, P. R., Crouzet, N., Deming, D., & Madhusudhan, N. 2014, ApJ, 791, 55

McCullough, P. R., Stys, J. E., Valenti, J. A., et al. 2005, PASP, 117, 783

Miller, N. & Fortney, J. J. 2011, ApJL, 736, L29

Miralda-Escudé, J. 2002, ApJ, 564, 1019

Morris, B. M., Agol, E., Hebb, L., & Hawley, S. L. 2018, AJ, 156, 91

Moses, J. I., Madhusudhan, N., Visscher, C., & Freedman, R. S. 2013, ApJ, 763, 25

Mugnai, L. V., Modirrousta-Galian, D., Edwards, B., et al. 2021, AJ, 161, 284

Murgas, F., Chen, G., Nortmann, L., Palle, E., & Nowak, G. 2020, A&A, 641, A158

Narita, N., Fukui, A., Ikoma, M., et al. 2013, ApJ, 773, 144

Nascimbeni, V., Mallonn, M., Scandariato, G., et al. 2015, A&A, 579, A113

Neilson, H. R., McNeil, J. T., Ignace, R., & Lester, J. B. 2017, The Astrophysical Journal, 845, 65

Nielsen, L. D., Brahm, R., Bouchy, F., et al. 2020, A&A, 639, A76

Nikolov, N., Sing, D. K., Burrows, A. S., et al. 2015, MNRAS, 447, 463

Nikolov, N., Sing, D. K., Fortney, J. J., et al. 2018, Nat, 557, 526

Nikolov, N., Sing, D. K., Gibson, N. P., et al. 2016, ApJ, 832, 191

Nikolov, N., Sing, D. K., Pont, F., et al. 2014, MNRAS, 437, 46

Nortmann, L., Pallé, E., Murgas, F., et al. 2016, A&A, 594, A65

Oshagh, M., Santos, N. C., Boisse, I., et al. 2013, A&A, 556, A19

Oshagh, M., Santos, N. C., Ehrenreich, D., et al. 2014, A&A, 568, A99

Oshagh, M., Santos, N. C., Figueira, P., et al. 2015, A&A, 583, L1

Parviainen, H., Pallé, E., Chen, G., et al. 2018, A&A, 609, A33

Parviainen, H., Pallé, E., Nortmann, L., et al. 2016, A&A, 585, A114

Parviainen, H., Palle, E., Zapatero-Osorio, M. R., et al. 2021, A&A, 645, A16

Parviainen, H., Tingley, B., Deeg, H. J., et al. 2019, A&A, 630, A89

Penev, K., Bakos, G. Á., Bayliss, D., et al. 2013, AJ, 145, 5

Pepper, J., Siverd, R. J., Beatty, T. G., et al. 2013, ApJ, 773, 64

Pollacco, D. L., Skillen, I., Collier Cameron, A., et al. 2006, PASP, 118, 1407

Pont, F., Sing, D. K., Gibson, N. P., et al. 2013, MNRAS, 432, 2917

Poppenhaeger, K. & Wolk, S. J. 2014, A&A, 565, L1

Quirrenbach, A., Amado, P. J., Ribas, I., et al. 2018, in Proceedings of SPIE, Vol. 10702, Ground-Based and Airborne Instrumentation for Astronomy VII, ed. C. J. Evans, L. Simard, & H. Takami, 107020W

Rackham, B., Espinoza, N., Apai, D., et al. 2017, ApJ, 834, 151

Rackham, B. V., Apai, D., & Giampapa, M. S. 2018, ApJ, 853, 122

Rackham, B. V., Espinoza, N., Berdyugina, S. V., et al. 2022, arXiv e-prints, arXiv:2201.09905

Rauer, H., Catala, C., Aerts, C., et al. 2014, Experimental Astronomy, 38, 249

Reiners, A., Bean, J. L., Huber, K. F., et al. 2010, ApJ, 710, 432

Ribas, I., Font-Ribera, A., & Beaulieu, J.-P. 2008, ApJL, 677, L59

Ricker, G. R., Winn, J. N., Vanderspek, R., et al. 2014, in Society of Photo-Optical Instrumentation Engineers (SPIE) Conference Series, Vol. 9143, Space Telescopes and Instrumentation 2014: Optical, Infrared, and Millimeter Wave, ed. J. Oschmann, Jacobus M., M. Clampin, G. G. Fazio, & H. A. MacEwen, 914320

Ricker, G. R., Winn, J. N., Vanderspek, R., et al. 2015, Journal of Astronomical Telescopes, Instruments, and Systems, 1, 014003

Ridden-Harper, A., Turner, J. D., & Jayawardhana, R. 2020, AJ, 160, 249

Rodriguez, J. E., Colón, K. D., Stassun, K. G., et al. 2016, AJ, 151, 138

Rowe, J. F., Bryson, S. T., Marcy, G. W., et al. 2014, The Astrophysical Journal, 784, 45

Rustamkulov, Z., Sing, D. K., Mukherjee, S., et al. 2022, arXiv e-prints, arXiv:2211.10487

Saha, S., Chakrabarty, A., & Sengupta, S. 2021, AJ, 162, 18

Sarkis, P., Mordasini, C., Henning, T., Marleau, G. D., & Mollière, P. 2021, A&A, 645, A79

Schwarz, G. 1978, The Annals of Statistics, 6, 461

Seager, S. 2011, in IAU Symposium, Vol. 276, The Astrophysics of Planetary Systems: Formation, Structure, and Dynamical Evolution, ed. A. Sozzetti, M. G. Lattanzi, & A. P. Boss, 198–207

Seager, S. & Mallén-Ornelas, G. 2003, in Astronomical Society of the Pacific Conference Series, Vol. 294, Scientific Frontiers in Research on Extrasolar Planets, ed. D. Deming & S. Seager, 419–422

Seager, S. & Sasselov, D. D. 2000, ApJ, 537, 916

Sedaghati, E., Boffin, H. M. J., Delrez, L., et al. 2017, MNRAS, 468, 3123

Sedaghati, E., Boffin, H. M. J., Jeřabková, T., et al. 2016, A&A, 596, A47

Sheppard, K. B., Welbanks, L., Mandell, A. M., et al. 2021, AJ, 161, 51

Shporer, A., Wong, I., Huang, C. X., et al. 2019, AJ, 157, 178

Sing, D. K. 2010, A&A, 510, A21

Sing, D. K., Désert, J. M., Lecavelier Des Etangs, A., et al. 2009, A&A, 505, 891

Sing, D. K., Fortney, J. J., Nikolov, N., et al. 2016, Nat, 529, 59

Sing, D. K., Lecavelier des Etangs, A., Fortney, J. J., et al. 2013, MNRAS, 436, 2956

Smalley, B., Anderson, D. R., Collier Cameron, A., et al. 2011, A&A, 526, A130

Southworth, J. 2011, MNRAS, 417, 2166

Southworth, J., Bohn, A. J., Kenworthy, M. A., Ginski, C., & Mancini, L. 2020, A&A, 635, A74

Southworth, J., Mancini, L., Novati, S. C., et al. 2010, MNRAS, 408, 1680

Southworth, J., Wheatley, P. J., & Sams, G. 2007, MNRAS, 379, L11

Stassun, K. G., Corsaro, E., Pepper, J. A., & Gaudi, B. S. 2018, AJ, 155, 22

Stevenson, K. B., Bean, J. L., Seifahrt, A., et al. 2014, AJ, 147, 161

Strassmeier, K. G., Granzer, T., Weber, M., et al. 2004, Astronomische Nachrichten, 325, 527

Strassmeier, K. G., Granzer, T., Weber, M., et al. 2010, Advances in Astronomy, 2010, 970306

Street, R. A., Pollaco, D. L., Fitzsimmons, A., et al. 2003, in Astronomical Society of the Pacific Conference Series, Vol. 294, Scientific Frontiers in Research on Extrasolar Planets, ed. D. Deming & S. Seager, 405–408

Temple, L. Y., Hellier, C., Albrow, M. D., et al. 2017, MNRAS, 471, 2743

Temple, L. Y., Hellier, C., Almleaky, Y., et al. 2018, MNRAS, 480, 5307

Tenenbaum, P. & Jenkins, J. 2018, TESS Science Data Products Description Document, EXP-TESS-ARC-ICD-0014 Rev D, `https://archive.stsci.edu/missions/tess/doc/EXP-TESS-ARC-ICD-TM-0014.pdf`

Thompson, S. E., Fraquelli, D., Van Cleve, J. E., & Caldwell, D. A. 2016, Kepler Archive Manual, Kepler Science Document KDMC-10008-006

Tinetti, G., Drossart, P., Eccleston, P., et al. 2018, Experimental Astronomy, 46, 135

Todorov, K. O., Désert, J.-M., Huitson, C. M., et al. 2019, A&A, 631, A169

Torres, G., Winn, J. N., & Holman, M. J. 2008, The Astrophysical Journal, 677, 1324

Tregloan-Reed, J., Southworth, J., Mancini, L., et al. 2018, MNRAS, 474, 5485

Tsiaras, A., Waldmann, I. P., Tinetti, G., Tennyson, J., & Yurchenko, S. N. 2019, Nature Astronomy, 3, 1086

Tsiaras, A., Waldmann, I. P., Zingales, T., et al. 2018, AJ, 155, 156

Turner, J. D., Ridden-Harper, A., & Jayawardhana, R. 2021, AJ, 161, 72

Turner, O. D., Anderson, D. R., Barkaoui, K., et al. 2019, MNRAS, 485, 5790

Turner, O. D., Anderson, D. R., Collier Cameron, A., et al. 2016, PASP, 128, 064401

VanderPlas, J. T. 2018, ApJS, 236, 16

von Essen, C., Mallonn, M., Hermansen, S., et al. 2020, A&A, 637, A76

von Essen, C., Mallonn, M., Piette, A., et al. 2021, A&A, 648, A71

von Essen, C., Mallonn, M., Welbanks, L., et al. 2019, A&A, 622, A71

Wakeford, H. R. & Sing, D. K. 2015, A&A, 573, A122

Wakeford, H. R., Sing, D. K., Kataria, T., et al. 2017, Science, 356, 628

West, R. G., Hellier, C., Almenara, J. M., et al. 2016, A&A, 585, A126

Wheatley, P. J., West, R. G., Goad, M. R., et al. 2018, MNRAS, 475, 4476

Wilson, P. A., Sing, D. K., Nikolov, N., et al. 2015, MNRAS, 450, 192

Winn, J. N. 2009, in IAU Symposium, Vol. 253, Transiting Planets, ed. F. Pont, D. Sasselov, & M. J. Holman, 99–109

Winn, J. N., Howard, A. W., Johnson, J. A., et al. 2009, ApJ, 703, 2091

Winn, J. N., Johnson, J. A., Howard, A. W., et al. 2010, ApJ, 718, 575

Wolszczan, A. & Frail, D. A. 1992, Nat, 355, 145

Wong, I., Benneke, B., Gao, P., et al. 2020, AJ, 159, 234

Wong, I., Kitzmann, D., Shporer, A., et al. 2021, AJ, 162, 127

Wu, Y. & Lithwick, Y. 2013, ApJ, 763, 13

Yang, F., Chary, R.-R., & Liu, J.-F. 2022, AJ, 163, 42

Yip, K. H., Changeat, Q., Edwards, B., et al. 2021, AJ, 161, 4

Acknowledgments

This section is always my favorite to read in published dissertations and I am so delighted that it is now my time to write the “Acknowledgements” of my own dissertation.

First and foremost, I would like to express my deepest appreciation to my principal supervisor Prof. Dr. Klaus Strassmeier for the opportunity to be a doctoral student at the AIP and for the constant support throughout the years of my studies. I am deeply indebted to Prof. Dr. Philipp Richter, since the moment he accepted me to complete my master in Astrophysics in Potsdam and without knowing he set the wheels in motion for all the following successes. I would like also to extend my deepest appreciation to Potsdam Graduate School (PoGS) for the financial support in the first three years and three months of this PhD, in the form of a doctoral scholarship. I am extremely grateful to Prof. Dr. Katja Poppenhaeger for the guidance and support, for always answering my questions and for treating me like her own student. I would like also to extend my sincere thanks to Dr. Syndey Barnes, for all the fruitful conversations and discussions, especially on how stone by stone, one day someone can build a cathedral.

This dissertation would not have been possible without the help and support of my mentor, Dr. Matthias Mallonn. I deeply appreciate how you have been encouraging and guiding me, since my master studies even, through the PhD proposal and during observations. Thank you for being there in all my efforts and struggles and for pushing me towards being an autonomous and independent scientist. Working under your mentorship has been very enjoyable and I have learned a lot.

Several people took part in making my PhD studies a great life adventure. And I will start by thanking my office mates, Thorsten Caroll and Engin Keles. Thank you, Thorsten, for all the nice discussions regarding work, travels, and for all the patience you have been showing all those years in dealing with Engin and me. Engin, I am so grateful I met you in this life. You are such an excellent friend and colleague. Thank you for always being there for me, for the good humor and the laughter, thank you for all the useful advice and comments, for the science talks, even for the Greek-Turkish office wars and for always cleaning the coffee machine! There is only one thing that prevents you from being the best colleague someone could dream of and this you can achieve it by watering the plants-just once. Also, I would like to special thank you for the German translation of the abstract of this dissertation, and of making suggestions in order to improve the manuscript.

Many wonderful people from the Branch I group contributed in their own way in the success of this PhD. I am forever grateful to Katrin Boehrs, basically for everything. She has been a delightful friend all those years and very helpful with every paperwork that needed to be done; to Carsten Denker, for never refusing answering a question or proofreading a document; to Arto and Silva for all our constructive conversations, including science, games, series, movies and fun, you are simply amazing; to Julian and Eliana for being wonderful people and for always

having an encouraging word to say and always having an open ear for all the questions and problems; to Ekaterina Ilin for being such a supportive colleague and for our nice conversations during a summer school in Vietri Sul Mare; to Nikoleta for all the friendly discussions and advice, and many thanks to Laura for being such a good friend, for her help with poster presentations, best practice for coding in python and for our beautiful adventure at the Aquarium in Crete!

I would like to thank all my bookish friends, especially my friends Chattie, Tallia, Kelli (the Guardians of Middlegrade Joy), and Cloe. I am so happy I met you and I am so grateful for all our buddy reads, which have been such a magical activity aside from all science-work.

My dear Judy, I want to thank you for many things, but I will mention only a top 3 of favorites that I would like to remember forever, especially when I will read this thesis after decades of years in the future. Top 1 will always be café Louise. I hope I will never forget that day that was of the most hilarious in my life! The adventures at the devil's bridge are following in second place (thank you also Jad!) equally with the Potsdam bookclub. So technically, this is a top 2. Thank you so much for all the fun and joy in reading together and adventuring together through Germany with the 9 euro tickets! Your friendship was of the most valuable things that flourished during our studies at the AIP and I am so happy to call you my friend.

I would like to thank also my High Conspiracy Group (HCG – you know who you are) and my Sagrada Familia, Carla and Vladan for being of my most amazing friends! I love you so much, and I admire you a lot for everything you achieved in this life! You have always been an inspiration, both of you. Thank you for showing me that family can be people you choose and not necessarily blood related relatives. And speaking about family, I would like to thank also my D&D family, John-John and Rebecca (and Felix too), Kristin, Sarah and Hauke. You kept my imagination alive through the hard times of the pandemic, and you made my life more magical, and this is priceless! I will always remember our adventures! - "Rota Fortunae" and "Firebaaaall" and life was just great! A huge thank you to Rebecca (again) because she proofread the entire dissertation on a very short notice before submission!

Thank you to my Katia, my Sunshine, my dose of Vit D and my sister in Potsdam, for the continuous support, the motivation, the encouragement, the walks in the park, the concerts, the ballets, the awesome trips and adventures, the "extrablatting" times and for one more million reasons including from rushing to bookstores and rekindling my reading passion, to proofreading of my works, without a single complaint every single time for all those years since we met. I love you so much. This thesis would have never happened without you. Forever grateful.

Thank you to my family, to Sofi and George for being like parents, to Stefanos for being like a brother, to Vaso for being like a sister, to mom for simply being, and to my amazing sister Joanna for being everything and more. Joanna is the sister that everyone would wish for but only me, I am the lucky one to have. Thank you for being the "big" sister with all the weights and responsibilities, so that I can be the "little" one and accomplish my lifetime dream. Thank you for all the fights you gave for me, so that I could be happy. You are my angel ♡.

Many heartfelt thanks to my partner, Ioannis, who has never let me feel alone (during the pandemic and up to now). Thank you for always being there for me, my love. For all the emotional support and the discussions regarding sneaky codes that don't work. Thank you for the fun, the smiles and hugs, the Age of Mythology and DST, the beautiful journeys, for our "secret garden", the fishing routines, the stargazing at Alexandrini, the homemade food, for making me feel that home is you. And thank you, Elsa and Ptolemy, for being a part of this home too!

With all my heart, I would like to dedicate this thesis to two people:

To my sister, Joanna, because I love her lots, because she has always believed in me, and she has always been my guiding star;

and to my beloved aunt, Lemonia†, because we shared the same dream and she was the inspiration for everything in this life. We made it ♡.

"We are all stardust and stories"
— Erin Morgenstern, The Starless Sea

Eidesstattliche Erklärung

Hiermit bestätige ich, dass die vorliegende Arbeit selbständig verfasst und keine anderen als die angegebenen Quellen und Hilfsmittel benutzt sowie Zitate und gedankliche Übernahmen kenntlich gemacht wurden. Die Arbeit wurde ausschließlich an der Universität Potsdam und keiner anderen Hochschule eingereicht.

Ort, Datum

Unterschrift